Solar Energy Materials & Solar Cells 204 (2020) 110212

Contents lists available at ScienceDirect

Solar Energy Materials and Solar Cells

journal homepage: http://www.elsevier.com/locate/solmat

Recent progress on cesium lead/tin halide-based inorganic perovskites for stable and efficient solar cells: A review

Bhaskar Parida [a], Saemon Yoon [a], Sang Mun Jeong [b], Jung Sang Cho [c], Jae-Kwang Kim [d,**], Dong-Won Kang [a,*]

[a] School of Energy Systems Engineering, Chung-Ang University, Seoul, 06974, Republic of Korea
[b] Department of Chemical Engineering, Chungbuk National University, 28644, Republic of Korea
[c] Department of Engineering Chemistry, Chungbuk National University, 28644, Republic of Korea
[d] Department of Solar & Energy Engineering, Cheongju University, 28503, Republic of Korea

ARTICLE INFO

Keywords:
Solar cell
Inorganic perovskites
Stability
Long term
Carrier transport

ABSTRACT

A comparable power conversion efficiency (PCE) to that of commercial Si solar cells (over 23%) has been achieved by organic–inorganic hybrid perovskite solar cells (OIH-PSCs) within several years. As OIH-PSC materials have hygroscopic organic cations that limit their thermal and long-term stability (i.e. operational lifetime of about 1 year, much shorter than commercial Si of 20–25 years), significant research efforts have been directed to the development of all-inorganic PSCs to overcome this limitation. These studies have demonstrated that cesium lead halide ($CsPbX_3$) and Pb-free cesium tin halide ($CsSnX_3$) perovskites are promising materials for the fabrication of thermally stable and efficient solar cells. This work reviews recent progress on versatile $CsPbX_3$ and $CsSnX_3$ inorganic PSCs. Remarkable PCE values over 17% and 4% have been achieved by employing $CsPbX_3$ and $CsSnX_3$ perovskites, respectively, in a short development time. In addition, we evaluate the materials engineering methods and film deposition techniques for producing such inorganic perovskite materials. Several strategies including surface and interfacial passivation are discussed to alleviate hysteresis and instability of inorganic PSCs. Furthermore, future research directions including device engineering using inorganic metal oxide charge transport layers are suggested to further reinforce this innovative advances in the inorganic PSCs.

1. Introduction

The global energy requirements for urbanization and use of electronic products is increasing rapidly. However, most of the required electric energy is full filled by exhaustible non-renewable fossil fuels which have detrimental effects on human health and environment. Therefore, renewable energy such as wind energy, water energy and solar energy have been found to be the best sources to produce electrical energy. Among these renewable energy sources solar energy attracts more attention due to the abundant availability of sunlight. Therefore, in last few decades the development of solar cells has been considerably grown because a solar cell can directly convert the solar energy to electric energy and can solve the energy crisis problem and global warming due to carbon emission in a greater extent. Generally, the solar cells have been classified into three generations, i.e. (1) first generation: mono- and multi-crystalline wafer based Si solar cells, (2) second generation: a-Si, CdTe, GaAs, CIGS, CuGaSe thin film based solar cells, and (3) third generation: multijunction, CZTs, CZTSe, CZTSSe, quantum dot, organic, dye-sensitized and perovskite solar cells. However, current photovoltaic market is dominated by Si based solar cells due to their mature technology, superior stability over 20 years and high PCE of 26.7% [1]. Despite the well-established technology, various studies on fabricating solar cells using solution processing at low temperature have been made for the development of low cost and flexible solar cells.

Over the last decade, organic-inorganic hybrid perovskites have attracted great attention due to their potentials of low-cost and easy fabrication, excellent intrinsic properties, such as a very long carrier diffusion length [2], high carrier mobility [3], tunable bandgap [4], and high optical absorption coefficient [5]. The general chemical formula of the organic–inorganic perovskite material is ABX_3, where A is a monovalent organic cation (e.g., $CH_3NH_3^+$ (MA^+), $HC(NH_2)_2)^+$ (FA^+), or Cs^+), B is a divalent metal cation (e.g., Pb^{2+}, Sn^{2+}), and X is a halide anion (e.

* Corresponding author.
** Corresponding author.
E-mail addresses: jaekwang@cju.ac.kr (J.-K. Kim), kangdwn@cau.ac.kr (D.-W. Kang).

https://doi.org/10.1016/j.solmat.2019.110212
Received 21 June 2019; Received in revised form 21 September 2019; Accepted 1 October 2019
Available online 14 October 2019
0927-0248/

g., I^-, Br^- Cl^- or a mixture of these). Methylammonium lead iodide ($CH_3NH_3PbI_3$), also referred to as $MAPbI_3$, is the most commonly studied perovskite due to its bandgap of 1.5 eV that allows absorption of a wide range of the solar spectrum, and ambipolar characteristics [2], which are essential for solar cells. The excellent optical and electrical properties of ABX_3 materials allowed the development of PSCs with a power conversion efficiency (PCE) that significantly increased from 3.8% to 24.2 % within a decade, making them highly competitive to traditional Si-based solar cells [6,7]. Recently, along with the development of OIH-PSCs, some other ABX_3 PSCs with super-alkali cations and super-halogen anions have also been reported [8–11].

Furthermore, the PSCs can be made using common metals and industrial chemicals. Also, the simple, low-temperature and common solution-processed low-cost spin- or spray-coating techniques are very attractive for prospective low-cost production of PSCs. Several deposition techniques, such as a multi-step methods [12], or single-step methods using antisolvent washing [13], thermal evaporation [14], and chemical vapor deposition (CVD) [15] have been developed and achieved high-quality pinhole-free polycrystalline perovskite films with large grains that facilitate efficient PSCs. However, $MAPbI_3$ perovskites are very sensitive to moisture, and show poor thermal and photo-stability, which limits their commercialization [16,17].

Formamidinium lead triiodide ($FAPbI_3$) has been developed as an alternative to $MAPbI_3$ as it shows longer and broader light absorption with better photostability [18]. However, $FAPbI_3$ shows an unwanted phase transition at room temperature, where the black perovskite-type trigonal structure (α-phase) transforms to a yellow non-perovskite hexagonal structure (δ-phase). Therefore, to enhance the stability of the perovskite compounds, various strategies for tailoring the composition have been demonstrated, in particular, the introduction of mixed cations and/or halides. For example, $MAPbBr_3$ was incorporated into $FAPbI_3$, which stabilized the $FAPbI_3$ perovskite phase and enhanced the PCE up to 18% [19]. It has been further reported that the partial replacement of FA by Cs (resulting in a perovskite composition of $FA_{0.9}Cs_{0.1}PbI_3$) or the mixture of triple-cation perovskites in $Cs_x(MA_{0.17}FA_{0.83})_{(1-x)}Pb(I_{0.83}Br_{0.17})_3$ significantly improved the photo- and moisture stability, PCE, and more importantly, phase stability [20,21]. Although organic–inorganic PSCs have shown good efficiency, the processing temperature of the solar cell device is limited by the poor stability of volatile organic cations, such as MA^+ and/or FA^+ that are thermally unstable at high temperature.

In an effort to address the stability problems, much research is being devoted to developing materials with alternative organic cations that improve the stability without decreasing the PCE. Therefore, all-inorganic perovskites, such as cesium lead halide ($CsPbX_3$ where X = Cl, Br, and I) have recently attracted a lot of interest due to their remarkably high stability under high humidity and high temperature (without requiring any encapsulation), and excellent optoelectronic properties [22,23]. The first inorganic PSC based on $CsPbBr_3$ was reported by Kulbak et al.; they demonstrated that the PSCs processed under ambient atmosphere generated high open circuit voltages (V_{oc} = 1.3 V), with an efficiency of 5.95% and good stability. However, $CsPbBr_3$-based inorganic perovskites exhibit a wide bandgap of 2.3 eV and can only absorb light below a wavelength of 540 nm, which limits the PCE. Similarly, the first $CsPbI_3$-based inorganic PSCs were reported by Eperon et al., with a stable PCE of 2.9%. The $CsPbI_3$-based inorganic perovskites have a bandgap of 1.73 eV, which makes them more suitable for solar cells than $CsPbBr_3$. However, the black cubic phase of $CsPbI_3$ (α-$CsPbI_3$) is unstable at room temperature under ambient conditions, where transformation to δ-$CsPbI_3$ phase occurs [24].

Such dedicated research efforts have quickly achieved materials with excellent stability and a record PCE of 17.06% [25]. However, most OIH-PSCs contain a large fraction (≈35%) of Pb, which is highly toxic. Due to this toxicity, most Pb-containing substances used in electronic devices are strictly banned by the European Union and other countries, which has motivated the fabrication of Pb-free PSCs [26,27]. The most feasible replacement for Pb in PSCs is tin. Thus, several recent studies focused on the development of lead-free PSCs, such as $MASnI_3$ [28] and $FASnI_3$ [29]. However, these PSCs also suffer from instability problems due to their hygroscopic organic cations (MA^+ or FA^+) that limit outdoor applications [30,31]. Therefore, compounds containing inorganic cations and lead-free perovskites, such as cesium tin halide ($CsSnX_3$) perovskites, have been developed.

In this paper, we review the recent progress in fabricating inorganic PSC devices with high PCE and stability. In particular, we discuss various strategies that have been proposed for increasing the efficiency and stability of perovskite materials and their corresponding solar cells; these include modifying the composition of lead-based and lead-free inorganic perovskites, solvent engineering, deposition techniques, and surface and interfacial passivation.

2. Basic concepts of PSCs

2.1. Crystal structure of inorganic perovskites

It is well known that the general formula of a typical perovskite is ABX_3, where A is the monovalent cation (Cs^+, MA^+, FA^+), B site is a bivalent cation (Pb^{2+}, Sn^{2+}) and X site is a halide (I^-, Br^-, and Cl^-) [32]. Moreover, the phase stability of the halide perovskites can be determined by its octahedral factor (μ) and the Goldschmidt's tolerance factor (*t*):

$$\mu = R_B/R_X \tag{1}$$

and

$$t = \frac{R_A + R_X}{\sqrt{2}(R_B + R_X)} \tag{2}$$

where R_A, R_B and R_X are the radius of the A-site and B-site cation, and X-site anion, respectively [33]. A stable black phase of the inorganic perovskite can be obtained when $0.8 \leq t \leq 1$ and $0.44 < \mu < 0.9$. However, a perfect cubic symmetry of perovskite requires *t*-factor in between 0.9 and 1; lowering or exceeding the upper limit of the *t*-factor can result non-perovskite yellow phase of the perovskite due to lattice distortion [24] which causes worse optical absorption, wider bandgap and results in low PCE. Depending on the *t*-factor and temperature, $CsPbX_3$ inorganic perovskites have four different crystal structures such as cubic phase (α), tetragonal phase (β), orthorhombic phase (γ) and non-perovskite phase (δ). Some perovskite derivatives such as A_2BX_6, $A_2B^{3+}X_6$, $A_3B_2X_9$, and $A_3B_2X_7$ have been also reported, but a very low PCE has been achieved by utilizing these perovskite derivatives for PSCs because of the formation of low dimensional crystal structure and multiple polymorphs [34].

2.2. Working principle and device physics of PSCs

A PSC is composed of multilayers such as a transparent conducting metal oxide as front electrode, the perovskite absorber sandwiched between and ETL and HTL, and a metal back electrode. When light incidents on the PSC, it will get absorbed by the perovskite absorber and give rise to electron-hole pairs. These electrons and hole will drift and diffuse due to the built-in electric fields and get collected on the contacts of the solar cell. However, the bandgap of the perovskite absorber shows a trade-off relation for the output current i.e. a low bandgap absorber can absorb more light and generate higher current. But the low bandgap absorber also affects the output voltage of the PSC because of the quasi-fermi level difference of the electrons and holes [35]. On the other hand, a high bandgap perovskite absorber suffers from the poor absorption of light and results low output current though it generates high output voltage. Therefore, it has been theoretically predicted that a single junction solar cell with an optimal bandgap between 1.1 eV and 1.4 eV can produce a maximum PCE of 33% [36].

The PCE can be obtained from the current density-voltage (J-V) characterization, measured under a standard AM 1.5 solar simulator with light intensity of 100 mW/cm^2. Generally, the PCE is defined as the ratio of maximum power output (P_{out})to the incident light power input (P_{in}) or can be determined by the short circuit current density (J_{sc}), V_{oc} and fill factor (FF) as:

$$PCE = \frac{P_{out}}{P_{in}} = \frac{V_{oc} \times J_{sc} \times FF}{P_{in}} \quad (3)$$

$$FF = \frac{V_{MP} \times J_{MP}}{V_{oc} \times J_{sc}}, \quad (4)$$

where V_{MP} and J_{MP} are the maximum voltage and current density at the maximum power.

Apart from the tolerance factor dependent stability issues, the J-V hysteresis has been found to be a common problem in all type of PSCs. Hysteresis happens when a mismatch of the J-V curves of the same solar cells occurs under the reverse and forward scan measurement [37,38]. To date, the reason for the origin of hysteresis in PSCs is not clear although few reports have been reported including, (1) Ferroelectric polarization [39,40], (2) ion migration [41,42], (3) charge trapping [43], (4) capacitive effect [44], (5) phase segregation [45,46]. Consequently, the hysteresis in PSCs can be overcome by improving the quality of perovskite film, passivating the interfaces for faster charge transport process and passivating the surface or grain boundary defects.

3. Compositional modification of lead-based and lead-free inorganic perovskites

Modification of the composition of PSCs has played a major role in optimizing both structural and optical properties of these materials, which greatly affect the device performance and stability. For example, the bandgap of the halide perovskite can be tuned using mixed-cation and mixed-halide compositions, resulting in optical absorption over a broad range of wavelengths [4,47,48]. As we discussed above that a stable perovskite crystal (ABX_3) can be obtained when the Goldschmidt t-factor is $0.8 \leq t \leq 1$ [33,49]. However, Cs-based inorganic perovskites have low t-factor values, which indicate poor phase stability, and their wide bandgap limits further improvements of the PCE [50]. Some selected compositional modifications of inorganic perovskites that have been demonstrated to improve their structural stability and device performance are discussed in this section.

3.1. $CsPbBr_3$ PSCs

Cesium lead halide base inorganic PSCs were reported for the first time by Kulbak et al., in 2015 [51]. They fabricated $CsPbBr_3$-based inorganic PSCs with a device structure of glass/-FTO/mp-TiO_2/$CsPbBr_3$/spiro-OMeTAD or PTAA/Au (Fig. 1a) and proposed that the organic cation (MA^+) of the organic–inorganic hybrid perovskites ($MAPbX_3$) can be replaced by inorganic cations (e.g., Cs^+) to increase the stability and V_{oc} of the solar cell. The V_{oc} is an important metric for solar cells as it is a measure of the maximum voltage available from the device. In 2016, this group further reported that $CsPbBr_3$-based PSCs exhibited higher efficiency and thermal stability than $MAPbBr_3$ PSCs and were stable over two weeks under dry air with Room humidity (RH) of 15–20%, constant illumination, and electron beam irradiation without encapsulation (Fig. 1b, and c) [51]. However, the organic hole transport layers (O-HTLs) used in these devices are quite expensive, and unstable against humidity and heat, which hinders the mass production and practical deployment of the PSCs.

In an attempt to increase the O-HTL stability, Chang et al. replaced the O-HTL with a carbon electrode and fabricated a $CsPbBr_3$ PSC device in an air atmosphere, which showed a PCE of 5% and significant thermal stability of 250 h at 80 °C [53]. Meanwhile, Liang et al. developed the first generation of all-inorganic PSCs by employing $CsPbBr_3$/carbon layers [52] with a similar approach to a previous study [53]. Interestingly, these non-encapsulated all-inorganic PSCs showed a remarkable PCE of 6.7% and operated well under extreme operating conditions of high humidity (90–95%) and temperature (100 °C) for over three months without any performance degradation (Fig. 1d–f). Both these works demonstrated that $CsPbBr_3$ inorganic perovskites have higher

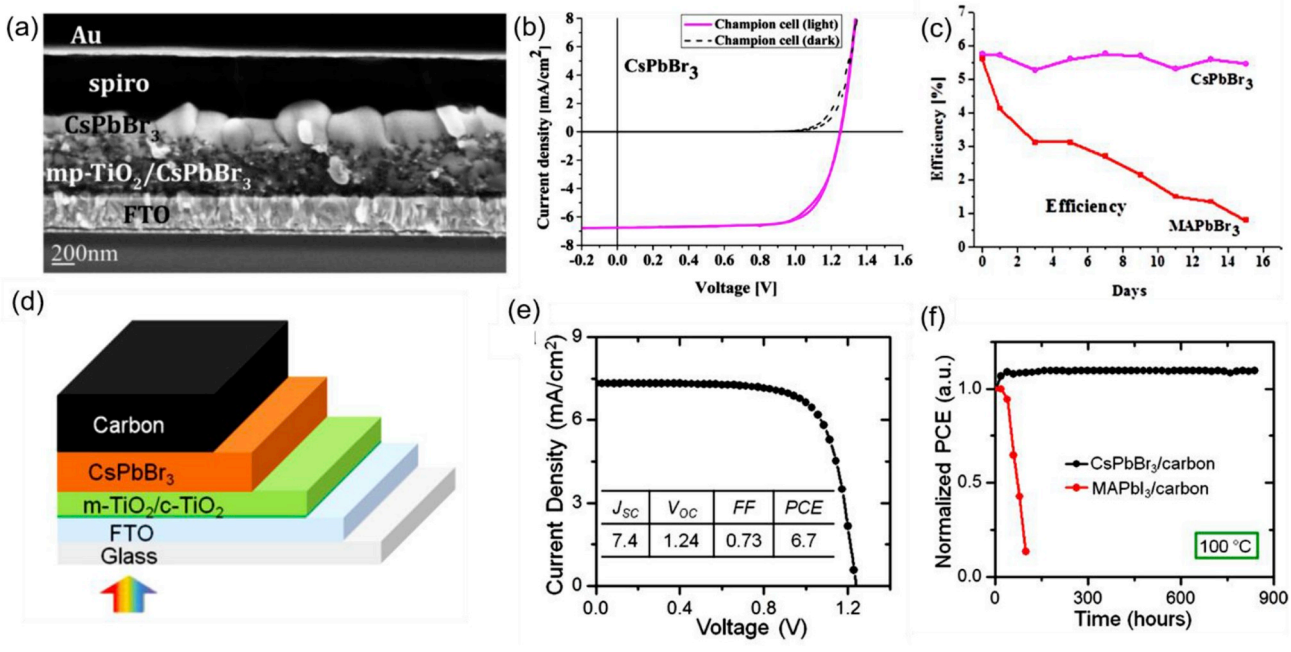

Fig. 1. (a) Cross-sectional SEM image of $CsPbBr_3$ PSCs. Reproduced with permission [22], copyright 2015, American Chemical Society. (b) J–V curve of a $CsPbBr_3$ PSC and (c) time-dependent PCE of unencapsulated $CsPbBr_3$ PSCs. Reproduced with permission [51], copyright 2016, American Chemical Society. (d) Device structure of an all-inorganic PSC with a carbon electrode, (e) J–V curve and PCE of $CsPbBr_3$ PSC, and (f) normalized PCE stability of unencapsulated $CsPbBr_3$ and $MAPbI_3$ PSCs at 100 °C. Reproduced with permission [52], copyright 2016, American Chemical Society.

stability than that of organic–inorganic hybrid PSCs. The use of carbon electrodes in these PSCs demonstrated a new direction for fabricating cheap and stable PSCs.

Furthermore, a significant advance was made by Akkerman et al. by tuning the optical and electronic properties of optoelectronic devices using colloidal semiconductor nanocrystals. They synthesized $CsPbBr_3$ nanocrystals using small low-boiling-point ligands like propionic acid (PrAc) and butylamine (BuAm), and environmentally friendly solvents like 2-propanol and hexane, at room temperature (Fig. 2a and b) [54]. Such $CsPbBr_3$ nanocrystals exhibited a photoluminescence quantum yield (PLQY) of $58 \pm 6\%$ in solution and $35 \pm 4\%$ in the film after coating. The PLQY of these nanocrystals in film form was 30% higher than those of long alkyl chains, which remained insulating. The film also exhibited an amplified spontaneous emission threshold as low as $1.5\ \mu J\ cm^{-2}$ (Fig. 2c), which is the lowest value ever reported for $CsPbBr_3$ nanocrystals. When these nanocrystal films with optimized thickness were used to fabricate PSC devices with a structure of FTO/c-TiO_2/$CsPbBr_3$/spiro-MeOTAD/Au, a PCE of 5.4% and a very high V_{oc} of 1.5 V were measured (Fig. 2d). This V_{oc} was the highest value reported for Cs-based inorganic PSCs. The $CsPbBr_3$ perovskite exhibits a bandgap of 2.3 eV. It has been reported that the theoretical V_{oc} of the Br perovskite-based wide bandgap PSCs is limited to 1.85 V due to the nonradiative recombination induced by the large work function difference between the HTL and electron transport layer (ETL) [55,56]. Thus, it is expected that the V_{oc} of $CsPbBr_3$ PSCs can be further improved by proper design of the HTLs and/or ETLs.

The use of $PbCl_2$ has been shown to improve both the microstructure and photophysics of PSCs [57]. Li et al. were the first to incorporate $PbCl_2$ into $CsPbBr_3$ perovskites (via a sequential deposition technique) and investigate its effect on the morphological, structural, optical, and device performance of $CsPbBr_3$-based PSCs [58]. They observed two major functions of $PbCl_2$ in $CsPbBr_3$ perovskites. Firstly, $PbCl_2$ controlled the crystal structure by promoting the phase transition of $CsPbBr_3$ from orthorhombic to cubic (Fig. 3a). Secondly, $PbCl_2$ passivated the interface between the ETL and perovskite, which increased the electron extraction rate, electron and hole lifetimes, and carrier diffusion lengths (Fig. 3b). As a result, the $PbCl_2$-induced $CsPbBr_3$ PSCs showed a PCE of 6.21%, which was higher than that of undoped $CsPbBr_3$ PSCs with a PCE of 3.78% (Fig. 3c). Recently, several strategies for interface passivation of all-inorganic PSCs using inorganic quantum dots have been published, which produced devices with excellent performance, including a PCE of 9.72% for $CsPbBr_3$-based inorganic PSCs; the thermal stability of this device will be discussed in Section 5 [59–61].

Despite the reported improvements in device performance, the carrier recombination in $CsPbBr_3$ perovskite films is still high due to the presence of grain-boundary-related defect states and low carrier lifetime in the film. To overcome such issues, increasing the grain size of the crystals and ensuring long carrier lifetime in the film are crucial factors for maximizing the power output. Therefore, Duan et al. doped $CsPbBr_3$ films with lanthanide ions ($Ln^{3+} = Sm^{3+}$, Tb^{3+}, Ho^{3+}, Er^{3+}, and Yb^{3+}) via a multistep solution-processing method [62]. The grain size and density of the perovskite films gradually increased with decreasing atomic number of Ln^{3+} ions, where the perovskite film doped with Sm^{3+} ions resulted in an average grain size of 1 μm (Fig. 4a). The proposed mechanism for the formation of large grains involved Ln^{3+} ions being expelled to the surface and grain boundaries, which resulted in highly oriented crystal domains due to changes in the surface energy of crystal growth. The large grains of the Ln^{3+}-doped $CsPbBr_3$ perovskite film both increased carrier lifetime and reduced carrier recombination within the film. Using these Ln^{3+}-doped $CsPbBr_3$ perovskite films with an optimized stoichiometry in HTL-free PSCs with a device structure of FTO/c-TiO_2/mp-TiO_2/$CsPb_{0.97}Sm_{0.03}Br_3$/carbon, a PCE of 10.14% and an ultrahigh V_{oc} of 1.594 V were achieved (Fig. 4b). Furthermore, these devices without encapsulation showed excellent moisture and thermal

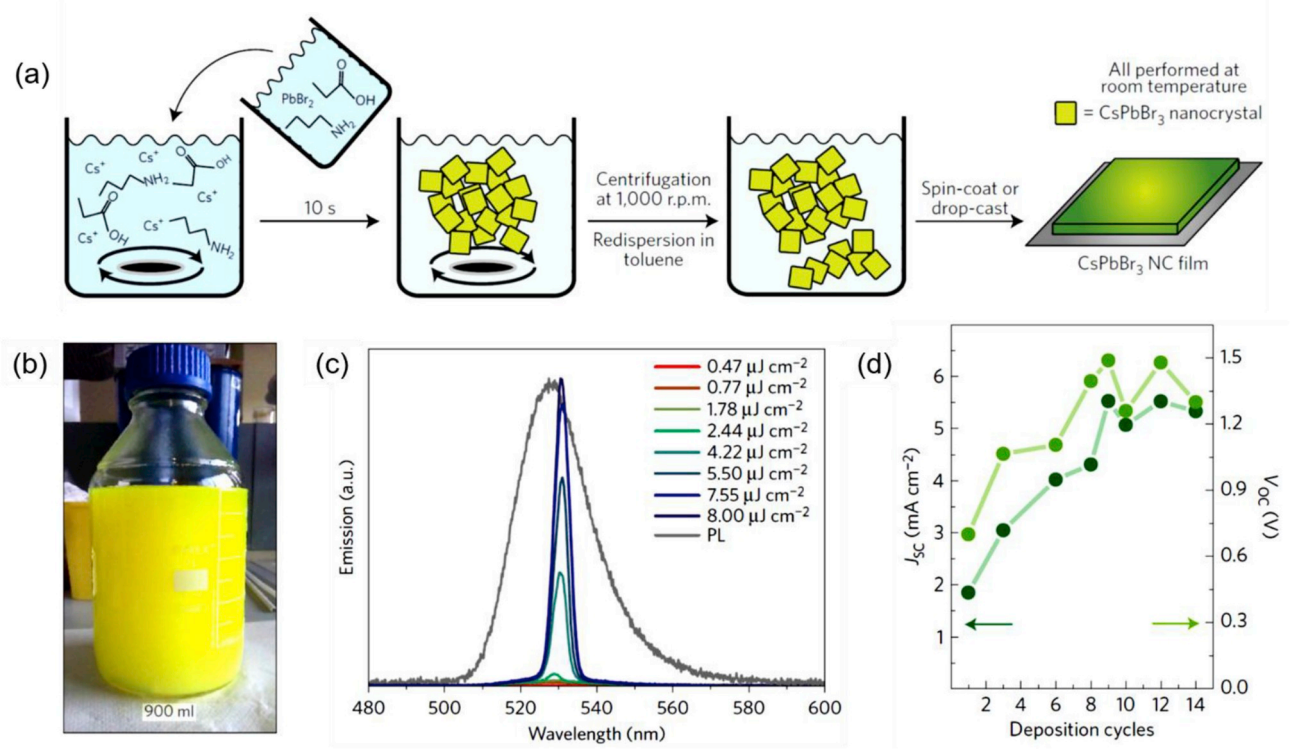

Fig. 2. (a) Schematic diagram of the synthesis of $CsPbBr_3$ nanocrystals and fabrication of $CsPbBr_3$ nanocrystal films; (b) photograph of scaled-up (2-gram) synthesis of $CsPbBr_3$ nanocrystal solution; (c) ASE spectra under increasing fs-pulsed excitation fluence with ($\lambda_{exc} = 405$ nm) recorded from a spin-coated film of $CsPbBr_3$ film. (d) J_{sc} (dark green dots) and V_{oc} (light green dots) as a function of $CsPbBr_3$ nanocrystal deposition cycle dependent an all-inorganic PSC with a carbon electrode. Reproduced with permission [54]; copyright 2016, Nature Publishing Group. (For interpretation of the references to colour in this figure legend, the reader is referred to the Web version of this article.)

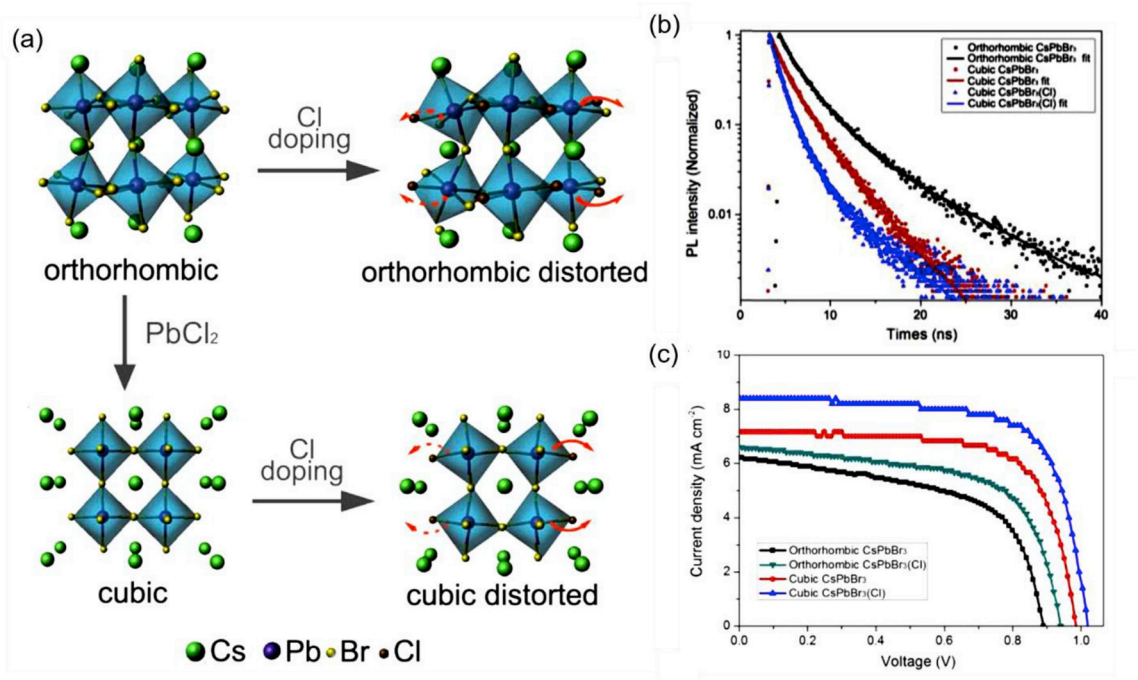

Fig. 3. (a) Schematic diagrams of molecular models of orthorhombic- and cubic-phase $CsPbBr_3$ perovskites with and without $PbCl_2$ doping. (b) Carrier lifetime measured from TRPL spectra of a $CsPbBr_3$/mp-TiO_2 layer. (c) J–V curve of orthorhombic and cubic $CsPbBr_3$ inorganic PSCs. Reproduced with permission [58]; copyright 2017, Elsevier.

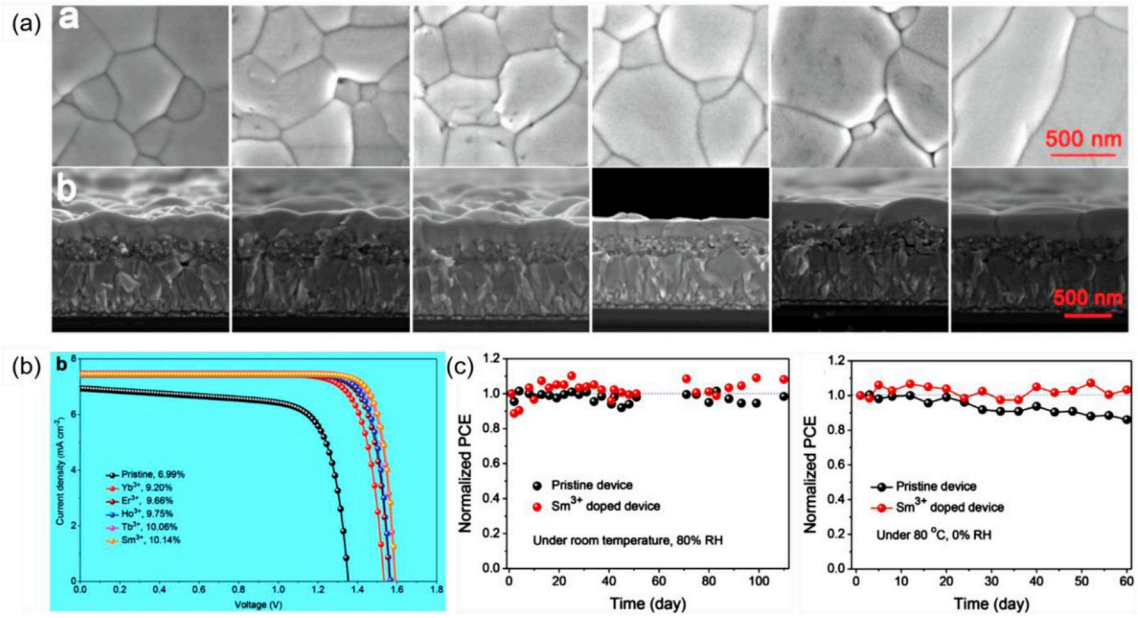

Fig. 4. (a) Top and cross-sectional SEM images of as-prepared Ln^+-doped $CsPbBr_3$ films on FTO/c-TiO_2/mp/TiO_2 substrates (left to right: $CsPbBr_3$, Yb^{3+}-$CsPbBr_3$, Er^{3+}-$CsPbBr_3$, Ho^{3+}-$CsPbBr_3$, Tb^{3+}-$CsPbBr_3$, and Sm^{3+}-$CsPbBr_3$). (b) J–V curves of all-inorganic PSCs with $CsPbBr_3$ films doped with various Ln^+ contents. (c) Stability of the normalized PCE of Sm^{3+}-doped unencapsulated $CsPbBr_3$ PSCs under humid (25 °C and RH = 80%) and high-temperature (80 °C, RH = 0%) conditions. Reproduced with permission [62]; copyright **2018**, Wiley-VCH.

stability; the initial PCE of the devices was maintained over 95% and 90% at room temperature under conditions of 80% RH for over 100 d, and 80 °C at 0% humidity for 60 d, respectively (Fig. 4c).

3.2. *$CsPbI_3$ PSCs*

All-inorganic PSCs provide a new strategy for fabricating low-cost, efficient, and highly stable next-generation solar cells. However, inorganic $CsPbBr_3$ devices show lower PCE values than organic–inorganic hybrid PSCs due to their wide bandgap ($E_g = 2.3$ eV). Inorganic $CsPbI_3$ perovskites are more suitable for PSC applications as they have a narrower bandgap of 1.73 eV; however, it is impossible to fabricate and operate these materials in an ambient atmosphere due to the rapid degradation of the perovskite cubic phase (α-$CsPbI_3$) to the non-perovskite orthorhombic phase (δ-$CsPbI_3$). According to Eperon et al., the addition of a small amount of HI to the $CsPbI_3$ precursor

solution stabilizes the cubic phase of the $CsPbI_3$ perovskite [23], which showed pronounced crystallinity at a low temperature of 100 °C (Fig. 5a and b). They also suggested that these inorganic perovskites had high carrier diffusion lengths and speculated that hysteresis in the current–voltage curves of the PSCs was not due to the ferroelectric properties, as $CsPbI_3$ does not exhibit ferroelectric polarization behavior. The main role of HI was forming the stable black phase of $CsPbI_3$ at a low temperature, which was characterized by the formation of small crystals. These smaller $CsPbI_3$ crystals induced a phase transition at low temperature due to the generation of lattice strain, which partially stabilized the α-$CsPbI_3$ phase.

Phase stabilization by small nanocrystals of $CsPbI_3$ is an excellent strategy for fabricating stable and efficient $CsPbI_3$ inorganic PSCs. Swarnkar et al. reported that the nanocrystal surface could be used to stabilize the α-$CsPbI_3$ phase at room temperature [63]. They synthesized highly stable α-$CsPbI_3$ quantum dots (QDs) via a synthesis route using Cs-oleate and PbI_2 precursors and processing temperatures ranging from 60 °C to 185 °C to obtain different sizes of QDs. The QDs were purified using methyl acetate (MeOAc), which acted as an antisolvent to remove excess unreacted precursors without inducing agglomeration, resulting in QDs that were stable in the cubic phase for several months in an air atmosphere. They fabricated $CsPbI_3$-based inorganic PSCs using these QDs by spin coating, followed by dipping in a MeOAc solution for ligand removal. The $CsPbI_3$-based inorganic PSCs with a device structure of FTO/c-TiO_2/$CsPbI_3$ QD film/Spiro-OMeTAD/MoO_x/Al showed a high PCE of 10.77% and V_{oc} of 1.23 V (Fig. 5c). However, when these PSCs without encapsulation were stored in an air atmosphere with 40–60% humidity for 2 d, their PCE decreased to 2.55% due to the slow transformation of the QD films into bulk $CsPbI_3$ film. Later, the same group reported treatment of the $CsPbI_3$ QDs with A-site cation halide salts (AX, where A= FA^+, MA^+ or Cs^+ and X= I^- or Br^-), which significantly increased the film mobility and photocurrent, resulting in the highest reported PCE of 13.43% for QD-based PSC [64].

A similar approach was used by Wang et al. to stabilize the cubic phase of $CsPbI_3$ by reducing the grain size [65]. They added a small amount (1.5 wt%) of sulfobetaine zwitterion in the $CsPbI_3$ precursor solution, which reduced the average grain size to 30 nm due to the electrostatic interaction between the zwitterion and the ions and colloids; this helped increase the grain surface area and stabilize the α-$CsPbI_3$ phase (Fig. 6a). The zwitterions in the precursor solution interacted with the PbI_2-DMSO complex, breaking its layered structure and preventing rapid grain growth, which resulted in an amorphous phase after spin coating. During thermal annealing of these films, the zwitterions were thought to migrate to the grain boundaries and hinder further grain growth, which resulted in small grains (Fig. 6b). The inorganic PSCs fabricated using these small α-$CsPbI_3$ grains with a device structure of ITO/PTAA/$CsPb(I_{0.98}Cl_{0.02})_3$/PCBM/$C_{60}$/BCP/metal achieved a PCE of 11.4% (Fig. 6c) and maintained 85% of its initial performance over 30 d in air without encapsulation.

These studies indicated that the use of additives for grain size engineering has great potential for enhancing the structural and thermal stability of inorganic perovskites. Therefore, several further studies were conducted to increase the PCE and stability of the inorganic PSCs using additives such as ethylenediamine (EDA), oleylammonium (OA), and phenylethylammonium (PEA) acetate [66,67]. These additives showed good moisture and thermal stability and increased the PCE values compared to control samples without additives. Fu et al. introduced long-chain ammonium additives (OA and PEA) into $CsPbI_3$ to achieve phase stabilization. They formed two different metastable $CsPbI_3$ polymorphs, α-$CsPbI_3$ and β-$CsPbI_3$ (the less-common orthorhombic phase), using a one-step spin-coating process with OA and PEA additives, respectively (Fig. 6d). These additives resulted in highly stable bulk $CsPbI_3$ perovskites, which were stable at room temperature for four months. As there are few reports of β-$CsPbI_3$ perovskite-based devices and their performance, they fabricated β-$CsPbI_3$-based PSCs, which showed efficient charge transport properties due to electron and hole diffusion lengths of 350 nm and 94 nm, respectively in β-$CsPbI_3$ (Fig. 6e and f). Heterojunction PSCs based on the β-$CsPbI_3$ perovskite films

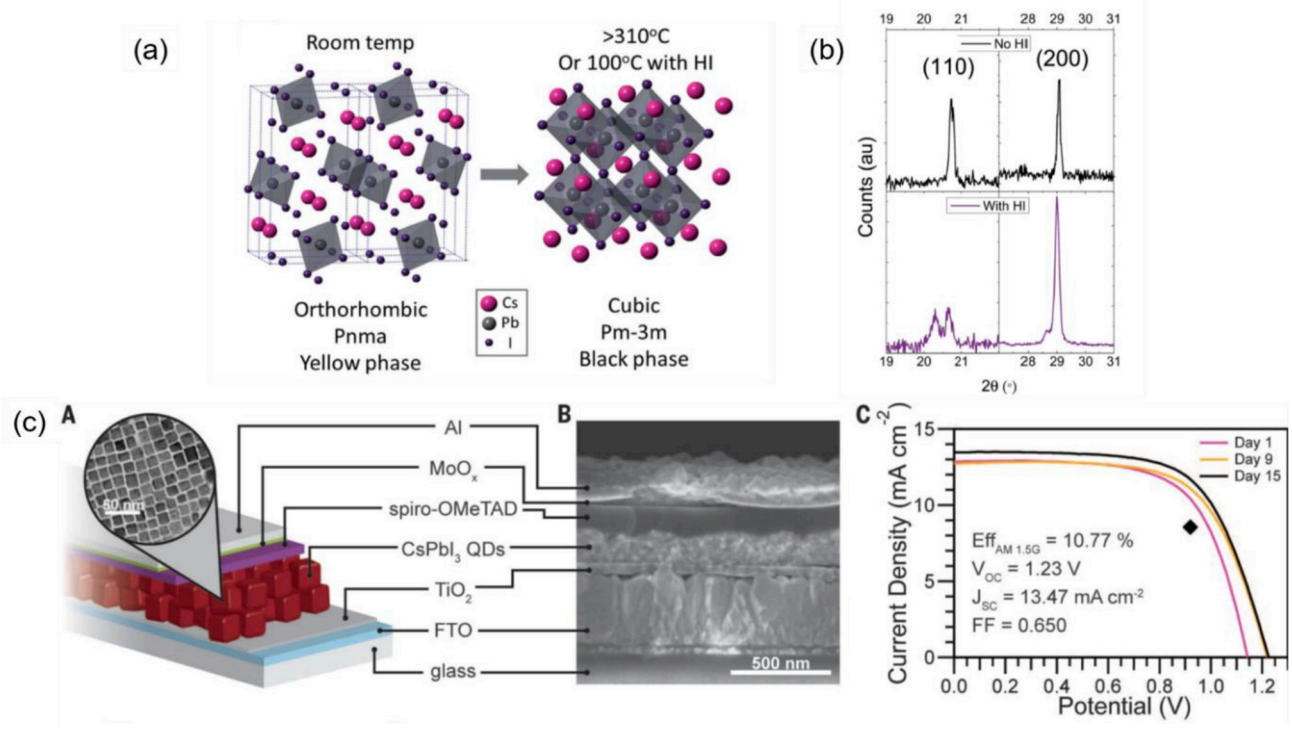

Fig. 5. (a) Schematic diagram of the crystal structure of yellow- and black-phase $CsPbI_3$. (b) XRD patterns of $CsPbI_3$ perovskite films deposited from solution with and without HI addition. Reproduced with permission [23]; copyright 2015, Royal Society of Chemistry. (c) Schematic diagram and cross-sectional image of the structure of PSCs based on $CsPbI_3$ QD layers, and their PCE values (without encapsulation) as a function of storage period. Reproduced with permission [63]; copyright 2016, Science Publishing Group. (For interpretation of the references to colour in this figure legend, the reader is referred to the Web version of this article.)

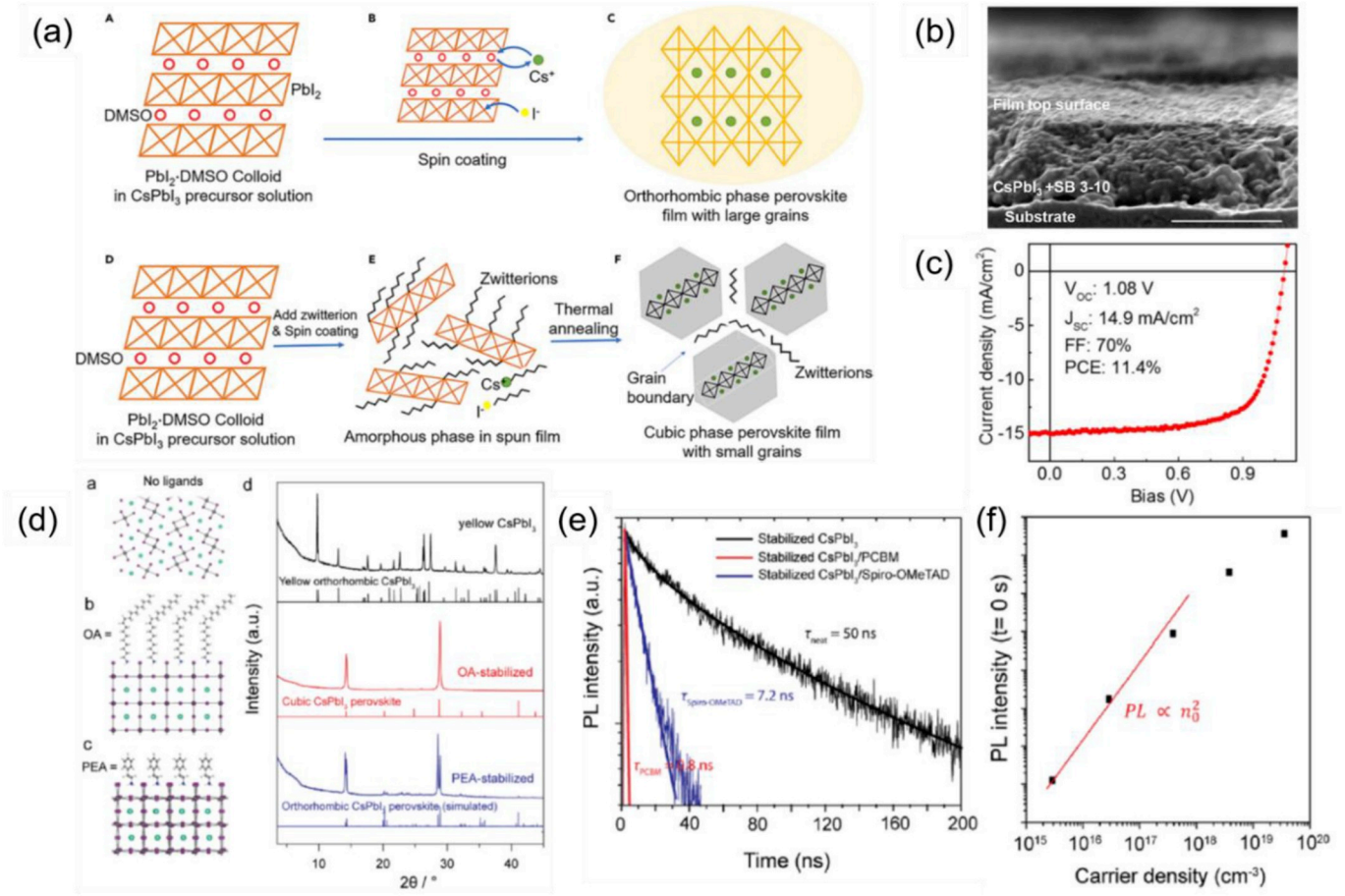

Fig. 6. (a) Schematic diagram of the proposed mechanism of zwitterion-induced phase stabilization in $CsPbI_3$ films. (b) SEM and (c) J–V curves of PSC with NDSB-201-added $CsPbI_3$ film. Reproduced with permission [65]; copyright 2017, Elsevier. (d) Schematic of the OA and PEA induced phase stabilization mechanism of $CsPbI_3$ films and their (e, f) photophysical properties. Reproduced with permission [66]; copyright 2017, American Chemical Society.

demonstrated a PCE of 6.5%.

Wang et al. recently reported that the organic cations (PEA^+) of phenylethylammonium iodide (PEAI) could be used to enhance the phase stability of $CsPbI_3$ perovskites [68]. They showed that PEA^+ could not intercalate into the crystal lattice of $CsPbI_3$, as PEAI cannot react with the bulk $CsPbI_3$ to form a new crystal phase or 2D perovskite layer by either solid cation exchange or subsequent cation exchange reactions. Therefore, it was hypothesized that PEA^+ cations terminated on the surface of $CsPbI_3$ perovskites by occupying the cation sites of $CsPbI_3$ via the NH_3^+ functional group (Fig. 7a). The PEA^+ and I^- ions passivated Cs^+

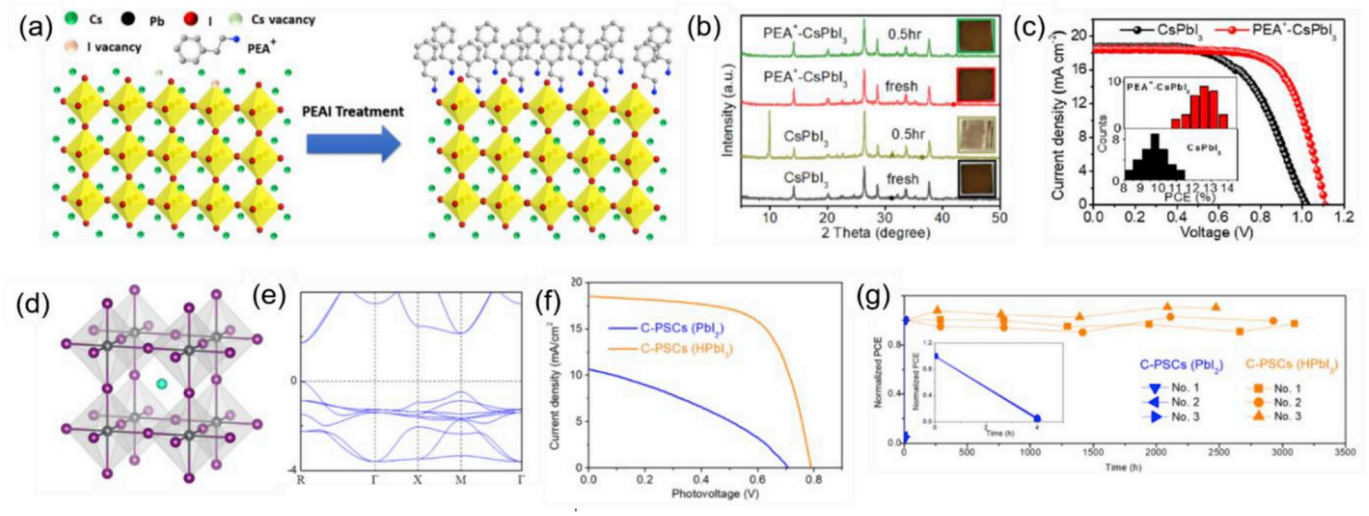

Fig. 7. (a) Schematic of the PEA^+-induced stabilization of $CsPbI_3$ films, and the (b) stability under moisture, and (c) J–V curves of $CsPbI_3$ and PEA^+-$CsPbI_3$ PSCs. Reproduced with permission [68]; copyright 2018, Elsevier. (d) Schematic of the unit cell structure, (e) calculated band structures, (f) PCE, and (g) normalized PCE of $HPbI_3$-treated α-$CsPbI_3$ films and unencapsulated solar cells. Reproduced with permission [69]; copyright 2018, Elsevier.

and I^- vacancies or defects on the surface of $CsPbI_3$ and blocked the formation of a 2D perovskite capping layer, which has been observed for organic–inorganic hybrid perovskites. The organic PEA^+ cations formed a functional organic group layer on the surface to stabilize the crystal structure of $CsPbI_3$, which enhanced the phase stability, moisture resistance (Fig. 7b), and passivated the surface, resulting in an increase in V_{oc} and the FF. PSCs based on the PEA^+-$CsPbI_3$ perovskite showed a stable and reproducible PCE of 13.5% (Fig. 7c) and excellent stability after storing in a dry box with RH < 20% at RT and thermal stability at 50 °C under continuous illumination for 200 h without encapsulation.

Similarly, Zhang et al. incorporated a small amount of EDA cations into $CsPbI_3$, which facilitated the formation of highly stabilized α-$CsPbI_3$ and prevented the formation of the δ-phase upon exposure to air [66, 67]. The two terminal NH_3^+ groups of EDA occupied two A cation sites and resulted in the formation of 2D A_2BX_4 perovskites. When these 2D perovskites of $EDAPbI_4$ were added to $CsPbI_3$, the intercalated EDA cations prevented the undesirable phase transition to the δ-phase by cross-linking the $CsPbI_3$–$EDAPbI_4$. Furthermore, it was hypothesized that the $EDAPbI_4$ both regulated the grain size and acted as a surface passivation layer in $CsPbI_3$. These perovskite films were stable, even after annealing at 100 °C for 150 h and retained their stability at room temperature for months. In addition, no EDA impurities were observed from X-ray diffraction (XRD) patterns, indicating that the EDA cations were successfully incorporated into the perovskite lattice. Using an optimized concentration of $EDAPbI_4$ (0.025 M) in the $CsPbI_3$ precursor, they achieved a highest PCE of 11.86% with high stability after storing in dry box without encapsulation. These findings encourage further investigation of combinations of 2D and 3D perovskites, which are expected to facilitate the fabrication of PSCs with enhanced structural stability.

Furthermore, QDs and additive-induced nanocrystals have been widely employed to increase the stability of the cubic phase of $CsPbI_3$ at room temperature [63]. However, these films contain many grain boundaries, which induce carrier recombination and hinder carrier transport. To overcome these issues and obtain a highly stable cubic phase of $CsPbI_3$ at room temperature, Xiang et al. replaced PbI_2 with $HPbI_3$ in a one-step deposition solution process in dry air (20–30 °C and 10–20% relative humidity) [69]. During annealing of the film after spin coating, CsI diffused into $HPbI_3$ crystals to induce the nucleation and growth of α-$CsPbI_3$ crystals with the generation of lattice strain (Fig. 7d). The lattice strain in the $HPbI_3$-processed $CsPbI_3$ perovskite film played a major role in stabilizing the large α-$CsPbI_3$ crystals and narrowing the bandgap to 1.68 eV, resulting in increased light absorption (Fig. 7e). These films also showed a higher carrier lifetime than a PbI_2-processed $CsPbI_3$ perovskite film, implying that $HPbI_3$ can effectively reduce carrier trap densities. The PSC fabricated using this highly stable α-$CsPbI_3$ perovskite film with a device structure of FTO/TiO_2/α-$CsPbI_3$/carbon resulted in a PCE of 9.5%, V_{oc} of 0.79 V, J_{sc} of 18.5 mA/cm^2, and FF of 65% (Fig. 7f). Most importantly, the device exhibited excellent long-term stability and retained 90% of the initial PCE over 3000 h of storage in dry air with temperature: 20–30 °C, RH: 10–20% (Fig. 7g) without encapsulation. These results indicate that the combination of the $HPbI_3$ precursor and carbon electrode can be effectively used to fabricate highly stable and efficient α-$CsPbI_3$-based inorganic PSCs.

In addition to the incorporation of organic ions to achieve phase stabilization of the $CsPbI_3$ perovskites, partial substitution of Pb on the B-site of the ABX_3 perovskite lattice has been proposed by several groups. Hu et al. reported the incorporation of Bi in $CsPbI_3$ and investigated the effect of Bi on the crystal structure of $CsPb_{1-x}Bi_xI_3$ [70]. The complete phase stability of the $CsPbI_3$ perovskite was obtained with 4 mol% Bi^{3+} content, which was confirmed by the characteristic α-phase peaks of (100), (110), (111), and (200) in the XRD spectra. Hence, it was suggested that several factors contributed to the enhanced phase stability of $CsPbI_3$ after Bi incorporation (Fig. 8a). First, the smaller ionic radii of Bi^{3+} resulted in a higher t value of the $CsPb_{1-x}Bi_xI_3$ (0.84) perovskite film than that of $CsPbI_3$ (0.81). Secondly, the Bi doping effectively induced the formation of microstrain in the perovskite crystal lattice, which contributed to the long-term phase stability of α-$CsPb_{1-x}Bi_xI_3$ (Fig. 8b). Notably, 4 mol% of Bi was optimal for distorting the $CsPbI_3$ cubic lattice, resulting in a reduction in the grain size that stabilized the α-$CsPbI_3$ and narrowed the bandgap from 1.73 eV to 1.56 eV. In addition, Bi effectively reduced the carrier trap densities and defect concentration in the α-$CsPbI_3$ perovskite film. The fabricated PSC with the optimized $CsPb_{0.96}Bi_{0.04}I_3$ perovskite layer sandwiched between a compact TiO_2 ETL and CuI HTL had an excellent PCE of 13.2% (Fig. 8c) and high stability at 25 °C and 55% humidity without any encapsulation (Fig. 8d).

Similarly, the doping of $CsPbI_3$ with Ca and Sb was also reported [71, 72]. Lau et al. investigated the partial replacement of Pb^{2+} ions with Ca^{2+} in a $CsPbI_3$ precursor and reported its multiple benefits. Firstly, the doping of Ca^{2+} reduced the size of the colloids in the precursor solution, producing uniform films with larger grains than the undoped film (Fig. 8e), which enhanced the interfacial contact between the perovskite and HTL. Secondly, with increasing Ca content, the bandgap increased from 1.72 eV to 1.93 eV (Fig. 8f), which is the opposite effect to Bi doping. Finally, Ca doping resulted in the formation of a Ca-rich oxide layer on the surface of the $CsPbI_3$ film, which acted as a surface passivation layer and increased the carrier lifetime (Fig. 8g). An optimal concentration of 5% Ca^{2+} in the precursor solution resulted in a perovskite $CsPb_{0.95}Ca_{0.05}I_3$ film which was used to achieve a stabilized PCE of 13.3% with a device structure of glass/-FTO/c-TiO_2/mp-TiO_2/$CsPb_{0.95}Ca_{0.05}I_3$/P3HT/Au (Fig. 8h). The encapsulated PSCs with 5% Ca maintained 85% of their initial PCE for over two months of storage at RT with a relative RH of 60–70%. Furthermore, Xiang et al. showed that Sb doping of $CsPbI_3$ in an air atmosphere at a low temperature of 110 °C was very effective for stabilizing the α-$CsPbI_3$ phase. The fabricated carbon-based HTL-free $CsPb_{0.96}Sb_{0.04}I_3$ PSC showed a promising PCE of 5.18%, and the device retained 93% of its initial PCE value over 37 d after storage in an air atmosphere (RH: < 20%, RT) without any encapsulation.

The thermodynamic instability of inorganic $CsPbI_3$ perovskites is a major challenge. A new black orthorhombic γ-$CsPbI_3$ perovskite phase was developed by Zhao et al. in late 2018 [73] in an attempt to increase the stability of $CsPbI_3$ perovskites. A small amount of H_2O was added to the $CsPbI_3$ precursor solution containing equimolar amounts of CsI and PbI_2 in a mixture of dimethylformamide (DMF) and HI; a facile one-step deposition method was used, followed by low-temperature annealing at 100 °C to obtain the $CsPbI_3$ perovskite film. H_2O fractions (x) of 0, 0.01, 0.02, and 0.04 vol% in DMF were used. XRD patterns of the x = 0.02 sample showed diffraction peaks at 2θ = 28.5° and 14.1°, corresponding to the (004) and (002) reflections, respectively, which were indexed to the black orthorhombic phase of $CsPbI_3$. They proposed a two-stage mechanism i.e. initially the PbI_2 and ions solvated in the DMF/HI solvent mixture in the presence of DMF.xHI molecular complexes formed the precursor solution. At the second stage, when H_2O was added into the precursor solution, it provided a strong ionization medium for DMF and HI to promote the proton transfer reaction in the precursor solution as described by the following equation:

$$DMF.xHI + xH_2O \rightarrow DMF + xH_3O^+ + xI^- \quad (5)$$

The increase in activity of the H^+ and I^- ions concentration facilitated the size reduction of PbI_2 colloids in the precursor as a result the crystal size of the perovskite film also reduced. During spin-coating, I^- ions in the solution coordinated to form corner sharing $[PbI_6]^{4-}$ octahedra intercalated by the Cs^+. The octahedral framework converted to the stable γ-$CsPbI_3$ perovskite structure with a small crystal size (100 nm) upon annealing at 100 °C (Fig. 9a and b). Based on the DFT calculations, the low Miller-index surface of the perovskite-structured γ-$CsPbI_3$ exhibited a lower surface energy (0.13 J/m^2) than the δ-$CsPbI_3$ (2.57 J/m^2) and higher surface area (over 8600 m^2/mol). It has been reported that, when the materials size decreases, the surface/volume ratio increases, and the materials tend to convert to a more

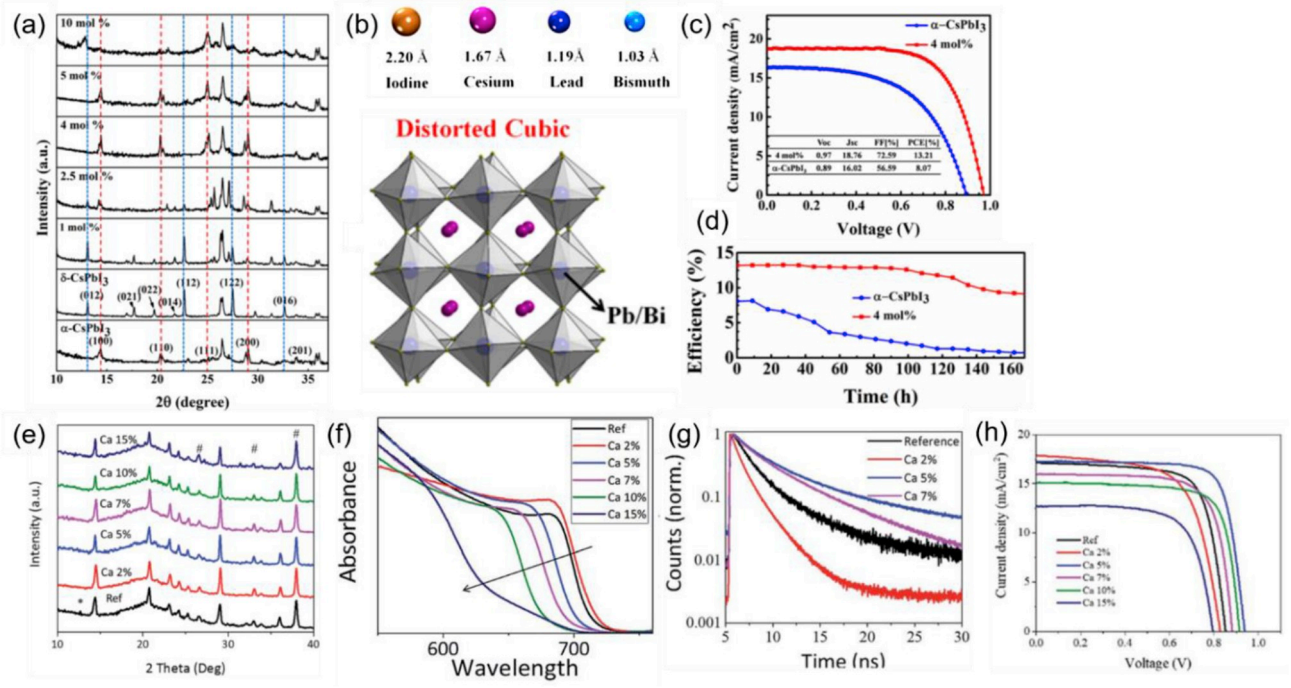

Fig. 8. (a) XRD patterns of $CsPb_{1-x}Bi_xI_3$ perovskites. (b) Schematic distorted stabilized crystal structure of $CsPb_{0.96}Bi_{0.04}I_3$ perovskites. (c) J–V curves and (d) time-dependent PCE of $CsPb_{0.96}Bi_{0.04}I_3$-based PSCs without encapsulation. Reproduced with permission [70]; copyright 2017, American Chemical Society. (e) XRD patterns, (f) absorbance spectra, and (g) TRPL decay curves of $CsPb_{1-x}Ca_xI_3$ perovskite films, and (h) J–V curves of their PSCs. Reproduced with permission [71]; copyright 2018, The Royal Society of Chemistry.

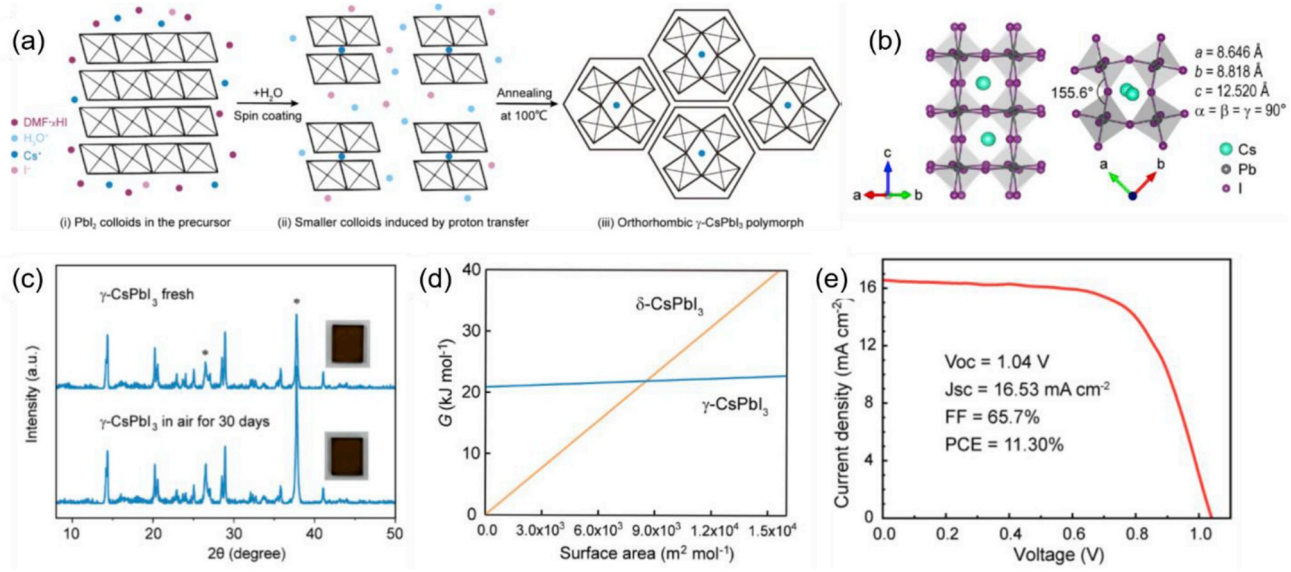

Fig. 9. (a) Schematic diagram of H_2O-induced formation and stabilization, and (b) crystal structure of γ-$CsPbI_3$ perovskites. (c) Storage-dependent XRD patterns and (d) surface area of the γ-$CsPbI_3$ films. (e) J–V curves and PCE of the γ-$CsPbI_3$-based PSCs. Reproduced with permission [73]; copyright 2018, American Chemical Society.

symmetric crystal structure because symmetrical crystal structures have smaller surface energy [74]. Thus, the low surface energy and high surface area made the γ-$CsPbI_3$ perovskite thermodynamically stable (Fig. 9d). A PSC fabricated with the γ-$CsPbI_3$ inorganic perovskite showed excellent performance, with a PCE of 11.3% (Fig. 9e). In addition, reliable performance was observed, where no noticeable performance loss of the unencapsulated devices was observed under an ambient environment with RH 10±5% for over 40 days.

3.3. *$CsPbI_2Br$ PSCs*

To further overcome the structural and thermal instability of $CsPbI_3$ PSCs, a simple approach of mixing halides has attracted much attention from researchers. In early 2016, Sutton et al. reported modified $CsPbI_3$ inorganic perovskites and fabricated $CsPbI_2Br$ by varying the ratio of I and Br [75]. The partial incorporation of Br into $CsPbI_3$ stabilize the cubic phase, even in ambient air. Absorption and PL spectra of the $CsPbI_2Br$ showed that the bandgap could be appropriately tuned by

varying the I and Br ratios (Fig. 10a and b). The optical bandgap of the $CsPbI_2Br$ inorganic perovskite was 1.92 eV, making it suitable for tailoring tandem devices with c-Si and copper indium gallium selenide solar cells. At that time, the highest PCE of 9.8% was obtained from a cesium-lead-halide-based inorganic PSC with a planar device structure (Fig. 10c) and the devices were measured in ambient atmosphere without any encapsulation. At the same time, Beal et al. used a similar approach to form uniform compositions of $CsPb(Br_xI_{1-x})_3$ perovskites with low Br concentrations [76]. They also tuned the bandgap of the inorganic perovskites to 1.9 eV by substituting the $CsPbI_3$ lattice with 33% of Br. The addition of Br also significantly improved the optical and thermal stability.

The durable stability and adequate performance of $CsPbI_2Br$ perovskites have inspired the development of many different approaches for preparing films of this material. Achieving void-free perovskite films with uniform grains and high crystallinity is a key strategy for developing inorganic $CsPbX_3$ PSCs. Notably, $CsPbX_3$ inorganic perovskites require high temperature processing, which restricts their application in multilayer or flexible solar cells. Rao et al. developed the room temperature solvent annealing (RTSA) technique to control the perovskite crystallization dynamics using DMSO, which resulted in highly uniform and void-free $CsPbI_2Br$ films at a low temperature of 120 °C [77]. This method effectively removed the high boiling point DMSO and induced the formation of uniform void-free perovskite films. According to their plausible mechanism, the DMSO molecules continuously coordinate with PbI_2 or $PbBr_2$ arrays consisting of layered octahedral $(PbI_6)^{4-}$ and are embedded into interlamellar interstices of the layered PbI_2; this resulted in an increase in the PbI_2 interlayer distance along the c-axis, and subsequently, longer PbI_2 interplanar distances. The longer interplanar distances in PbI_2 assist subsequent intercalation of CsI into the PbI_2 lattice, leading to the formation of the PbI_2-CsI-DMSO intermediate phase. The intercalation of CsI into the PbI_2 removed the DMSO molecules and formed the cubic phase of the $CsPbI_2Br$ perovskite. $CsPbI_2Br$-based PSCs (with an inverted planar structure) fabricated using the RTSA technique achieved a maximum PCE of 6%. When an additional annealing step was employed after RTSA treatment of these films, the perovskite grain size increased with increasing temperature (from 50 °C to 300 °C) (Fig. 10d, and e). A relatively low annealing temperature of 120 °C was optimal for producing uniform grain growth, resulting in the highest device performance of 10.4% (Fig. 10f). Due to the low-temperature processing, efficient, flexible $CsPbI_2Br$-based PSCs were achieved, which showed a maximum PCE of 7.3%.

The stoichiometric ratios of the precursors in the $CsPbI_{3-x}Br_x$ films need to be accurately controlled by carefully considering the hygroscopic nature of CsI and CsBr. Using this strategy, Chen et al. successfully co-deposited stoichiometrically balanced PbI_2 and CsBr to form high-quality $CsPbI_2Br$ perovskite films [78]. By controlling parameters such as post-annealing temperature and time, a large grain size of 3 μm was achieved. The fabricated PSCs with a device structure of ITO/-$Ca/C_{60}/CsPbI_2Br/TAPC/TAPC:MoO_3/Ag$ resulted in a PCE of 11.8% (Fig. 11a). Similarly, Nam et al. investigated the effect of annealing temperature on the crystal growth of $CsPbI_2Br$ perovskite films [79]. A pinhole-free surface morphology with a uniform and dense crystal structure was formed at an optimal moderate annealing temperature of 280 °C (Fig. 11b). At this temperature, the surface and bulk defects of the perovskite films were passivated, which enhanced both the phase stability and device performance. The PSCs fabricated using the optimal conditions exhibited a PCE of 10.7% and V_{oc} of 1.23 V (Fig. 11d), which were higher values than previous reports [75,76].

Additionally, several doping strategies were employed to promote crystal growth in an attempt to increase the phase stability, and modify the structural and optoelectronic properties of $CsPbI_2Br$ perovskites. Nam et al. reported the partial substitution of Cs^+ ions with K^+ ions in $CsPbI_2Br$ [80]. The partial incorporation of K^+ ions in $Cs_{1-x}K_xPbI_2Br$ improved the structural stability and electron lifetime, without affecting the light absorption; this resulted in a clear increase in the PCE to 10%, and the unencapsulated devices were more stable in air (RH: 20%, Temperature: 20 °C) with under continuous operation than that of pristine $CsPbI_2Br$ PSCs (Fig. 12a-c). Lau et al. reported the incorporation of Sr into $CsPbI_2Br$ with a low-temperature annealing process to form

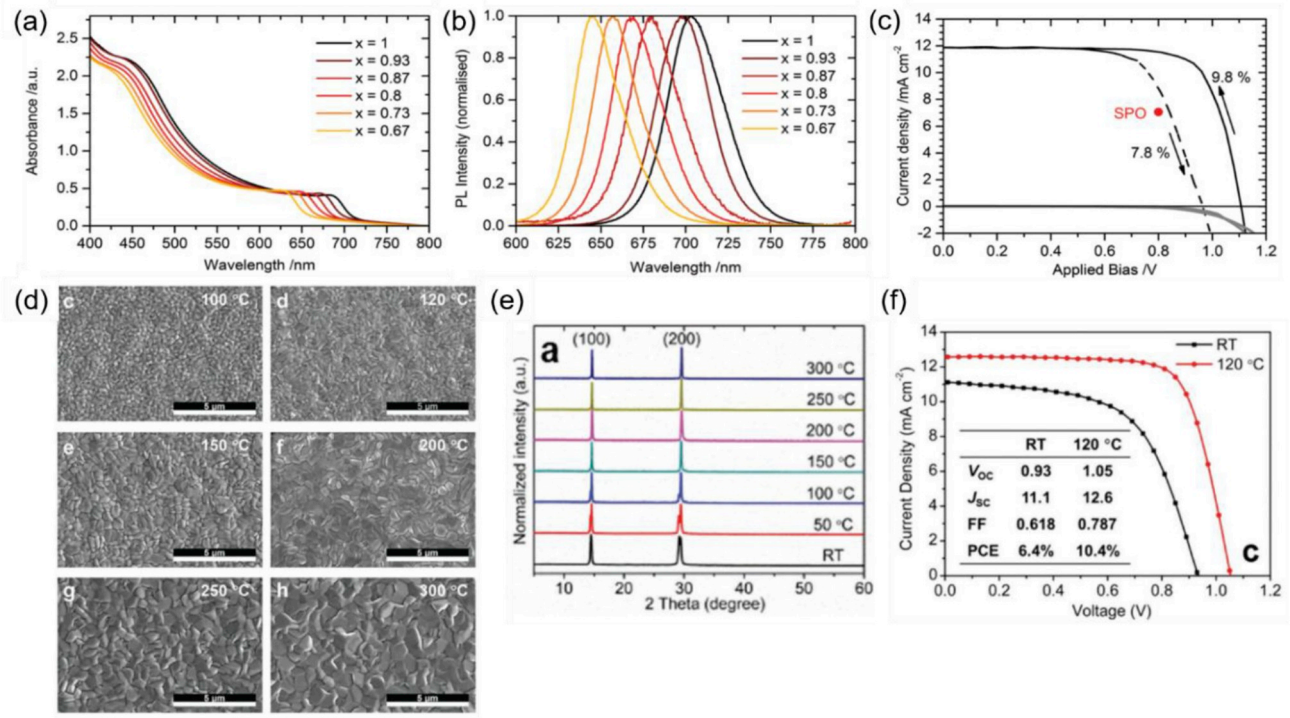

Fig. 10. (a) Photographs, and optical absorption and PL spectra of $CsPbI_2Br$ films with various Br contents, and J–V and PCE curves of the respective PSCs. Reproduced with permission [75]; copyright 2016, Wiley-VCH. (d) SEM images and (e) XRD spectra of $CsPbI_2Br$ films after post-annealing treatment. (f) J–V curves and PCE of $CsPbI_2Br$-based PSCs and Reproduced with permission [77]; copyright 2018, Wiley-VCH.

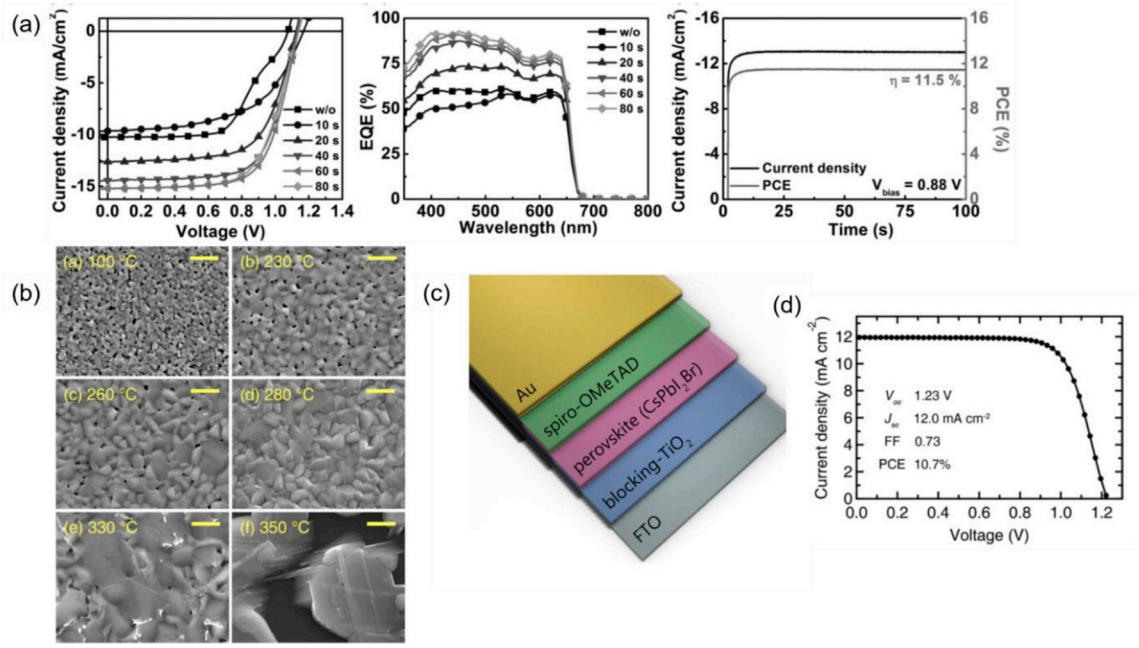

Fig. 11. (a) J–V characteristics, EQE spectra, time-dependent J_{sc}, and PCE of $CsPbI_2Br$-based PSCs. Reproduced with permission [78]; copyright 2017, Wiley-VCH. (d) SEM images of $CsPbI_2Br$ films annealed at various temperatures. (e) Schematic diagram of the device structure and (f) J–V characteristics and PCE of $CsPbI_2Br$-based PSCs. Reproduced with permission [79]; copyright 2017, American Chemical Society.

$CsPb_{1-x}Sr_xI_2Br$ perovskites and investigated their structural properties, carrier lifetime behavior via time-resolved photoluminescence (TRPL), and device performance [81]. The surface morphology of the perovskite films had snowflake-like structures due to the enrichment of Sr on the surface (Fig. 12d); this formed SrO, which played a major role in passivating surface defects. The surface passivation reduced non-radiative surface recombination and effectively increased the carrier lifetime, which increased the PCE from 7.7 to 11.3% for PCSs with a device structure of FTO/c-TiO_2/mp-TiO_2/$CsPb_{1-x}Sr_xI_2Br$/P3HT/Au (Fig. 12e).

3.4. $CsPbIBr_2$ PSCs

Although mixed-halide-like $CsPbI_2Br$ has shown better stability than $CsPbI_3$, it still degenerates to the yellow phase when exposed to air due to its high iodine content. To further enhance the stability of iodine-rich Cs-based lead halide inorganic perovskites, Br-rich Cs-based inorganic PSCs have been proposed as an alternative compositional modification. In early 2016, Ma et al. reported a non-stoichiometric approach to fabricate HTL-free $CsPbIBr_2$ inorganic PSCs via thermal evaporation of CsI and $PbBr_2$ precursors [82]. The Br-rich $CsPbIBr_2$ inorganic perovskite film showed a typical bandgap of 2.05 eV and PL emission at 2 eV with high thermal stability (Fig. 13a). The $CsPbIBr_2$ film showed better thermal stability in both a N_2 environment and ambient conditions than equivalent $CsPbI_3$ and $CsPbI_2Br$ films; no changes in the morphology and optical properties of the $CsPbIBr_2$ films were observed (Fig. 13b). However, inorganic PSCs based on $CsPbIBr_2$ films showed poor performance (PCE = 4.7%) and large hysteresis because of the absence of the

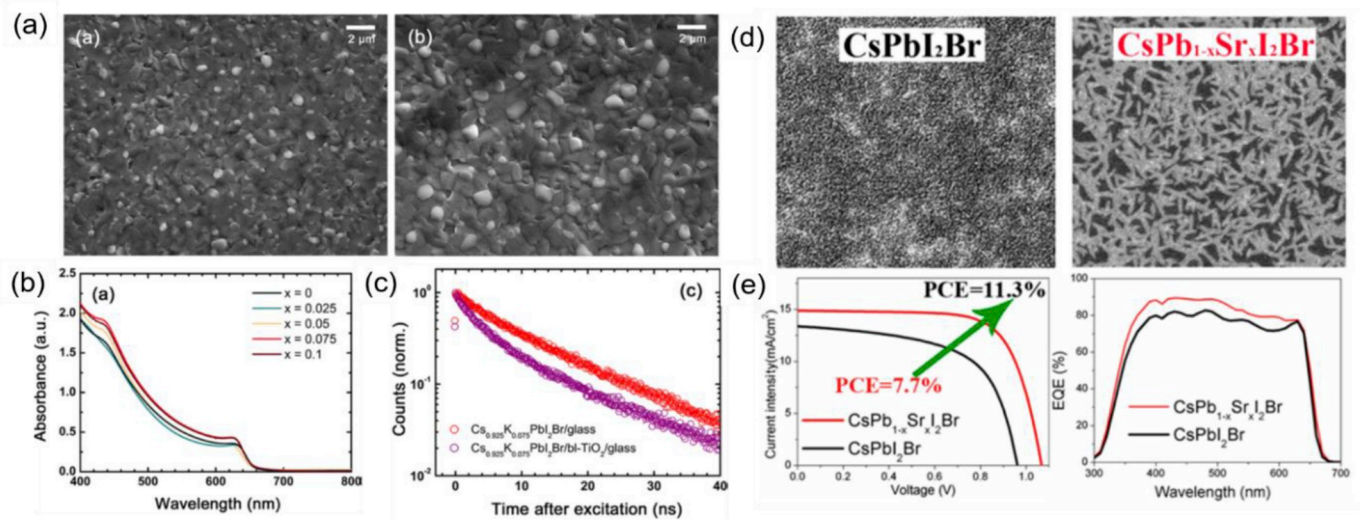

Fig. 12. (a) SEM, (b) optical absorbance, and (c) TRPL decay curves of K-doped $CsPbI_2Br$-based films. Reproduced with permission [80]; copyright 2017, American Chemical Society. (d) SEM images of $CsPbI_2Br$ and $CsPb_{1-x}Sr_xI_2Br$ films and (e) J–V, PCE, and EQE curves of $CsPbI_2Br$- and $CsPb_{1-x}Sr_xI_2Br$-based PSCs. Reproduced with permission [81]; copyright 2017, Wiley-VCH.

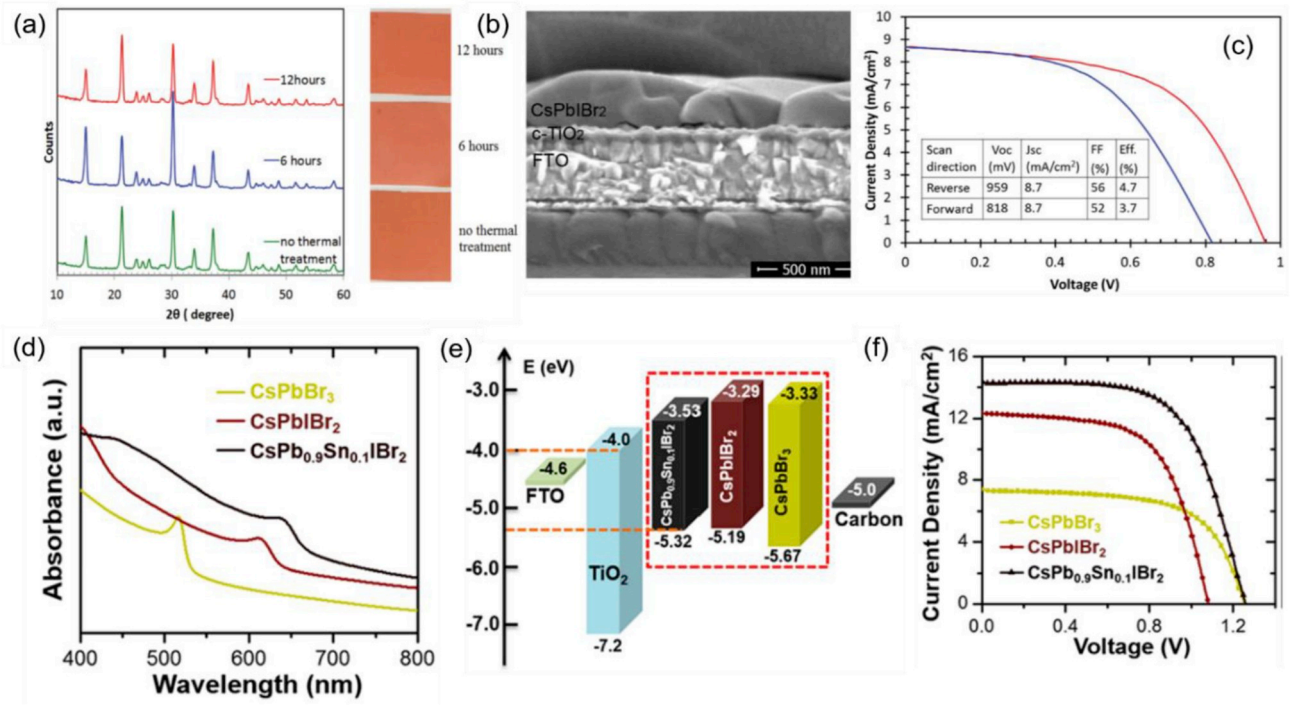

Fig. 13. (a) XRD patterns and photographs of $CsPbIBr_2$ films with and without thermal treatment. (b) SEM images of the PSC structure and (c) J–V curves of $CsPbIBr_2$-based PSCs. Reproduced with permission [82]; copyright 2016, Wiley-VCH. (d) Optical absorption and (e) energy level band diagrams of $CsPbBr_3$, $CsPbIBr_2$, and $CsPb_{0.9}Sn_{0.1}IBr_2$ films and (f) J–V curves of their respective PSCs. Reproduced with permission [84]; copyright 2017, American Chemical Society.

HTL, resulting in severe interfacial recombination (Fig. 13c). Lau et al. overcame this problem using a Spiro-OMeTAD layer as HTL and obtained a PCE of 6.3% [83]. In addition, to tune the bandgap of $CsPbIBr_2$ and enhance structural stability, partial substitution of Sn with Pb was reported by Liang et al. [84]. The addition of Sn into the $CsPbIBr_2$ perovskite ($CsPb_{0.9}Sn_{0.1}I\ Br_2$) reduced the bandgap to 1.79 eV, close to that of $CsPbI_3$, and increased the stability (Fig. 13d). A PSC device with a structure of FTO/m-TiO_2/$CsPb_{0.9}Sn_{0.1}IBr_2$/C_{60} showed a PCE of 11.33% and V_{oc} of 1.26 V, which is an exceptional record for a device without an HTL layer (Fig. 13e and f). Furthermore, the PSCs (without any encapsulation) showed extremely high stability under continuous operation in the presence of heat (100 °C for two weeks) and moisture (60% RH for 50 h). In particular, no degradation was observed for the encapsulated PSCs at room temperature, and the devices maintained their initial performance over three months.

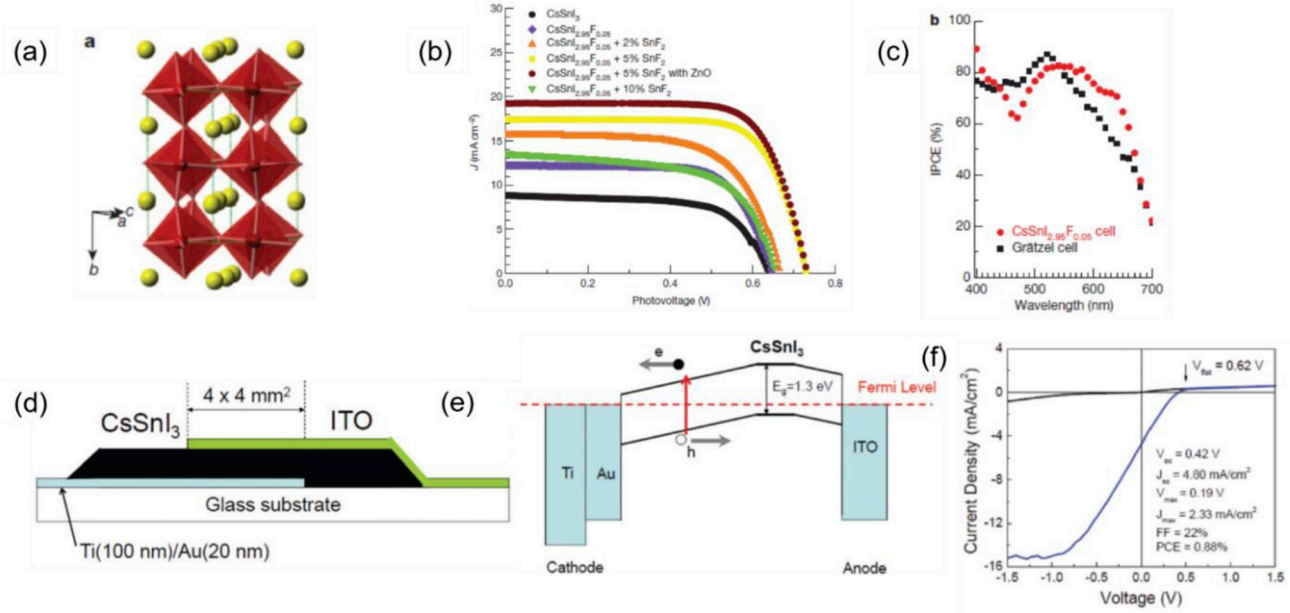

Fig. 14. (a) Schematic crystal structure of $CsSnI_3$ perovskites, J–V curve and photocurrent of DSSCs based on $CsSnI_3$ liquid electrolyte. Reproduced with permission [90]; copyright 2012, Nature Publishing Group. (d) Device structure, band alignment, and J–V curve of $CsSnI_3$-based Schottky solar cells. Reproduced with permission [91]; copyright 2012, American Institute of Physics.

3.5. $CsSnI_3$ PSCs

Despite the exciting progress in Pb-based PSCs, concerns regarding the toxicity of Pb have motivated the development of alternative Pb-free halide PSCs. For example, Pb was replaced by Sn ions in $CsPbI_3$, resulting in the formation of $CsSnI_3$ perovskites, which generally form two polymorphs: a black orthorhombic phase (B-γ-$CsSnI_3$) with a 3D perovskite structure; and a yellow phase with a 1D double-chain structure (Y-$CsSnI_3$) (Fig. 14a) [85]. The γ-$CsSnI_3$ phase has a bandgap of 1.3 eV, with a high optical absorption coefficient of 10^4 cm^{-1} and low exciton binding energy of 18 meV, which makes $CsSnI_3$ perfectly suited for PSC applications [86–88]. Furthermore, a $CsSnI_3$ structure deficient in Sn produces a good p-type conductor with a carrier concentration of ~10^{17} cm^{-3} and hole mobility of ~585 $cm^2V^{-1}s^{-1}$ [89]. Due to its good p-type conductivity, Chung et al. first used $CsSnI_3$ as a solid electrolyte in dye-sensitized solar cells (DSSCs), where $CsSnI_3$ was synthesized by a vacuum melt process at 450 °C, and obtained a PCE of 10.2% with high photocurrent. (Fig. 14b, and 14c) [90]. They observed that $CsSnI_3$ had good light absorption over the long wavelength range and was able to convert the absorbed light into photocurrent, which makes it suitable for the fabrication of tandem solar cells. Following this, Schottky-type solar cells based on a $CsSnI_3$ light absorber were reported by Chen et al., with a device structure of ITO/$CsSnI_3$/Au/Ti (Fig. 14d, and 14e) [91]. The $CsSnI_3$ layer was synthesized by sequentially depositing the CsI and $SnCl_2$ layers, followed by a thermal annealing process with a temperature of 175 °C. The PCE of the device with this type of perovskite layer was about 0.88% (Fig. 14f).

The demonstration of the promising bandgap, good light absorption properties, and acceptable photovoltaic performance of $CsSnI_3$ perovskites led to several further studies of $CsSnI_3$-based PSCs. Kumar et al. first reported PSCs using $CsSnI_3$ as the active light absorber layer with a device structure of FTO/mp-TiO_2/$CsSnI_3$/HTL/Au (Fig. 15a) [92]. The perovskite layer was deposited using a one-step solution method and a low annealing temperature (70 °C). In addition, SnF_2 was added in order to reduce the number of intrinsic defects associated with Sn vacancies (V_{Sn}) that generate high background carrier concentration and high charge recombination in $CsSnI_3$ perovskites [89,93]. The addition of SnF_2 reduced V_{Sn} without entering the $CsSnI_3$ perovskite lattice (Fig. 15b). The photovoltaic performance was considerably enhanced with an optimal concentration (20%) of SnF_2, which resulted in a PCE of 2.02%, J_{sc} of 22.70 mA/cm^2, V_{oc} of 0.24 V, and FF of 0.37 (Fig. 15c). However, it was proposed that the low photovoltaic performance was due to trap-assisted recombination, rather than any significant energy barrier in the device.

The poor film quality, high V_{Sn}, and lack of understanding of the physics of $CsSnI_3$ perovskite materials limit the performance of $CsSnI_3$ PSCs. To address these issues, Wang et al. developed a simple solution-based method where $CsSnI_3$ was dissolved in a mixture of different solvents, such as methoxyactonitrile, DMF, and acetonitrile [94]. Various post-annealing temperatures were also used to control the film quality and the V_{Sn}. The grain size increased with increasing post-annealing temperature and the grains were coarsened over an annealing temperature of 250 °C (Fig. 15d). Several device structures, such as mesoporous scaffolds (TiO_2 or Al_2O_3), and n-i-p and p-i-n planar PSCs, were fabricated and their performance was evaluated (Fig. 15e and g). The PCE values of the PSCs with mesoporous structures were very low (Fig. 15f) (0% for TiO_2 and 0.3% for Al_2O_3), which could have been due to: (i) insufficient pore filling; (ii) constrained crystallization environment in the mesoporous scaffolds; and (iii) low crystallinity impurities (Y-$CsSnI_3$ and Cs_2SnI_6). To overcome these issues, a planar device structure of ITO/c-TiO_2/$CsSnI_3$/Spiro-MeOTAD was fabricated, and an improved PCE of 0.77% was achieved. However, the device performance was still low due to the low conductivity of undoped Spiro-MeOTAD, which limited the hole conductivity and carrier transport. The Spiro-MeOTAD was undoped here to avoid the degradation of γ-$CsSnI_3$ induced by the oxidation steps required to dope Spiro-MeOTAD. To avoid the challenges related to the use of Spiro-MeOTAD in γ-$CsSnI_3$-based PSCs, a compact NiO_x HTL and PCBM

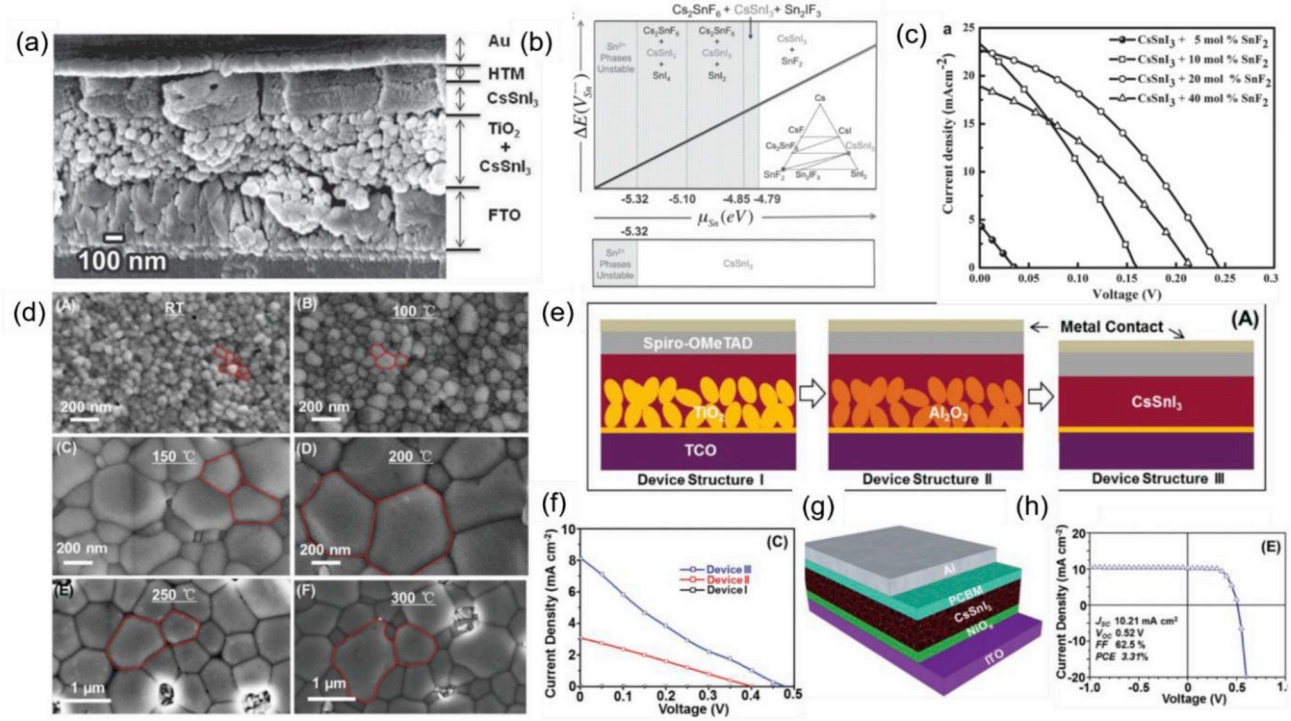

Fig. 15. (a) Cross-sectional FESEM images, calculated variation in V_{Sn} formation energy, and J–V curves of $CsSnI_3$-based PSCs with different concentrations of SnF_2. Reproduced with permission [92]; copyright 2014, Wiley-VCH. (d) SEM images of the B-γ-$CsSnI_3$ perovskite thin films annealed at different temperatures, (e), (f) device structure and J-V curves of the perovskite solar cells, and (g), (h) device structure and J–V curves of an inverted planar device with NiO_x as HTL and PCE of $CsSnI_3$-based PSCs. Reproduced with permission [94]; copyright 2016, Wiley-VCH.

ETL were used, which significantly increased the PCE to 3.0% (Fig. 15h). The annealing temperature had a significant impact on the device performance; a temperature of 150 °C was optimal for producing a smooth surface and uniform crystals, which resulted in improved device performance. Annealing at higher temperatures produced larger crystals, but increased the V_{Sn} content and film roughness, which reduced the carrier lifetime and degraded the interfacial contact, respectively.

The susceptibility of Sn-based perovskites to oxidation, their low energy of defect formation, and difficulties in producing pinhole-free films limit the performance and stability of $CsSnI_3$-based PSCs. To address these challenges, Marshall et al. systematically studied the addition of Sn halides (e.g., SnI_2, $SnBr_2$, $SnCl_2$, and SnF_2) to $CsSnI_3$ solutions [95]. First, they added an excess of SnI_2 to $CsSnI_3$ precursor solutions and investigated the effect on the $CsSnI_3$ film morphology and device performance. The addition of 10% of SnI_2 increased the PCE of the $CsSnI_3$ PSCs. A plausible mechanism for PCE enhancement was described in terms of suppression of carrier recombination due to the reduced V_{Sn} content in the Sn-rich perovskite films. As a result, a PCE of 2.76% and V_{oc} of 0.55 V were achieved using CuI and ICBA as HTL and ETL, respectively. Among the Sn halide additives, the use of $SnBr_2$ and SnF_2 produced PSCs with poor device performance (PCE of only 0.4%). However, $SnCl_2$ was a beneficial additive and showed the most significant effects on $CsSnI_3$ perovskite film and PSC performance. The addition of $SnCl_2$ did not improve the morphology of the $CsSnI_3$ perovskite film (pinholes were still observed; Fig. 16a) compared to those prepared with SnI_2, $SnBr_2$, and SnF_2 additives; however, the photovoltaic performance did not seem to be degraded by the poor morphology. Further analysis indicated that a $SnCl_2$ layer was formed on the $CsSnI_3$ film, instead of forming $CsSnCl_3$ or $CsSnI_{3-x}Cl_x$, which may have occurred due to a large difference between the ionic radii of Cl (1.81 Å) and I (2.2 Å). This $SnCl_2$ layer was sacrificed to form a stable hydrate and SnO_2 that protected the underlying $CsSnI_3$ layer from oxidation upon exposure to air. This work provided further evidence for the hypothesis that the presence of excess $SnCl_2$ at the surface of $CsSnI_3$ crystallites resulted in moderate n-doping of the fullerene layer, resulting in the formation of a Schottky barrier that prevents unwanted extraction of electrons from the fullerene into the ITO at the pinhole sites (Fig. 16b). Therefore, carrier recombination at the exposed ITO sites was significantly reduced, and the PCE of the $CsSnI_3$ device increased to 3.56% without an electron blocking layer (Fig. 16c). Consequently, the stability of the unencapsulated $CsSnI_3$ PSC devices tested in ambient air at a humidity of ~25% under constant 1 sun simulated solar simulation also increased with the addition of the $SnCl_2$ layer (Fig. 16d).

3.6. $CsSnBr_3$ PSCs

Similar to $CsPbX_3$ (X= I, Br, Cl) perovskites, the bandgap of $CsSnX_3$ perovskites can be tuned by changing the X elements. The bandgap of $CsSnX_3$ can be varied from 1.3 eV to 1.75 eV by substituting I with Br, resulting in a significant increase in V_{oc} of the PSCs (Fig. 17a). Gupta et al. investigated $CsSnBr_3$ PSCs [96], where the perovskite absorber layer was prepared using a one-step solution method using mp-TiO_2 and Spiro-MeOTAD as an ETL and HTL, respectively. In addition, the effects of SnF_2 incorporation on the $CsSnBr_3$ film properties and PSC performance were investigated. The addition of SnF_2 reduced the background carrier density by neutralizing carrier traps induced by V_{Sn} and reduced the work function of $CsPbBr_3$, resulting in conduction band (CB) and valence band (VB) energies closer to the CB of the ETL and VB of the HTL, respectively, which facilitated carrier transport at the interfaces (Fig. 17b). As a result, the PCE increased from 0.01% to 2.1% (Fig. 17c). In addition, the oxidation of Sn from X-ray radiation was prevented, and the stability of the perovskite in an inert atmosphere increased with the addition of SnF_2 and without any encapsulation.

To prevent the oxidation of Sn^{2+} ions to Sn^{4+} ions in $CsSnX_3$ perovskites, the addition of excess SnF_2 or $SnCl_2$ in $CsSnX_3$ perovskites results in poor film morphology, which hinders the device performance. To solve this problem, Song et al. designed a novel and effective method in which an atmosphere with a reducing vapor of hydrazine (N_2H_4) was introduced during spin coating of the $CsSnBr_3$ and $CsSnI_3$ perovskite precursors, as shown in Fig. 17d [97]. The proposed reaction path in the reducing atmosphere during film formation was $2SnI_6^{2-} + N_2H_4 \rightarrow 2SnI_4^{2-} + N_2 + 4HI$ (Fig. 17e), which resulted in more than 20% reduction in the Sn^{4+}/Sn^{2+} ratio, which dramatically suppressed the carrier recombination induced by the undesirable p-type electrical conductivity of V_{Sn}. As a result, PCE values of 1.83% and 3.04% for the $CsSnI_3$- and $CsSnBr_3$-based PSCs were achieved, respectively. Later, the

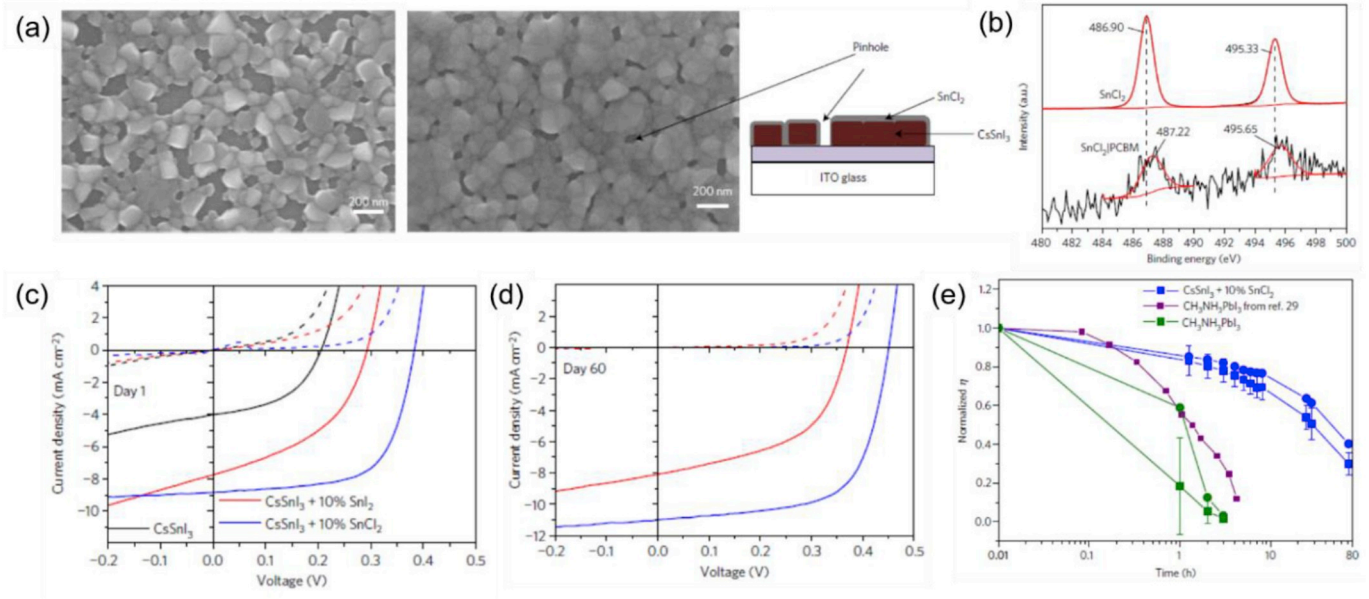

Fig. 16. (a) SEM images of $CsSnI_3$ perovskite films with and without 10 mol% $SnCl_2$ added, along with a schematic diagram of $SnCl_2$-capped $CsSnI_3$ crystallites. (b) High-resolution XPS spectra of $SnCl_2$ and $SnCl_2$-doped PCBM films used to investigate n-type doping. (c) J–V curves of fresh $CsSnI_3$-based PSCs, (d) the stability of PCE after storing in nitrogen atmosphere, and (e) time-dependent normalized PCE of the devices tested under a 1 sun solar simulator in ambient air without encapsulation. Reproduced with permission [95]; copyright 2016, Nature Publishing Group.

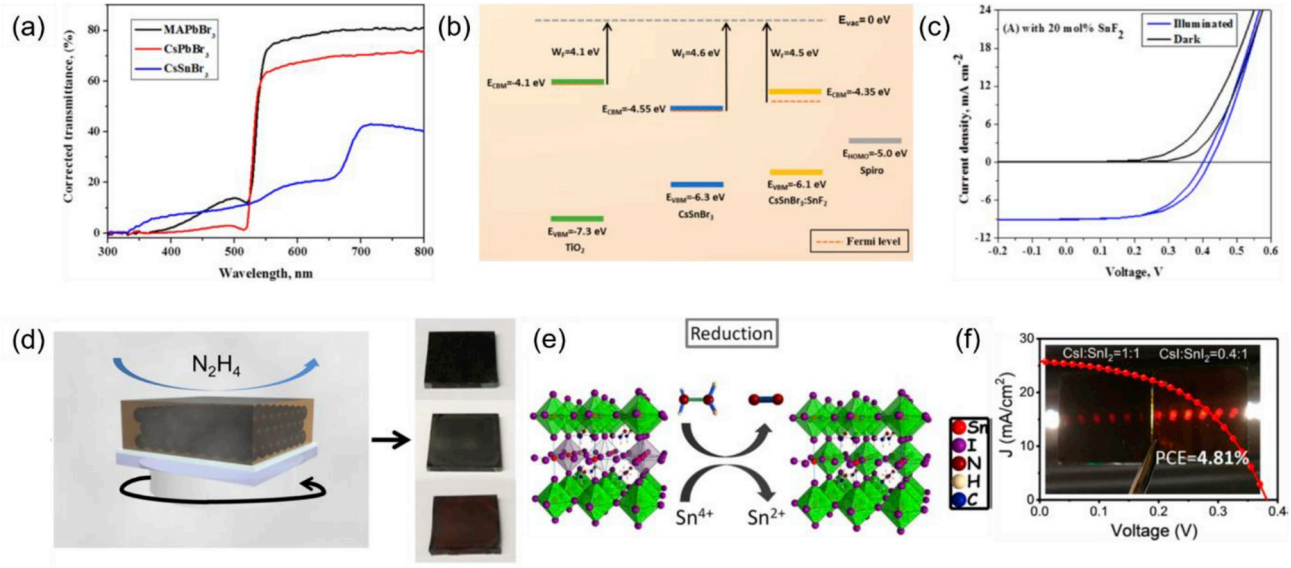

Fig. 17. (a) Reflection-corrected normalized transmittance spectra of $CsSnBr_3$, $CsPbBr_3$, and $MAPbBr_3$ films. (b) Band diagram of $CsSnBr_3$ with and without 20 mol% SnF_2 added. (c) J–V curves of $CsSnBr_3$-based PSCs with and without added SnF_2. Reproduced with permission [96]; copyright 2016, American Chemical Society. (d) Schematic diagram of reducing atmosphere process for preparation of (top) $MASnI_3$, (middle) $CsSnI_3$, and (bottom) $CsSnBr_3$. (e) Proposed mechanism of hydrazine vapor reaction with Sn-based perovskite materials. (f) J–V curves of $CsSnBr_3$ PSCs with and without various hydrazine vapor concentrations. Reproduced with permission [97]]; copyright 2017, American Chemical Society.

same group reported that excess SnI_2 was dispersed uniformly in the perovskite film (instead of using SnF_2 to reduce the V_{Sn}) under a reducing atmosphere of N_2H_4. The excess SnI_2 in the perovskite film decreased p-type conductivity by compensating Sn^{2+} vacancies [98]. The $CsSnI_3$ PSCs (optimal concentration of 0.4 M CsI and 1.0 M SnI_2) fabricated using this approach demonstrated a highest efficiency of 4.81% (Fig. 17f).

3.7. $CsSnI_{3-x}Br_x$ PSCs

$CsSnI_3$ is a widely investigated lead-free halide inorganic perovskite that functions as an efficient light absorber with high photocurrent. However, the PCE of $CsSnI_3$ inorganic PSCs is limited by the low V_{oc}. To overcome this, Sabba et al. proposed increasing the V_{oc} by chemically doping Br in $CsSnI_3$ to form $CsSnI_{3-x}Br_x$ ($0 \leq x \leq 3$) [99]. Br doping transformed the crystal structure from the orthorhombic to cubic phase, from $CsSnI_3$ to $CsSnBr_3$, respectively. The optical bandgap transitions

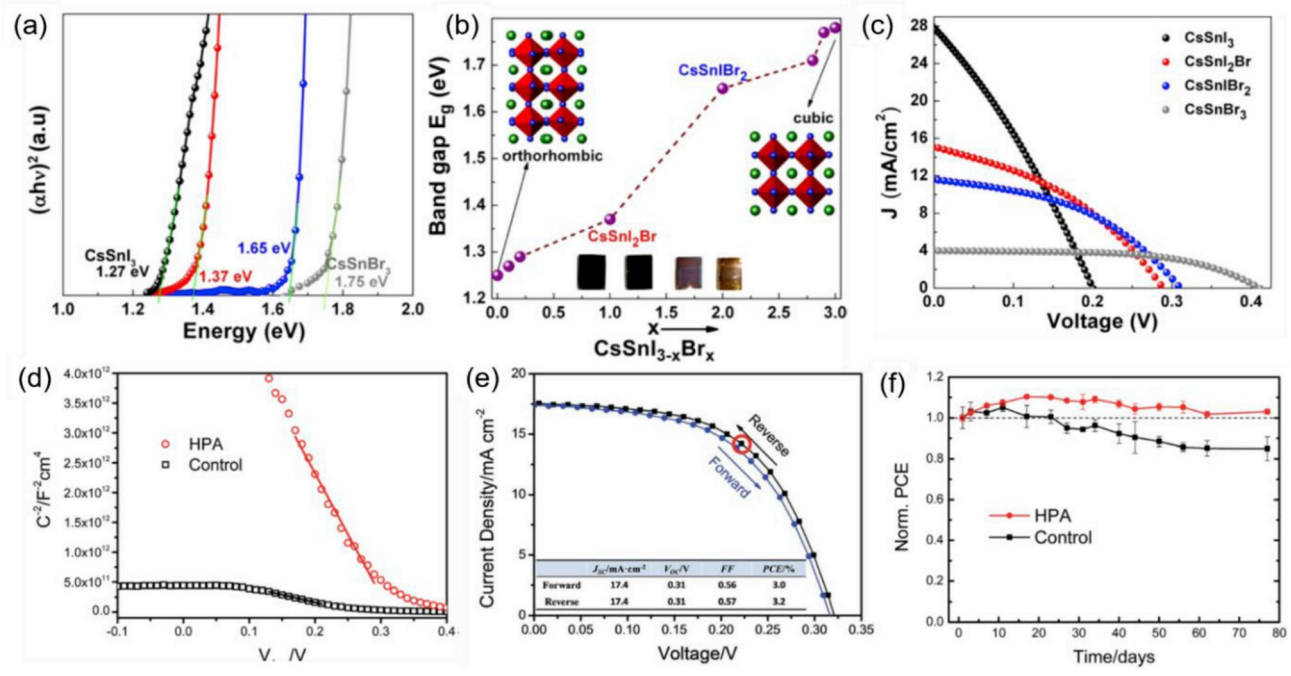

Fig. 18. (a) Tauc plots of $CsSnI_{3-x}Br_x$ with different concentration of Br, (b) bandgap variation with-respect-to Br concentration, (c) J-V curves of $CsSnI_{3-x}Br_x$ PSCs. Reproduced with permission [99]. Copyright 2015, American Chemical Society. (d) Mott-Schottky plots of $CsSnIBr_2$ PSCs used to calculate the carrier density. (e) J–V curves, and (f) normalized PCEs of encapsulated $CsSnIBr_2$ PSCs with and without HPA additives under ambient conditions. Reproduced with permission [100]; copyright 2016, The Royal Society of Chemistry.

increased with increasing Br concentration from 1.27 eV for $CsSnI_3$ to 1.37, 1.65, and 1.75 eV for $CsSnI_2Br$, $CsSnIBr_2$, and $CsSnBr_3$, respectively (Fig. 18a and b). Br doping also significantly reduced the structural disorder of the $CsSnI_{3-x}Br_x$ perovskite (deduced from the Urbach energy), decreased the charge carrier density (6.32×10^{15} cm^{-3}), and increased the charge recombination resistance, which increased the V_{oc} of $CsSnI_{3-x}Br_x$ PSCs. Further addition of SnF_2 (20 mol%) into $CsSnI_2Br$ significantly suppressed the V_{Sn} concentration, which reduced carrier recombination and increased the photocurrent densities. As a result, the PCE was consequently enhanced, with a value of 1.67% (Fig. 18c). In addition, they achieved the PCE with a highest value of 1.76% for the $CsSnI_{2.9}Br_{0.1}$ inorganic base PSCs.

To further overcome the instability and bulk recombination induced by V_{Sn} defects in Sn-based inorganic PSCs, Li et al. introduced hypophosphoric acid (HPA) into the $CsSnIBr_2$ perovskite precursor solution [100]. The HPA additive worked as a complexant to enhance the nucleation process with inhibiting the formation of Sn^{4+} ions during formation of the $CsSnIBr_2$ film; this remarkably reduced the carrier mobility and carrier density in the perovskite film (Fig. 18d). When the perovskite film with the HPA additive was applied in PSCs, the V_{oc} and FF were significantly increased; a PCE of 3.2% was achieved with a mesoporous PSC architecture, which was two times higher than the equivalent device without HPA addition (Fig. 18e). Furthermore, the PSC with HPA-doped $CsSnIBr_2$ film combined with a carbon electrode resulted in impressive stability, with no efficiency loss over 77 d. The encapsulated devices also exhibited superior thermal stability, maintaining 98% of the initial PCE after 9 h continuous power output at 473 K (Fig. 18f).

It is clear from these studies that the efficiency and stability of the Pb- and Sn-based inorganic PSCs have dramatically improved in a short period. The efficiency values of $CsPbX_3$ and $CsSnX_3$ PSCs have been increased to over 17% and 4%, respectively, under rigorous experimental conditions. The bandgap and structural stability of $CsPbX_3$ and $CsSnX_3$ PSCs have been optimized by the partial substitution of metal cations or halide anions. In addition, the incorporation of several additives, including ligands, polymers, and ammonia salts, effectively enhanced phase stabilization of these perovskites.

4. Solvent engineering and deposition techniques

Several deposition techniques have been demonstrated for preparation of organic–inorganic hybrid PSCs, such as a two-step sequential method [12], antisolvent-washing [13], evaporation [14], and chemical vapor deposition (CVD) [15], which have been widely implemented to overcome the poor solubility between the organic (MAI, MABr, FAI, FABr) and inorganic (PbI_2, $PbBr_2$) elements. However, in the case of the $CsPbX_3$-and $CsSnX_3$-based inorganic perovskites, the major challenge is related to the poor solubility of the Cs and Br precursors that limits the deposition of a sufficiently thick and pinhole-free perovskite film for solar cell applications. Therefore, well-controlled solvent engineering and optimized deposition methods are critical for producing high-quality films. In this section, we thoroughly review recent achievements in solvent engineering for solution-based processing techniques, along with vacuum deposition methods for the fabrication of high-quality inorganic perovskite films and their PSC applications.

The large concentration difference between $PbBr_2$ and CsBr solution forms CsBr-rich Cs_4PbBr_6 insulating phase in $CsPbBr_3$ perovskites which significantly limits the PCE of $CsPbBr_3$ based all inorganic PSCs. To overcome the formation of Cs_4PbBr_6 insulating phase in $CsPbBr_3$ perovskite films, a multistep solution-processing method was developed by Duan et al. They fabricated high-purity $CsPbBr_3$ inorganic perovskite films by multiple times (n) of CsBr spin-coating on $PbBr_2$-coated substrates (Fig. 19a) [101]. A monolayer with vertically aligned $CsPbBr_3$ grains was achieved with an optimized number of CsBr coating. For example, for $n \leq 3$, $CsPb_2Br_5$ phases were observed which further transitioned to $CsPbBr_3$ for $n = 4$, and Cs_4PbBr_6 for $n \geq 5$, as shown in Fig. 19b. The multiple times of CsBr coating on the $PbBr_2$ devolved a transformation mechanism: phase fusion and separation of perovskite i.e. $PbBr_2 \rightarrow CsPb_2Br_5 \rightarrow CsPbBr_3 \rightarrow Cs_4PbBr_6$, as shown in Eqs. (6)–(8).

$$2PbBr_2 + CsBr \rightarrow CsPb_2Br_5 \ (n \leq 3) \quad (6)$$

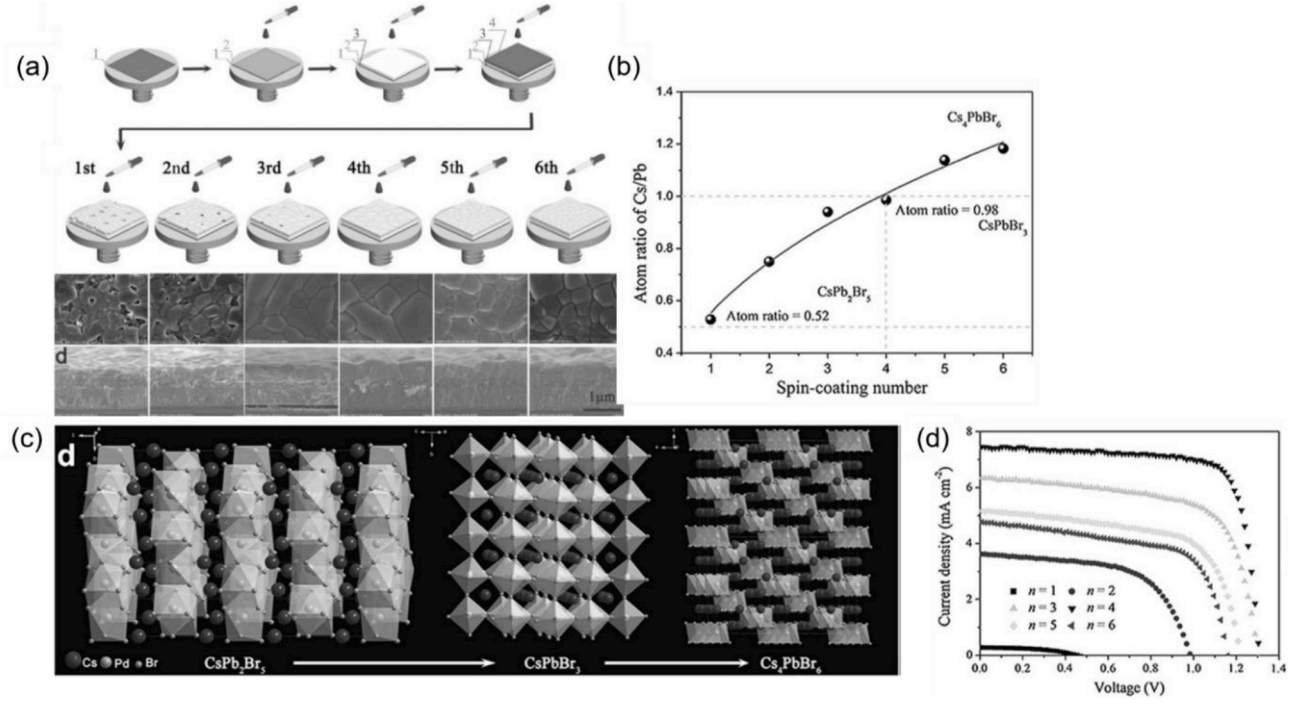

Fig. 19. (a) Schematic of the deposition process and SEM images of a $CsPbBr_3$ film. (b) Atomic ratios of Cs/Pb for different deposition cycles. (c) Schematic of the crystal structure of cesium lead bromide halide. (d) J–V curves of the $CsPbBr_3$-based PSCs made at different coating cycles. Reproduced with permission [101]]; copyright 2018, Wiley-VCH.

$$CsPb_2Br_5 + CsBr \rightarrow 2CsPbBr_3 \ (n = 4) \quad (7)$$

$$CsPbBr_3 + 3CsBr \rightarrow Cs_4PbBr_6 \ (n \geq 5) \quad (8)$$

At n = 4, the film coverage and grain sizes were better than for n < 4, n > 4 and the film showed a highly phase-pure crystal structure (Fig. 19c). The all-inorganic PSCs fabricated with this $CsPbBr_3$ (n = 4) perovskite film and a carbon electrode showed a PCE of 7.54% and V_{oc} of 1.308 V (Fig. 19d), whereas the PCE of the devices fabricated for n<4 and n>4 was deteriorated due to the formation of $CsPb_2Br_5$ and Cs_4PbBr_6 phases, respectively. These results indicate that this multistep solution-processing method was very effective for producing high-quality $CsPbBr_3$ inorganic perovskite films for PSC applications.

In order to overcome the solubility limit of Br in conventional solution-based processing, Luo et al. developed a Br_2-vapor-assisted CVD method and investigated the fast anion exchange from $CsPbI_3$ to $CsPbBr_3$ [102]. The Br_2 vapor was injected into a hot quartz chamber containing a $CsPbI_3$-coated FTO/TiO_2 substrate and reacted at 150 °C for a certain time (Fig. 20a). Under this Br_2 vapor, $CsPbI_3$ reacted to form $CsPbBr_3$ via the following reaction:

$$CsPbI_3 + Br_2 = CsPbBr_3 + I_2 \ (g) \quad (9)$$

The transition from $CsPbI_3$ to $CsPbBr_3$ was confirmed by both XRD and absorption spectra of the perovskite film. The plausible mechanism proposed by the authors was that the α-$CsPbI_3$ phase changed to δ-$CsPbI_3$ at 150 °C, which reacted with the Br_2 vapor to form the highly pure cubic phase of $CsPbBr_3$, which exhibited optical absorption at 523 nm. The $CsPbBr_3$ perovskite film maintained the highly stable cubic phase under further heating to 300 °C, indicating excellent thermal stability (Fig. 20b). The PSCs fabricated using this CVD-grown $CsPbBr_3$ film and a carbon electrode under ambient conditions showed a PCE of 5.38% (Fig. 20c) and showed excellent stability. The Br_2-vapor-assisted CVD method is a novel approach for developing a stable inorganic perovskite film.

Notably, a high temperature of 250 °C is required to crystalize $CsPbBr_3$ thin films, which results in a high fabrication cost and makes it unsuitable for preparation of flexible devices. To address this problem, Tang et al. developed a two-step process to fabricate inorganic PSCs at low temperature by treating $PbBr_2$ films with pyridine (Py) vapor [103]. They proposed that Py could act as a ligand to form intermediate phases with $PbBr_2$ films by reducing the activation energy; this facilitated the formation of the $CsPbBr_3$ perovskite film at low temperature through an alternative reaction pathway (Fig. 20d). The average grain size of a $CsPbBr_3$ film after treatment with Py annealing at 160 °C was 450 nm, which was similar to that of the perovskite film annealed at 250 °C; hence, Py treatment successfully reduced the annealing temperature of the $CsPbBr_3$ film, while large grains were obtained (Fig. 20e). PSCs fabricated with the Py-treated $CsPbBr_3$ films showed great potential for practical applications, with a PCE of 6.05% and V_{oc} of 1.34 V (Fig. 20f), along with excellent stability in ambient air (RH: 40–70%, RT) without any encapsulation.

To overcome the limitations of conventional spin-coating processes, Ramadan et al. investigated the effect of different solvents (DMF, DMSO, and mixtures of these) on the structural, morphological, and electronic properties of the $CsPbI_3$ perovskite films [104]. An optimal solvent mixture of 2:1 vol% DMF:DMSO produced higher quality $CsPbI_3$ films than the use of only DMF or DMSO solvents, which resulted in low surface coverage, the presence of crystalline PbI_2, and rough surfaces with pinholes (Fig. 21a). The depth profile analyzed using secondary ion mass spectroscopy (SIMS) showed a gradual slope for the Cs, Pb, and I ions throughout the film, indicating an even distribution of elements (Fig. 21b). Similarly, the low-energy ion sputtering (LEIS) intensity of the $CsPbI_3$ film obtained using the DMF and DMSO solvent mixture showed that Cs, Pb, and I ions were stoichiometrically balanced (molar ratio of 1:1:3 for Cs:Pb:I) (Fig. 21c). Hence, the SIMS and LEIS results strongly indicated that the DMF-DMSO solvent mixture produced highly crystalline $CsPbI_3$. Furthermore, this report argued that a thorough understanding of the fundamental structure of $CsPbI_3$ and good control of the solvent system are required in order to further improve its photovoltaic performance.

The stabilization of the black α-$CsPbI_3$ phase in ambient air remains a difficult challenge. Luo et al. achieved stable operational $CsPbI_3$ PSCs fabricated via a sequential solvent engineering and low-temperature processing method involving addition of HI to the $CsPbI_3$ perovskite precursor solution and treatment with isopropyl alcohol (IPA) [105].

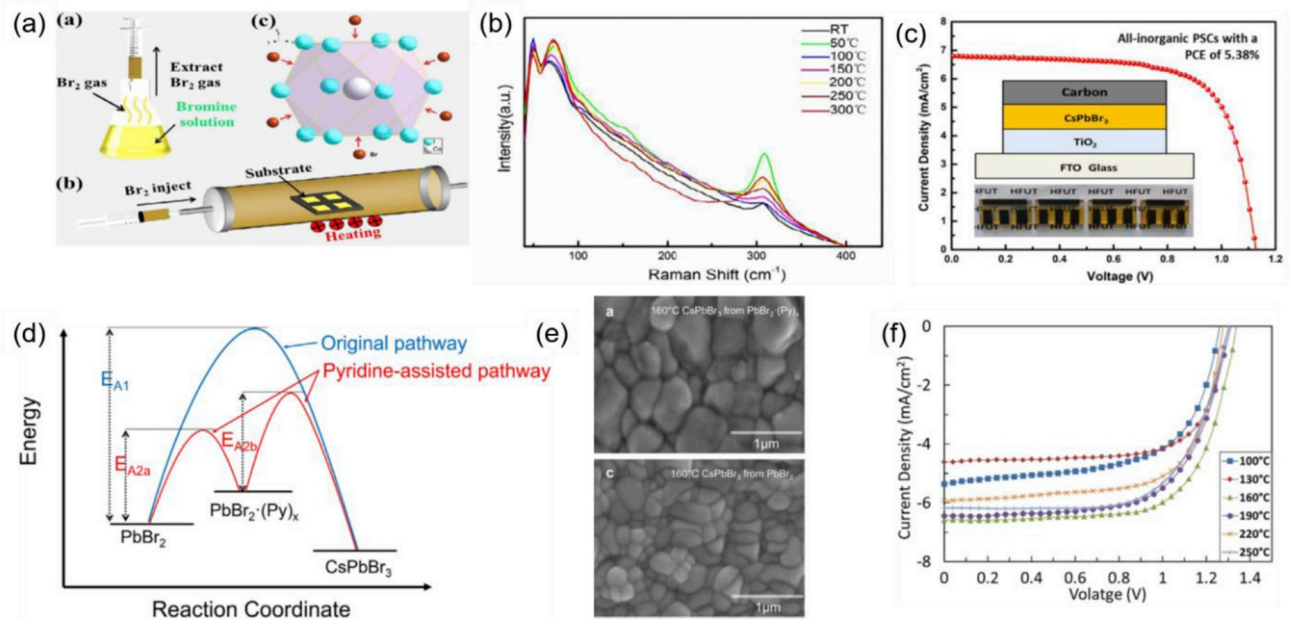

Fig. 20. (a) Schematic of the process for fabricating $CsPbBr_3$ films using Br_2-vapor-assisted CVD and its crystal structure. (b) Raman spectra of $CsPbBr_3$ films processed at different temperatures. (c) J–V curves of $CsPbBr_3$ PSCs and (inset) schematic of the device structure. Reproduced with permission [102]; copyright 2018, Elsevier. (d) The reaction coordinate diagram of the conversion from Py-assisted $PbBr_2$ to $CsPbBr_3$ perovskite. (e) SEM images of $CsPbBr_3$ films with and without pyridine treatment. (f) J–V curves of pyridine-treated $CsPbBr_3$-based PSCs after annealing at various temperatures. Reproduced with permission [103]; copyright 2018, Wiley-VCH.

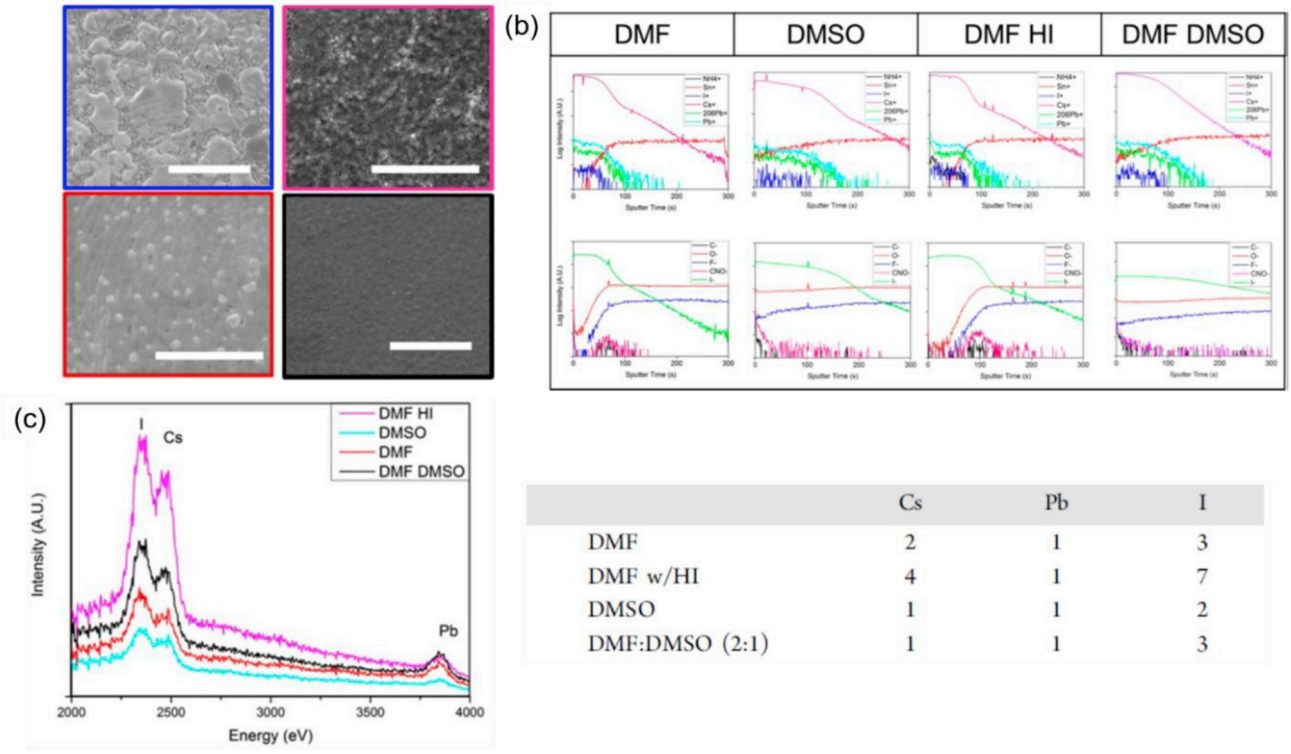

	Cs	Pb	I
DMF	2	1	3
DMF w/HI	4	1	7
DMSO	1	1	2
DMF:DMSO (2:1)	1	1	3

Fig. 21. (a) SEM images, (b) SIMS results, and (c) LEIS spectra of $CsPbI_3$ films prepared using DMF and DMSO solvents. Reproduced with permission [104]; copyright 2017, American Chemical Society.

XRD analysis suggested that the addition of HI resulted in an intermediate Cs_4PbI_6 phase that reacted completely to form the stable cubic phase of $CsPbI_3$ when treated with hot IPA solution and annealed at 100 °C (Fig. 22a). Hence, the intermediate Cs_4PbI_6 phase played a significant role in developing the phase stability of the $CsPbI_3$ film, which was stable for 72 h upon continuous exposure to air (RH: <30%) and

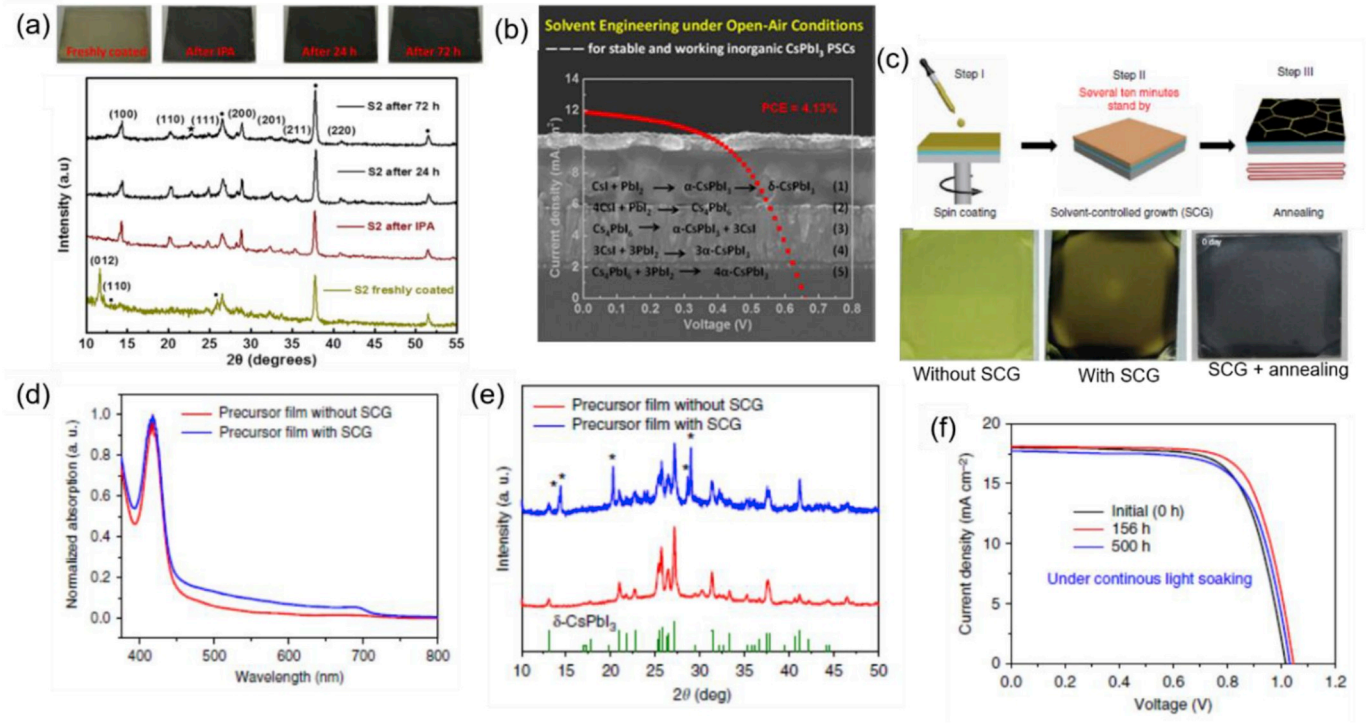

Fig. 22. (a) Photographs and XRD patterns of the IPA-treated $CsPbI_3$ films with and without exposure to air. (b) J–V and PCE curves of IPA-treated $CsPbI_3$-based PSC. Reproduced with permission [105]; copyright 2016, American Chemical Society. (c) Schematic and photographs of the SCG $CsPbI_3$ films before and after annealing; (d) absorption spectra and (e) XRD patterns of $CsPbI_3$ films with and without SCG; (f) J–V curves of the unencapsulated $CsPbI_3$ PSCs under continuous light soaking for several hours in a nitrogen atmosphere. Reproduced with permission [106]; copyright 2018, Nature Publishing Group.

achieved a PCE of 4.13% without any encapsulation (Fig. 22b).

It is imperative to form highly crystalline, pinhole-free perovskite films of the highly stable α-phase of $CsPbI_3$ to improve the PCE of PSCs. A solvent control growth (SCG) method was reported by Wang et al. for producing high-quality α-phase $CsPbI_3$ thin films (Fig. 22c) [106]. They suggested that the DMSO solvent could not be completely removed from the precursor film due to its high boiling point (189 °C). Residual DMSO in the film could enhance mass transport and diffusion processes and improve the film quality by reducing the evaporation rate. The $CsPbI_3$ films were dried in a nitrogen-filled glovebox for several tens of minutes before annealing, which resulted in gray films with an absorption peak at the wavelength of 720 nm similar to that of the α-phase $CsPbI_3$ (Fig. 22d). The XRD pattern revealed that the SCG process exhibited a partial phase change from the δ-phase to β-phase $CsPbI_3$ due to diffusion of the perovskite materials and reconstruction of the perovskite film (Fig. 22e). This process enhanced mass transport and resulted in high-quality films that were uniform and free of pinholes. The optimal $CsPbI_3$ perovskite film (with an SCG time of 50 min) was used to fabricate PSC devices with a structure of ITO/SnO_2/$CsPbI_3$/Spiro-OMeTAD/Au, which showed a high PCE of 15.71%. The SCG method was also used to fabricate high-quality $CsPbI_{3-x}Br_x$ and $CsPbBr_3$ films, and excellent PCE values of 16.14% and 9.8% were achieved, respectively. Interestingly, the PSCs (without encapsulation) showed excellent photostability under continuous illumination in a nitrogen atmosphere at RT (Fig. 22f). Similar approaches using DMSO-controlled solvent engineering methods have also been recently reported, where highly crystalline, pinhole-free, and defect less $CsPbI_2Br$ films with improved device performance and stability were fabricated [107,108].

To further overcome the solubility limits, Frolova et al. investigated the fabrication of $CsPbI_3$ films by thermal co-evaporation of CsI and PbI_2 precursors under vacuum, followed by annealing at 60–320 °C (Fig. 23a) [109]. The temperature-dependent structural evolution was quantified by in situ grazing incident wide-angle X-ray scattering (GIWAXS) measurements. The film annealed at high temperature (320 °C) showed a high-quality cubic-phase with preferred orientation of the crystal structure (Fig. 23b). Scanning Kelvin probe microscopy measurements showed that high-temperature annealing of the vacuum-deposited perovskite film increased the surface potential to 645 mV, indicating a reduction in the surface defect density. Using this co-evaporation method with an optimal annealing temperature of 320 °C, stoichiometrically balanced $CsPbI_3$ PSCs were fabricated, which exhibited the highest PCE of 10.5% (Fig. 23c). In addition, similar vacuum deposition methods have been recently reported for the fabrication of $CsPbI_3$ and $CsPbI_{3-x}Br_x$ films [78,110].

The evaporation of organic/inorganic and metal halides under high vacuum is difficult to monitor and control the rate of evaporation because of the gas like behavior or the poor-sticking problem of the organic halides which hinders the device performance [111]. Thus, the evaporation methods raise a question mark on the feasible fabrication of PSCs. To overcome these issues and the solubility limit, another strategy was developed by Lau et al., which combined solution-based spin-coating and spray deposition methods [83]. $CsPbIBr_2$ films were fabricated using a two-step process in ambient air. A $PbBr_2$ film was first spin-coated on a TiO_2/FTO substrate followed by spray coating a CsI solution dissolved in methanol. A post-deposition annealing treatment was performed at 275–350 °C in air for 10 min to achieve sufficient crystallinity of the perovskite film. Perovskite films with well-balanced stoichiometry (Pb/Cs = 1, Br/I = 2) were achieved at room temperature. Furthermore, a pinhole-free surface morphology and high charge carrier lifetime was achieved for a film annealed at 300 °C, as confirmed by scanning electron microscopy (SEM) and TRPL measurements (Fig. 23d and e). The fabricated PSCs with device structure of FTO/c-TiO_2/mp-TiO_2/$CsPbIBr_2$/Spiro-OMeTAD/Au exhibited a PCE of 6.3% (Fig. 23f).

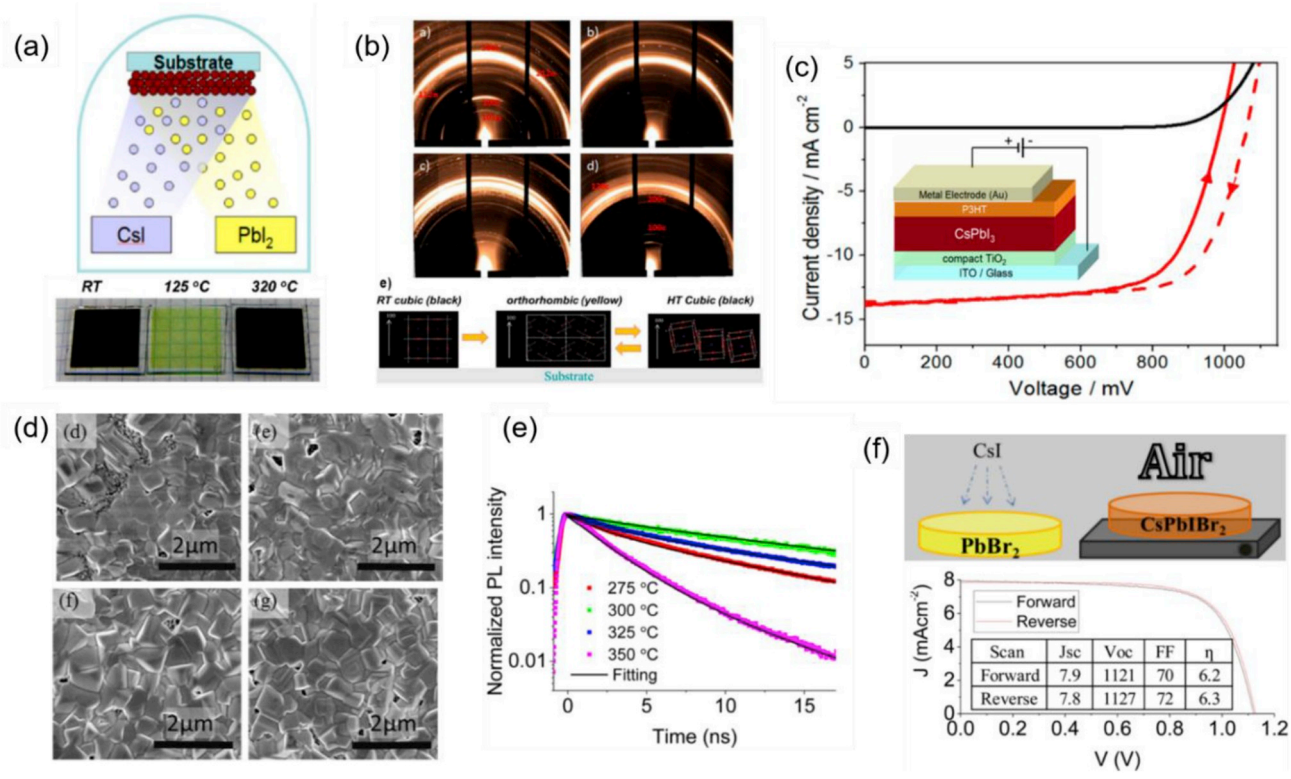

Fig. 23. (a) Schematic diagram the thermal evaporation method and photographs of the $CsPbI_3$ films without and with annealing. (b) GIWAXS spectra of $CsPbI_3$ films before and after annealing at various temperature. (c) J–V curve and device structure of $CsPbI_3$ PSCs. Reproduced with permission [109]; copyright 2017, American Chemical Society. (d) SEM images, (e) TRPL of spray-coated $CsPbI_2Br$ films, and (f) J–V curves of $CsPbI_2Br$ PSCs. Reproduced with permission [83]; copyright 2016, Wiley-VCH.

It is still challenging to produce high-quality all-inorganic perovskites using conventional solution processing due to the high phase transition temperature and low solubility of cesium halides. To overcome these issues, Zhang et al. reported a wide solution-processing method using a combination of DMSO solvent and a subsequent heating process [112]. The $CsPbI_2Br$ films were fabricated by varying the solvent components and solute concentration. The solubility of the precursors was completely dependent on the DMSO, i.e., the solubility increased with increasing DMSO fraction in the solution, which is important for controlling the thickness of the film. Under additional heating in a hot air flow (HAF), the DMSO acted as a capping agent to facilitate molecular self-assembly and uniform crystal growth of the $CsPbI_2Br$ film (Fig. 24a). XRD and SEM analyses indicated that 50% DMSO was optimum (for all solute concentrations), resulting in high-quality perovskite crystals and uniform, pinhole-free perovskite films (Fig. 24b and c). PSCs fabricated with perovskite films prepared using 50% DMSO and a solution concentration of 1 M had a PCE of 12.52 % and a remarkably high V_{oc} of 1.315 V. The wide solution-processing windows with enhanced processability indicate that this method is potentially suitable for industrial fabrication of tandem solar cells.

Antisolvent treatment methods can be very effective for producing perovskite films with dense surface morphology, large grains, and low defect density; however, such methods have not been widely adopted for fabricating inorganic PSCs. Dong et al. demonstrated the preparation of $CsPbI_2Br$ films using a green solvent, ethyl acetate (EA)-based anti-solvent process [113]. The SEM images revealed that the EA anti-solvent-processed $CsPbI_2Br$ film had full dense surface coverage with large grains, which could effectively reduce the trap densities and recombination losses (Fig. 24d). XRD patterns and optical absorption spectra of the EA-treated $CsPbI_2Br$ films showed strong α-phase peaks and direct bandgap values close to 1.91 eV, respectively, indicating a highly crystalline film with few defects (Fig. 24e). The improved morphology and crystallinity were attributed to the low boiling point (77 °C) of EA, which resulted in low residues in the precursor film that produced high-quality pinhole-free perovskite films after annealing. The performance of EA-treated PSCs was significantly improved (with a PCE of 10%), which was attributed to enhanced carrier extraction and transport (Fig. 24f). In addition, the devices without encapsulation exhibited excellent long-term stability with retaining 94% of their initial PCE when stored in ambient air (RH: 15–30%, RT) for 39 days.

In addition, an intermolecular exchange method was introduced by Zhu et al. for fabricating $CsPbIBr_2$ films [114]. This method consisted of spin coating an optimized methanol-based CsI solution on a $CsPbIBr_2$ precursor film in a conventional one-step solution process. The authors suggested that some CsI-$PbBr_2$-DMSO complexes were transformed into $CsPbIBr_2$ by intermolecular exchange of DMSO with CsI, which resulted in the formation of well-crystallized polygonal grains with an average size of 650 nm (Fig. 25a). SEM images showed that the intermolecular exchange method produced $CsPbIBr_2$ films with full uniform surface coverage. The (100) orientation of the $CsPbIBr_2$ perovskite grain (obtained from XRD analysis) seemed to be perpendicular to the substrate, which could enhance carrier transport and injection in the solar cell. The two most significant benefits of the intermolecular exchange method were highlighted: (1) full coverage of the $CsPbIBr_2$ film could only be obtained by spin coating the CsI solution; and (2) the grain size of the $CsPbIBr_2$ film depended on the concentration of the CsI solution. Furthermore, the valence-band maximum (VBM) and the work function (WF) of such $CsPbIBr_2$ films were 5.29 eV and 4.80 eV, respectively (Fig. 25b). The high WF of $CsPbIBr_2$ films formed using the intermolecular exchange method indicated that a high built-in-potential and wide depletion region could be developed between the $CsPbIBr_2$ and c-TiO_2, which enhances dissociation and transfer of photogenerated carriers, while suppressing the electron-hole pair recombination in the cell, respectively. The effect of intermolecular exchange was further

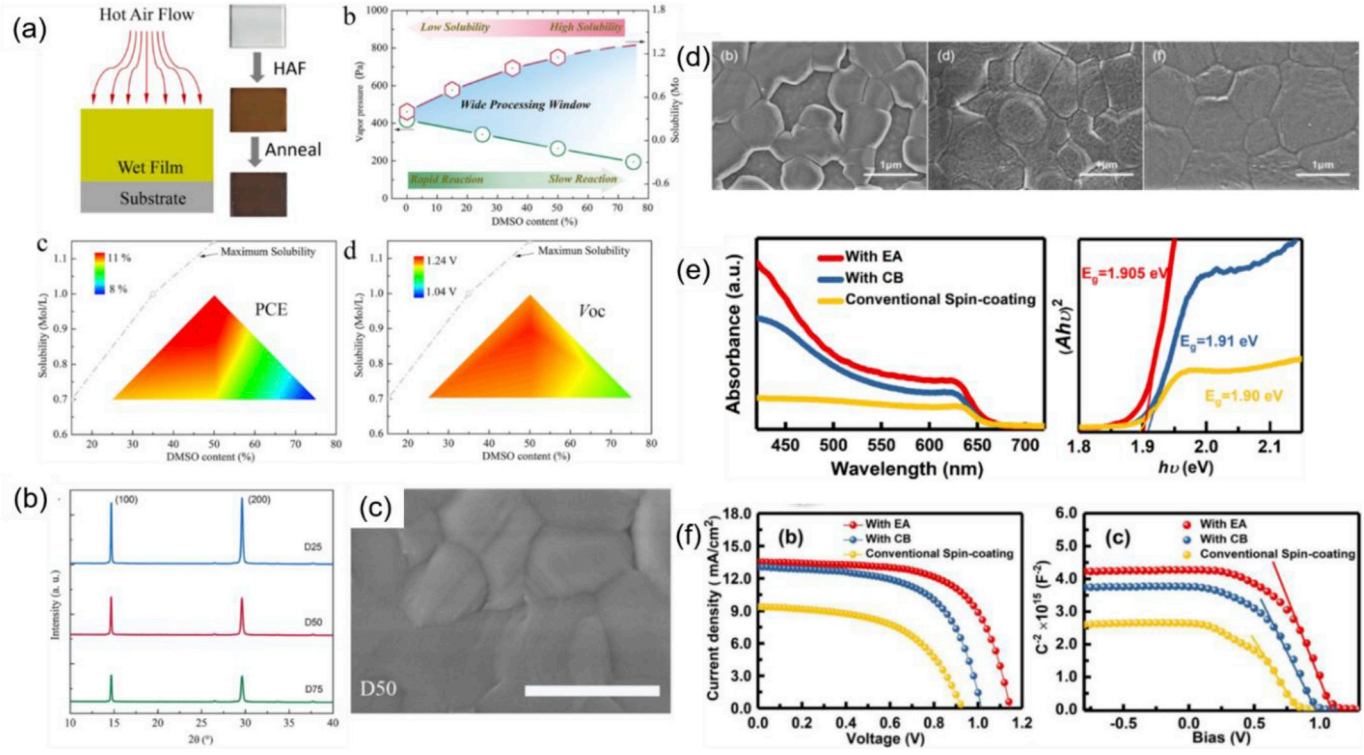

Fig. 24. (a) Schematic of heat-assisted process and photographs of the processed film after HAF and annealing treatments; solubility of the precursor solution as a function of DMSO content; and PCE and V_{oc} curves of the $CsPbI_3$ PSCs as a function of DMSO content. (b) XRD and (c) FESEM images of the $CsPbI_3$ films. Reproduced with permission [112]; copyright 2018, American Chemical Society. (d) SEM images of $CsPbI_2Br$ films obtained using conventional spin-coating process, and chlorobenzene or EA anti-solvent treatment processes, and their corresponding (e) absorption spectra and Tauc plots. (f) J–V curves and Mott-Schottky plots of $CsPbI_2Br$ PSCs. Reproduced with permission [113]; copyright 2018, Wiley-VCH.

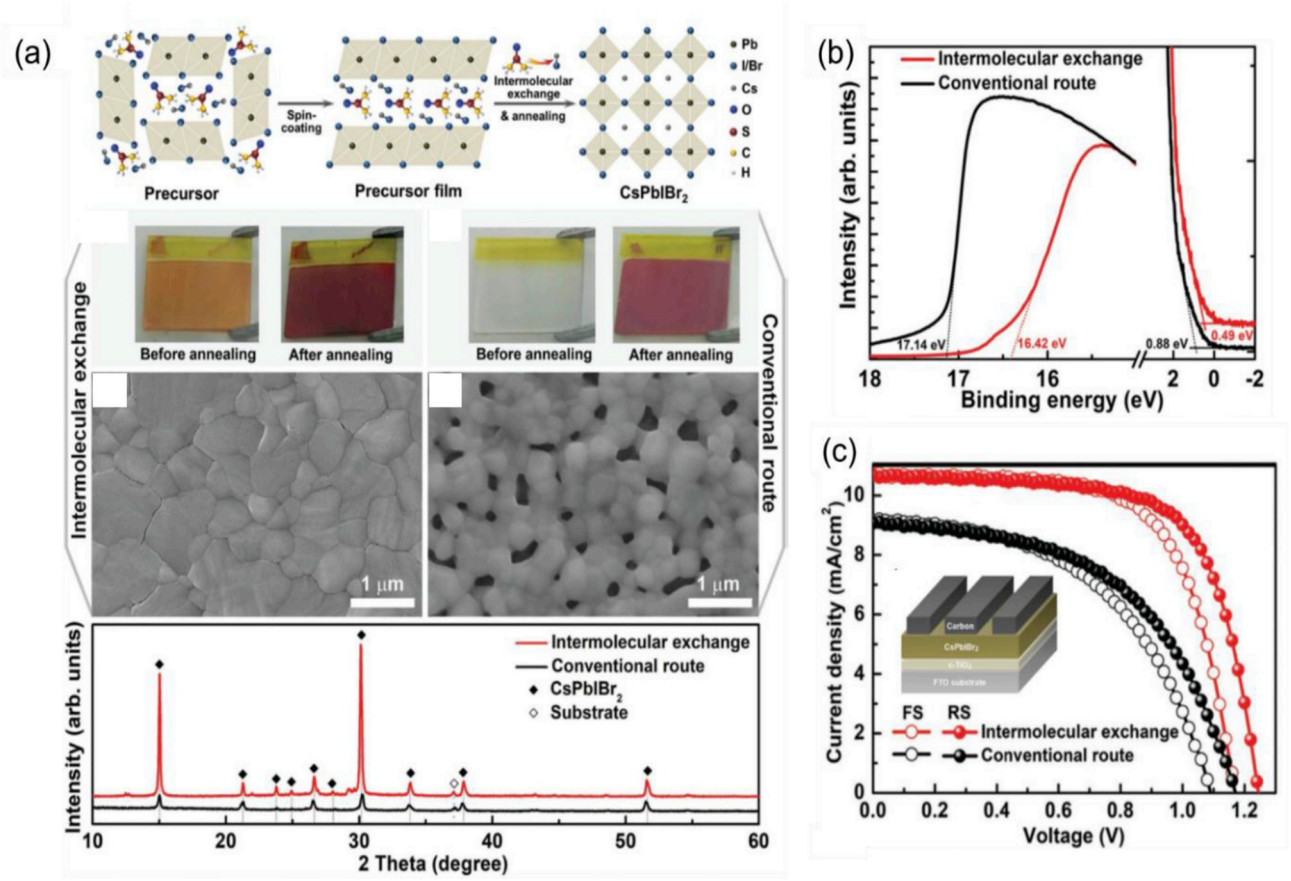

Fig. 25. (a) Schematic of the intermolecular exchange process used to form $CsPbIBr_2$ perovskites; photographs of the $CsPbIBr_2$ films before and after annealing; comparison of SEM images and XRD spectra of the $CsPbIBr_2$ perovskite films obtained by intermolecular exchange and conventional routes. (b) UPS spectra of the $CsPbIBr_2$ films used to calculate the VBM. (c) J–V curves of the $CsPbIBr_2$ PSCs. Reproduced with permission [114]; copyright 2018, Wiley-VCH.

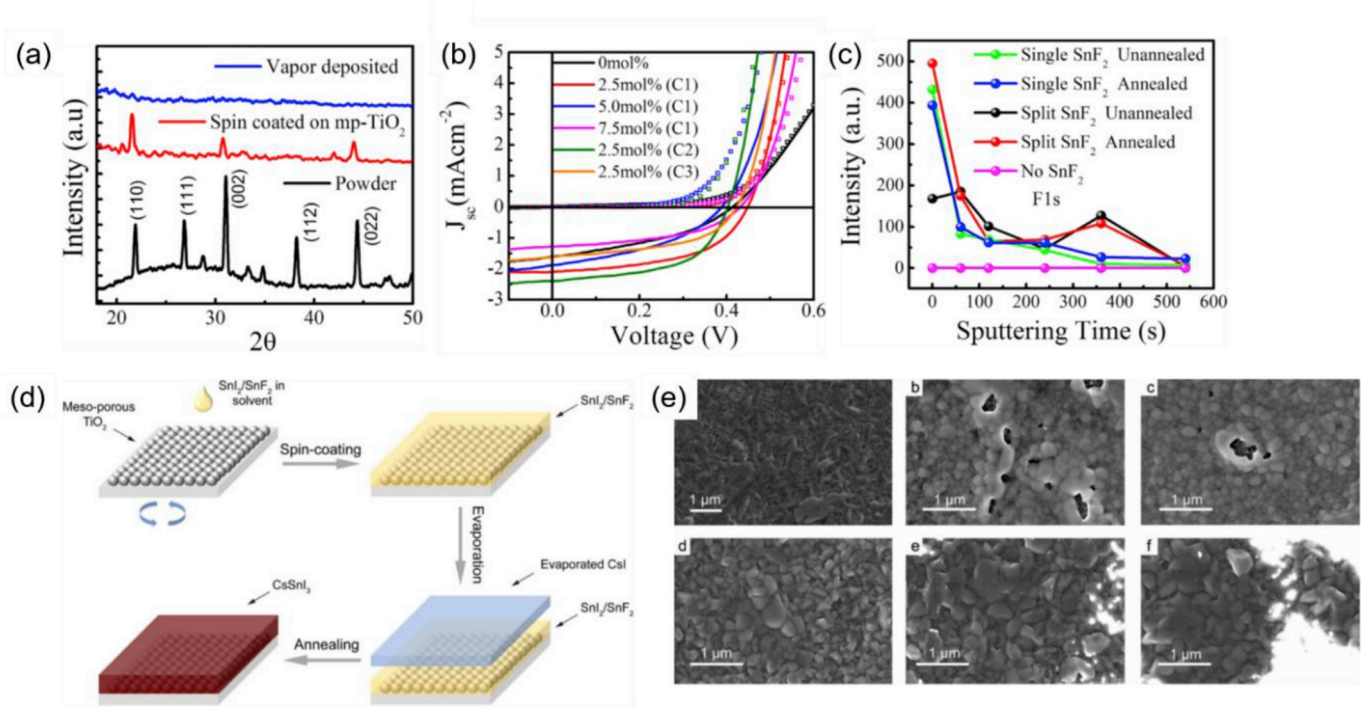

Fig. 26. (a) XRD patterns of the $CsSnBr_3$ perovskite films. (b) J–V curves of the $CsSnBr_3$ PSCs. (c) XPS depth profile of $CsSnBr_3$ perovskite films. Reproduced with permission [115]; copyright 2016, Elsevier. (d) Schematic of the evaporation-assisted solution method for fabricating $CsSnI_3$ films. (e) SEM images of $CsSnI_3$ films with different CsI thickness (0, 40, 52, 66, 80, and 100 nm). Reproduced with permission [116]; copyright 2018, Wiley-VCH.

investigated in terms of the device performance and stability. The HTL-free carbon-electrode-based all-inorganic PSCs with these high-quality $CsPbIBr_2$ films yielded a PCE of 9.16% (Fig. 25c) and excellent long-term stability against both moisture and heat without encapsulation because these devices retained 90% and 97% of their initial PCE over 60 and 7 days when stored in an ambient air (RH: 45%, T: ~25 °C) and in glovebox at temperature of 85 °C, respectively.

In an attempt to fabricate air-stable $CsSnBr_3$ films and devices, Moghe et al. developed a thermal vapor deposition method, where $SnBr_2$ and CsBr thin films were sequentially deposited for immediate reaction [115]. The $CsSnBr_3$ perovskite films obtained using this method showed a stable optical bandgap of 1.8 eV by smoothly varying the molar ratio of CsBr and $SnBr_2$, and optimizing the annealing process. However, no clear diffraction peaks were observed from vapor-deposited $CsPbBr_3$ films, suggesting that they were either amorphous or nanocrystalline (Fig. 26a). Furthermore, doping $CsSnBr_3$ with an optimal concentration of 2.5 mol.% SnF_2 increased the J_{sc} by reducing V_{sn} and trap densities, resulting in a 50% increase in PCE (Fig. 26b). XPS analysis indicated the uniform diffusion of the dopant throughout the film (Fig. 26c). This study demonstrated that thermal vapor deposition is an effective alternate method for doping and depositing lead-free perovskite films.

In traditional solution methods, it is challenging to form smooth pinhole-free $CsSnI_3$ films with high coverage due to the uncontrollable fast crystallization of the Sn-based perovskite. To overcome this problem, Zhu et al. developed an evaporation-assisted solution method (EAS) [116], which combines spin coating the SnI_2+SnF_2 solution and thermal evaporation of CsI onto the coated substrates (Fig. 26d). SEM images showed that the thickness of the thermally evaporated CsI film played a major role in crystal growth; thinner CsI films resulted in the formation of pinholes, while thicker ones produced CsI impurities. The optimal CsI thickness of 66 nm formed smooth pinhole-free $CsSnI_3$ films with large dense grains (Fig. 26e). PSCs with a device structure of FTO/c--TiO_2/mp-TiO_2/$CsSnI_3$/Spiro-OMeTAD/Au showed a PCE of 2.3% for the optimized CsI thickness of 66 nm. This report indicated that the EAS method is suitable for fabricating perovskite films for optoelectronic device applications.

In this section, we thoroughly discussed various deposition methods, including spray-assisted coating, thermal evaporation, intermolecular exchange, anti-solvent treatment, SCG, and vapor-assisted CVD. These methods were demonstrated at the laboratory scale; however, they show promise for industrial-scale fabrication of both $CsPbX_3$-and $CsSnX_3$-based inorganic PSCs. Solution-based spray coating is a simple method for scalable fabrication of high-quality perovskite films under controlled humidity and temperature conditions. Techniques such as thermal evaporation, antisolvent and intermolecular exchange methods are limited by their high cost, limited coating area, and difficulty in controlling the stoichiometry of each precursor, respectively. Otherwise, the thermal evaporation method is highly recommended, as it is a well-established industrial production technology. It is clear from the literature that several efforts have been made to develop and optimize highly efficient and scalable inorganic PSCs, which are expected to be further developed in the near future.

5. Surface and interfacial passivation

Due to the inherent properties of both organic–inorganic hybrid and inorganic perovskites, along with a device architecture consisting of several interfaces, many interfacial defect centers or charge transport barriers can exist at the interfaces and grain boundaries. Specifically, under illumination, the mixed halide perovskites cause phase segregation due to the formation of iodide-rich $CsPbI_{(1+x)}Br_{(2-x)}$ phases at the grain boundaries which generate a high density of mobile ions. These mobile ions accumulate at the interface of carrier transport layer and perovskite and form large injection barriers which hamper the carrier extraction and lead to the formation of strong current density-voltage dependent hysteresis [45]. These defects and the phase segregations are the main cause of hysteresis and instability in the PSCs. To overcome this, several strategies have been developed, including surface and interface passivation [117]. In PSCs, the interfacial defects can be passivated by chemical methods, whereas physical passivation can be used to isolate specific functional layers from the external environment in order to prevent degradation of the device [118]. Therefore, in this section, we summarize recent achievements in the surface and interfacial passivation of $CsPbX_3$-and $CsSnX_3$-based PSCs with improved PCE and stability.

The undesired α-to-δ phase transition in Cs-based inorganic perovskite films has not yet been prevented by solution-chemistry processes. To overcome this unwanted phase transition and obtain a stable $CsPbI_3$ film, Li et al. recently developed a polyvinylpyrrolidone (PVP)-induced surface passivation method [118]. It was hypothesized that the acylamino group of PVP donates lone pairs related to oxygen and nitrogen atoms, which provides a large number of coordination centers. These coordination centers coordinate the polymer molecules on the surface of $CsPbI_3$ with strong N–C bonds and weak C═O bonds. The long backbone chain and electronegative acylamino group of the PVP attract cations of the $CsPbI_3$ precursors. The positive and negative ions of $CsPbI_3$ tend to assemble and bond to form cubic-phase $CsPbI_3$ around the N–C═O coordination of PVP. With increasing reaction time, more $CsPbI_3$ nuclei attach to the PVP, which prevents aggregation of $CsPbI_3$ nanocrystals. With increasing growth rate, $CsPbI_3$ was stabilized with PVP; the surface tension decreases to stabilize the cubic phase of $CsPbI_3$; this occurs even at the microscale due to an enhancement in the electron cloud density on the surface of $CsPbI_3$ originating from the chemical bonding between the acylamino in PVP and $CsPbI_3$ (Fig. 27a). The PVP-induced α-$CsPbI_3$ films exhibited excellent photoelectronic properties, such as extra-long carrier lifetime of 338.7 ns (Fig. 27b), and a high diffusion length >1.5 μm, which was more than ten times higher than that of the orthorhombic phase of $CsPbI_3$. This ultra-long carrier diffusion length indicated that the carrier transport capability of the $CsPbI_3$ films increased, and the carrier recombination due to surface defects was passivated by the PVP. It should be noted that all of the PVP-induced $CsPbI_3$ were treated with IPA to remove residual PVP, which acts as an insulator. Based on these excellent electrical properties, the fabricated $CsPbI_3$ PSCs without encapsulation showed a PCE of 10.74% (Fig. 27c) and good moisture (R. H. 45–55%, RT) and thermal stability (60 °C, N_2 atmosphere) over three months. Without removing the residual PVP, the PCE of the PSC was only 4.7 %. The improved $CsPbI_3$ phase stability achieved with the addition of PVP demonstrated significant progress towards the fabrication of efficient and highly stable PSCs on a large scale.

Recently, Wang et al. developed a simple post-treatment method of $CsPbI_3$ films with phenyltrimethylammonium bromide (PTABr) solution to improve the phase instability under high humidity [25]. The PTABr-$CsPbI_3$ perovskite film exhibited a dense and pinhole-free surface morphology with large grains (average grain size of 510 nm). The EDS results revealed that the PTABr treatment resulted in a gradient of Br doping in the $CsPbI_3$ perovskite film, which formed a PTABr-$CsPbI_3$ film with a Br-rich perovskite surface. Furthermore, the PTA^+ organic cations were terminated on the $CsPbI_3$ perovskite surface. Based on these findings, this report suggested that graded Br doping enhanced crystal growth and phase stability, while the organic PTA^+ cations passivated the $CsPbI_3$ perovskite surface (Fig. 27d), which enhanced the carrier lifetime and carrier transport, while reducing the contact resistance of the device (Fig. 27e). The PSCs fabricated with this PTABr-treated $CsPbI_3$ film exhibited a PCE of 17.06%, V_{oc} of 1.104V, J_{sc} of 18.76 mA/cm^2, and FF of 80.6% (Fig. 27f). The high V_{oc} and FF were attributed to the Br doping and surface passivation by the PTA^+ cations. Furthermore, the PTABr-treated $CsPbI_3$ inorganic PSCs retained 91% of their initial PCE after stored in nitrogen filled glovebox for 500 h indicating showed high photostability and moisture stability due to the high moisture resistance of PTA. Similarly, as discussed in Section 2, additives such as $EDAPbI_4$, zwitterions, Sr, Bi, and Ca also acted as surface passivation layers for the $CsPbX_3$ inorganic PSCs, which significantly

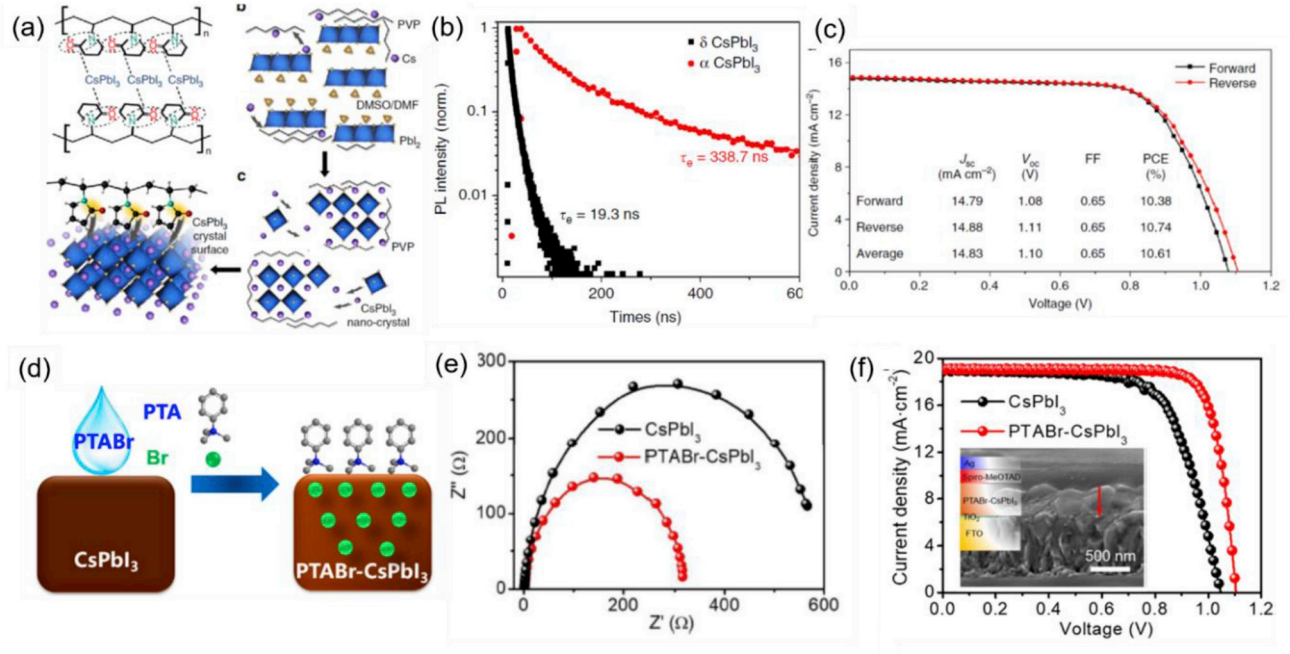

Fig. 27. (a) Schematic of the mechanism of PVP-induced phase stability of $CsPbI_3$ perovskites. (b) TRPL spectra of PVP-induced $CsPbI_3$ perovskite film. (c) J–V curve and device stability of the $CsPbI_3$ PSCs. Reproduced with permission [118]; copyright 2018, Nature Publishing Group. **(d)** Schematic diagram of gradient doping and surface passivation of $CsPbI_3$ films by PTA organic cations. (e) Nyquist plot, and (f) J–V curves of $CsPbI_3$ and PTABr-$CsPbI_3$ PSCs. Reproduced with permission [25]; copyright 2018, American Chemical Society.

improved the device performance and thermodynamic stability [65,67,70,71,81].

The electron-hole carrier recombination due to the presence of surface defect states in PSCs results in energy losses (E_{loss}) which degrade device performance. Zeng et al. reported the electronic passivation of these surface defect states in $CsPbI_2Br$ films by P3HT polymer [119]. In this report, spin coating of $CsPbI_2Br$ nanocrystals was used to fabricate the perovskite film, followed by a ligand removal process by soaking in $Pb(OAc)_2$ IPA solution; next, a Li-doped P3HT HTL was spin coated on the $CsPbI_2Br$ film, then annealed at 200 °C for 5 min. A Stokes shift in the PL spectra of the Pb-rich $CsPbI_2Br$ film showed the presence of surface defects. The P3HT coating on the top of the $CsPbI_2Br$ film effectively passivated surface defects, as well as the interface between $CsPbI_2Br$ and P3HT; this was confirmed by the quenching of PL peaks and increased

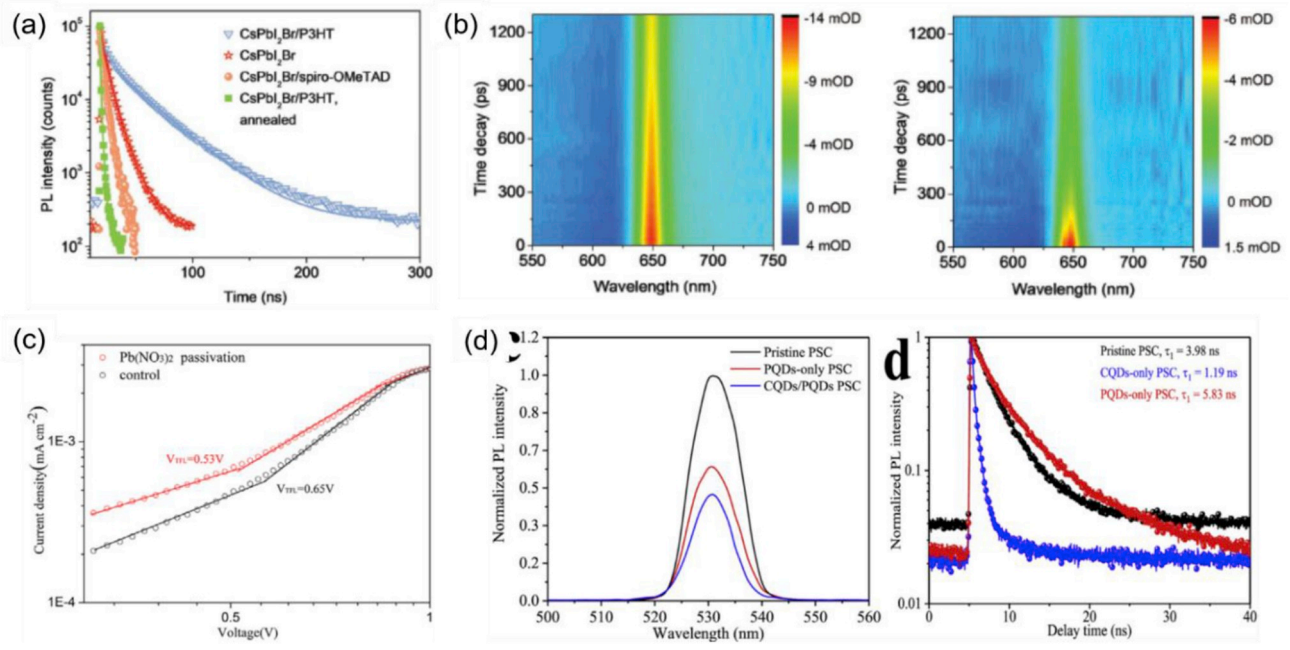

Fig. 28. (a) TRPL spectra of $CsPbI_2Br$ perovskite film with P3HT layer. (b) Transient absorption spectral maps of $CsPbI_2Br$/P3HT bilayers before and after annealing. Reproduced with permission [119]; copyright 2018, Wiley-VCH. (c) dark J–V curves of the electron-only devices showing VTFL points for the non-passivated and Pb^{2+}-passivated $CsPbI_2Br$ PSCs. Reproduced with permission [120]; copyright 2018, Wiley-VCH. (d) Steady PL spectra and TRPL decay of the $CsPbBr_3$ perovskite films with and without interfacial modifications using PQD and/or CQD. Reproduced with permission [60]; copyright 2018, Elsevier.

carrier lifetime (from 6.91 to 14.8 nm) observed from TRPL measurements (Fig. 28a). The plausible mechanism suggested that the sulfur atoms in P3HT played a major role in the surface and interfacial passivation of $CsPbI_2Br$ perovskite film. The S atom first bound to the Cs atoms on the $CsPbI_2Br$ (110) surface and passivated the positively charged under-coordinated Cs^+ ions at the interface. Similarly, the S atoms further bonded to Pb atoms and passivated antisite defects (known as deep-level defects). Furthermore, P3HT efficiently passivated both the surface and interface of the $CsPbI_2Br$ films, which significantly reduced the number of trap states. The TRPL decay of the $CsPbI_2Br$/P3HT films reduced from over 1300 to around 400 ps after annealing at 200 °C, indicating that P3HT enhanced hole extraction and transport in the devices due to the improved band alignments (Fig. 28c). These P3HT-passivated PSCs exhibited a PCE of 12.02%, with a high V_{oc} of 1.32 V and low E_{loss} of 0.5 eV. Similarly, organic hole transport materials, including BT-BTH ([2-(3,5-bis(5-(5-hexylthiophen-2-yl)thiophen-2-yl)thiophen-2-yl)-3,5-bis(5-(5-hexylthiophen-2-yl)thiophen-2-yl)thiophene]), PEDOT, PANi, and PPy have been used as HTLs in $CsPbBr_3$-based inorganic PSCs [121]. Among these small organic HTLs, the use of BT-BTH significantly reduced the carrier recombination at the $CsPbBr_3$/BT-BTH interface due to the low energy level difference which enhanced hole extraction and improved device performance. The $CsPbBr_3$ inorganic PSCs fabricated with BT-BTH HTL exhibited a PCE of 9.32% and improved stability (maintained 94% of the initial PCE) under high R.H. of 70% over 80 d without encapsulation.

It has been reported that two types of defects, namely Pb vacancies (V_{Pb}) and I interstitials (I_i), can easily form on the surface of perovskite films due to their low formation energy [122,123]. These defects in $CsPbX_3$ films form deep trap states at the surface that lead to severe charge recombination. Yuan et al. presented a Pb^+ solution post-processing strategy to passivate these deep trap states at the surface of the $CsPbI_2Br$ film [120]. The Pb^{2+} ions from the $Pb(NO_3)_2$ methyl acetate solution effectively combined with excess halide ions on the perovskite surface to reduce the density of deep trap states of V_{Pb} and I_i, which enhanced the carrier lifetime and effectively reduced the trap densities from 8×10^{16} to 6.64×10^{16} (Fig. 28c). PSCs prepared with $CsPbI_2Br$ films treated with Pb^+ ions showed a PCE of 12.34% with a high V_{oc} of 1.29 V.

A critical disadvantage of interfacial defects is that the PSCs suffer from severe charge carrier recombination and efficiency loss; therefore, such defects need to be passivated by interface passivation or interfacial engineering strategies. Since the energy difference at the $TiO_2/CsPbBr_3$ interface is 0.9 eV and $CsPbBr_3$/carbon interface is 0.6 eV, severe charge carrier recombination can occur at these interfaces. To minimize these losses, Yuan et al. fabricated all-inorganic $CsPbBr_3$ PSCs by modifying the $TiO_2/CsPbBr_3$ and $CsPbBr_3$/carbon interfaces with carbon QDs (CQDs) and phosphorous QDs (PQDs), respectively. Both QD systems introduced intermediate energy levels at the respective interfaces, which suppressed charge recombination (Fig. 28d) and resulted in a high V_{oc} of 1.45 V, J_{sc} of 7.24 mA/cm^2, and PCE of 7.93% with excellent long-term stability (99% of initial PCE at R.H. of 80%, RT 25 °C) over 1400 h without encapsulation [60]. A similar approach was demonstrated by Ding et al. [124] to reduce recombination at the interfaces of $TiO_2/CsPbBr_3$ and $CsPbBr_3$/carbon by introducing intermediate energy levels using graphene QDs (GQDs), PQDs, and $CInS_2/ZnS$ alloy QDs (CISZ-QDs). These QDs also effectively suppressed interfacial recombination and enhanced device performance and stability [59,61,124].

To reduce the interfacial trap density, Liu et al. inserted an ultra-thin (4 nm) MoO_x cathode buffer layer at the interface between $CsPbIBr_2$ and the electrode [125]. They have annealed the thermal deposited MoO_x (thickness = 4 nm) film by in nitrogen ambient at 160 °C for 10 min which increased the oxygen vacancy and lowered the work function of MoO_x to 4.30 eV. In this case the MoO_x thin film worked as an ETL for the $CsPbIBr_2$ PSCs because it has been found that the conduction band discontinuity (ΔE_{CB}) between the $CsPbIBr_2$ and MoO_x is < 0.1 eV and valence band discontinuity (ΔE_{VB}) 1.8 eV. The low work function of the n-type MoO_x resulted in reducing the energy barrier from the CB of $CsPbIBr_2$, as the surface energy bands bend downwards and significantly facilitated the extraction of electrons. The thin (4 nm) MoO_x layer not only enhanced the J_{sc} of the $CsPbIBr_2$ inorganic PSCs by enhancing the electron extraction but also increased the built-in potential which further enhanced the V_{oc}. In this report the authors have presented that if the thickness of the MoO_x film increased the work function and bulk resistance would increase which could hinder the electron transportation and the device performance. The low WF of the MoO_x cathode buffer layer significantly reduced the Schottky barrier, contact resistance, and interfacial recombination (Fig. 29a-c), which improved the device performance. Moreover, the unencapsulated devices also maintained 100% and 88% of their initial PCE for 150 d in a nitrogen ambient and thermal stability at 85 °C for 90 min in air ambient, respectively.

The same group further fabricated $CsPbI_2Br$-based all-inorganic PSCs using a ZnO@C_{60} bi-layer ETL [126]. The driving force (ΔG), defined as the difference between the conduction band minimum of the perovskite and the ETL, was 0.04 eV and 0.32 eV for the ZnO and C_{60} ETLs, respectively, indicating that the C_{60} ETL could extract more electrons than the ZnO ETL (Fig. 29d). A C_{60} coating on the ZnO layer passivated the ZnO pinholes, while reducing interfacial recombination (Fig. 29e), which consequently increased the multiple pathways for electron extraction. The $CsPbI_2Br$-based all-inorganic PSCs fabricated with this bilayer ZnO@C_{60} ETL exhibited a high PCE of 13.3% and were thermodynamically stable (Fig. 29f). Similarly, many efforts, such as increasing the film thickness [127], introducing PbO [128], and polyethylene glycol (PEG) [129], have been made by several research groups to reduce the bulk and surface recombination of $CsPbIBr_2$ based inorganic PSCs, respectively. However, very few efforts have been made to passivate $CsSnX_3$-based lead-free inorganic perovskites, apart from the addition of, e.g., SnF_2, $SnCl_2$, and SnI_2, which significantly reduced the surface and bulk recombination, as discussed in Section 2.

6. Conclusions and outlooks

We have reviewed the recent progress in $CsPbX_3$ and Pb-free $CsSnX_3$ inorganic perovskite-based solar cells, which have shown promising optoelectrical and thermodynamic properties. The PCE values from the studies discussed here are compared in Table 1. First, we discussed various compositional modifications used in the development of lead-based and lead-free inorganic PSCs. In the early stage of development, lead-based inorganic PSCs exhibited low device performance due to the phase instability of $CsPbI_3$ and wide bandgap of $CsPbBr_3$ films. Therefore, numerous studies have developed mixed-halide ($CsPbI_{3-x}Br_x$) materials to stabilize the perovskite film, which achieved efficiencies over 10%. Similarly, various additives were used to stabilize the cubic phase of $CsPbI_3$, which effectively produced high-quality stable $CsPbI_3$ films, even at a low temperature of 100 °C in an ambient atmosphere. PTABr-treated $CsPbI_3$ inorganic PSCs showed the highest efficiency of 17.06% among all inorganic-based PSCs. Furthermore, the partial replacement of Pb with Bi, Sr, Sn, Ca, Sm, and lanthanide metals significantly enhanced both device performance and structural stability. Several approaches have been demonstrated for stabilizing the $CsSnX_3$-based perovskites in PSCs. Most commonly, Sn halide precursors have been added to improve the structural stability and device performance. In particular, optimal $CsSnI_3$ films were formed using excess SnI_2 addition under an N_2H_4 atmosphere, resulting in a device with the highest PCE of 4.8%.

Second, several solvent engineering and deposition methods have been discussed. Solution methods with RT drying and PTABr treatment of the inorganic perovskite films showed promising phase stability and device performance. However, spray-coating and thermal co-evaporation methods are thought to be the optimal for fabricating perovskite films, as they can overcome the solubility limits of perovskite precursors and provide a feasible benchmark for large-scale fabrication. However, only a few methods, including the conventional solution,

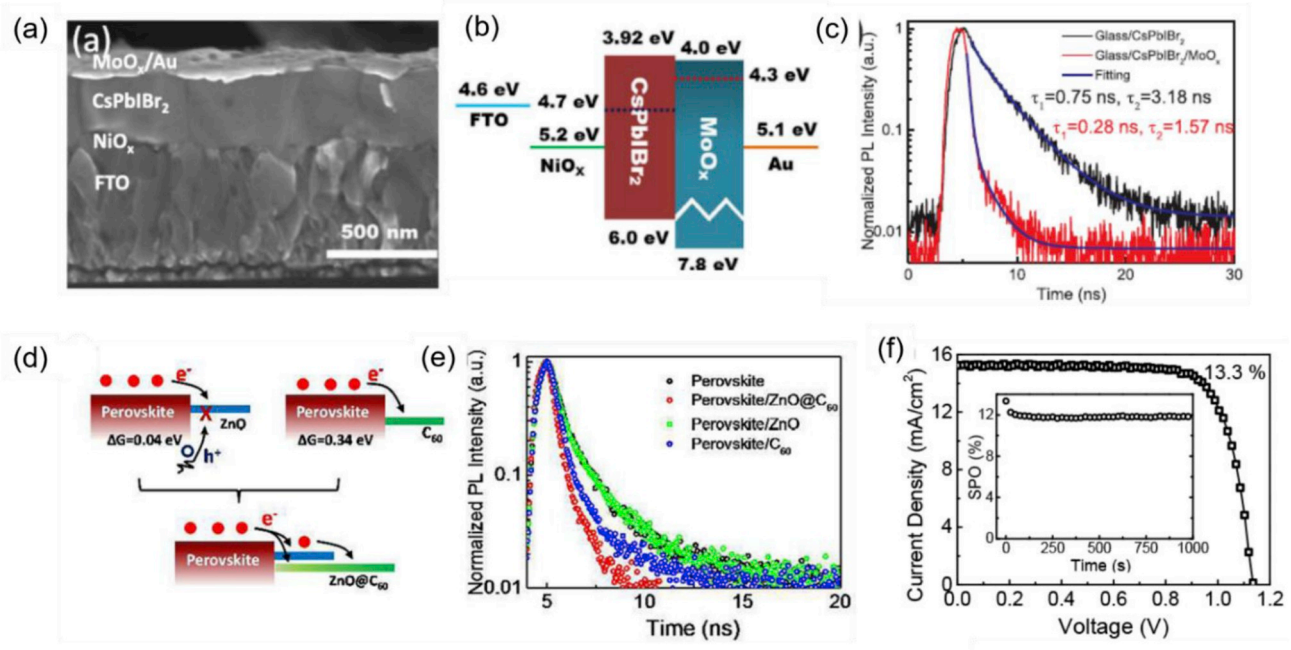

Fig. 29. (a) Cross-sectional FESEM image of the $CsPbIBr_2$ PSC, (b) energy band diagram, and (c) TRPL decay curves of complete devices. Reproduced with permission [125]; copyright 2017, Elsevier. (d) Schematic of the bandgap alignment of ZnO and C_{60} ETLs, (e) TRPL spectra of $CsPbI_2Br$ films with different ETLs, and (f) J–V curve and stabilized PCE of $CsPbI_2Br$ PSCs. Reproduced with permission [126]; copyright 2018, American Chemical Society.

thermal evaporation, and EAS methods have been developed for $CsSnX_3$ film fabrication. Finally, methods for passivating surface and interfacial traps were discussed, as such traps cause severe carrier recombination and inhibit device performance. In general, the use of additives in the perovskite precursors and the polymer/organic carrier transport layers is very effective for passivating both surface and interface traps. In addition, QDs are beneficial for interfacial passivation by forming intermediate levels between the carrier transport layer and perovskite film, which reduces recombination at the interfaces and improves extraction of charge carriers.

Although these impressive developments have been achieved in a very short time, the stability and device performance of inorganic-based PSCs remain inferior to those of organic–inorganic hybrid PSCs and require further improvement. Since inorganic perovskites are insensitive to light-induced ion migration, their photostability is higher than that of organic–inorganic hybrid perovskites. However, inorganic perovskites still have low stability due to the α-to-δ phase change related to the low *t*-factor of Cs in $CsPbI_3$ in the ambient atmosphere, which is a major impediment to their commercialization. These stability problems may be carefully investigated and resolved by replacing the A-site alkali cation (Cs) with super alkali cations like Li_3O, LiF_2 and H_5O_2 [9–11]. The reduction of grain sizes (< 100 nm) makes the inorganic perovskites thermodynamically stable, however, their device performance is not that much comparable to that of devices made with large grains because these nanostructured perovskite possess severe surface recombination issues [130]. Therefore, effective phase stabilization methods producing larger grains with low surface recombination could be developed to further improve the PCE of the inorganic PSCs. Similarly, the favorable oxidization of Sn^{2+} to Sn^{+4} ions in $CsSnI_3$ results in the formation of SnO_2 and V_{Sn} in air, which hinders device performance. Therefore, to produce viable $CsSnI_3$ PSCs, further methods should be developed, or the devices should be carefully encapsulated. The PCE of inorganic PSCs is still below that of organic–inorganic PSCs, although various additive and doping strategies were used to significantly stabilize the cubic phases of inorganic PSCs and increase the PCE. Further efforts are required to deposit high-quality perovskite films to enhance device performance. The lead-based inorganic PSCs have achieved remarkable PCE improvement as compared to the lead-free inorganic PSCs. However, the inherent toxicity of lead is a major concern for environment and human health. Therefore, lead-free high-quality inorganic perovskites should be developed for the fabrication of lead-free inorganic PSCs.

The highest PCE of 17.06 % was obtained from an inorganic PSC with using Spiro-OMeTAD as an organic HTL. In addition, most of the literature report the use of Spiro-OMeTAD as an HTM in the inorganic PSCs. However, Spiro-OMeTAD suffers from thermal stress and hinders the device performance and stability of the PSCs due to its low glass transition temperature (125 °C) [131]. Therefore, further research is required to develop organic HTLs with high glass transition temperature, low HOMO energy level and high carrier mobility in order to improve the device stability, carrier transportation and boost the device performance. Furthermore, inorganic HTLs including carbon or C_{60} electrodes showed low PCE values compared to organic HTLs due to the large energy barrier between the perovskite and HTL, which increases charge carrier recombination. In this scenario, inorganic HTLs such as NiO [132], Li-Mg-NiO [133], Cu-NiO [134], CuSCN [135], and CuI [70] and ETLs including, SnO_2 [136], ZnO, [27], Al-ZnO [137] and In_2S_3 [138] are better choices over organic HTLs, ETLs, and inorganic carbon base transport layers because of their excellent moisture and thermal stability. In addition, these inorganic metal oxides are capable of producing more compact film than the organic molecules and perfectly matching band alignment with the perovskite for significant carrier transportation which can reduce the carrier recombination and enhance the PCE of the PSCs. Therefore, more research efforts should be drawn towards the fabrication of all inorganic perovskite solar cells by employing these inorganic metal oxides instead of the above organic charge transport layers. Though thermal annealing temperatures for preparing the metal oxides are relatively high compared with those for organic charge transport materials, constructing whole device would be more feasible as underlying inorganic perovskites are much thermally stable than organic-inorganic hybrid perovskites.

Solvent engineering, compositional modifications, new deposition methods, and surface/interface passivation techniques are gradually overcoming the structural instability in ambient conditions, phase

Table 1
Summary of the device performance of reported $CsPbX_3$-and $CsSnX_3$-based PSCs.

Composition	Additives	Device structure	J_{sc} (mA/cm^2)	V_{oc} (V)	FF (%)	PCE (%)	Ref.
$CsPbI_3$		FTO/TiO_2/$CsPbI_3$/Spiro-OMeTAD/Au	12.00	0.800	-	2.90	[23]
$CsPbI_3$	PTABr	FTO/TiO_2/PTABr-$CsPbI_3$/Spiro-OMeTAD/Ag	19.15	1.104	80.6	17.06	[25]
$CsPbI_3$ QDs		FTO/TiO_2/$CsPbI_3$/Spiro-OMeTAD/MoO_x/Au	13.47	1.23	65.0	10.77	[63]
$CsPbI_3$ QDs		FTO/TiO_2/$CsPbI_3$/Spiro-OMeTAD/MoO_x/Al	15.24	1.162	76.6	13.43	[64]
$CsPbI_3$	Zwitteri-ons	ITO/PTAA/$CsPbI_3$/PCBM/C_{60}/BCP	14.9	1.08	70	11.4	[65]
$CsPbI_3$	$EDAPbI_4$	FTO/TiO_2/$CsPbI_3$/Spiro-OMeTAD/Ag	14.53	1.15	71.0	11.86	[67]
$CsPbI_3$	PEAI	FTO/TiO_2/$CsPbI_3$/Spiro-OMeTAD/Ag	18.1	1.11	69.6	14.3	[68]
$CsPbI_3$	$HPbI_3$	FTO/TiO_2/$CsPbI_3$/carbon	18.5	0.79	65	9.5	[69]
$CsPbI_3$	BiI_3	FTO/TiO_2/$CsPbI_3$/CuI/Au	18.76	0.97	72.59	13.21	[70]
$CsPbI_3$	CaI_2	FTO/TiO_2/$CsPbI_3$/P3HT/Au	17.9	0.945	80.0	13.5	[71]
$CsPbI_3$	H_2O	FTO/TiO_2/$CsPbI_3$/P3HT/Au	16.53	1.04	65.7	11.3	[73]
$CsPbI_3$		ITO/SnO_2/$CsPbI_3$/Spiro-OMeTAD/Au	18.41	1.08	79.32	15.7	[106]
$CsPbI_3$		FTO/TiO_2/$CsPbI_3$/P3HT/Al	13.8	1.063	71.6	10.5	[109]
$CsPbI_3$	PVP	FTO/TiO_2/$CsPbI_3$/Spiro-OMeTAD/Au	14.88	1.11	65	10.74	[118]
$CsPbBr_3$		FTO/TiO_2/$CsPbBr_3$ /PTAA/Au	6.24	1.280	74.0	5.95	[22]
$CsPbBr_3$		FTO/TiO_2/$CsPbBr_3$ /PTAA/Au	6.70	1.250	74.0	6.60	[51]
$CsPbBr_3$		FTO/TiO_2/$CsPbBr_3$ /Carbon	5.70	1.290	68.0	5.00	[53]
$CsPbBr_3$		FTO/TiO_2/$CsPbBr_3$ /Carbon	7.40	1.240	73.0	6.70	[52]
$CsPbBr_3$		FTO/TiO_2/$CsPbBr_3$/Spiro-OMeTAD/Au	5.6	1.5	62.0	5.40	[54]
$CsPbBr_3$	$PbCl_2$	FTO/TiO_2/$CsPbBr_3$(Cl)/Spiro-OMeTAD/Ag	8.47	1.02	71.6	6.21	[58]
$CsPbBr_3$		FTO/TiO_2/$CsPbBr_3$ /Carbon	7.35	1.522	84.3	9.43	[59]
$CsPbBr_3$	Ln^+	FTO/TiO_2/$CsPb_{0.97}Sm_{0.03}Br_3$/Carbon	7.48	1.594	85.1	10.14	[62]
$CsPbBr_3$		FTO/TiO_2/$CsPbBr_3$ /Carbon	8.12	1.458	82.1	9.72	[101]
$CsPbBr_3$	Py	FTO/TiO_2/$CsPbBr_3$/Spiro-OMeTAD/Au	6.52	1.340	69	6.05	[103]
$CsPbBr_3$		ITO/SnO_2/$CsPbBr_3$/Spiro-OMeTAD/Au	10.33	1.26	75.34	9.81	[106]
$CsPbI_2Br$		ITO/NiO_x/$CsPbI_2Br$/C_{60}/BCP/Ag	12.6	1.05	78.7	10.4	[77]
$CsPbI_2Br$		ITO/Ca/C60/$CsPbI_2Br$/TAPC/TAPC:MoO_3/Ag	15.2	1.15	67.0	11.8	[78]
$CsPbI_2Br$		FTO/TiO_2/$CsPbI_2Br$/Spiro-OMeTAD/Au	12.0	1.23	73.0	10.7	[79]
$CsPbI_2Br$	KI	FTO/TiO_2/$CsPbI_2Br$/Spiro-OMeTAD/Au	11.6	1.18	73.0	10	[80]
$CsPbI_2Br$	SrI_2	FTO/TiO_2/$CsPbI_2Br$/P3HT/Au	15.3	1.043	69.9	11.2	[81]
$CsPbI_2Br$		ITO/SnO_2/$CsPbI_2Br$/Spiro-OMeTAD/Au	17.13	1.22	77.52	16.14	[106]
$CsPbI_2Br$		FTO/TiO_2/$CsPbI_2Br$/Spiro-OMeTAD/Ag	13.56	1.315	74.3	12.52	[112]
$CsPbI_2Br$		FTO/TiO_2/$CsPbI_2Br$/Carbon	13.54	1.15	64.2	10.0	[113]
$CsPbI_2Br$		FTO/TiO_2/$CsPbI_2Br$/P3HT/Au	13.13	1.32	70.04	12.02	[119]
$CsPbI_2Br$	$Pb(NO_3)_2$	ITO/SnO_2/$CsPbI_2Br$/Spiro-OMeTAD/Ag	1.29	12.41	76.9	12.34	[120]
$CsPbIBr_2$		FTO/TiO_2/$CsPbIBr_2$/Au	8.7	0.959	56	4.7	[82]
$CsPbIBr_2$	Sn	FTO/TiO_2/$CsPbIBr_2$ /Carbon	14.30	1.26	63.0	11.33	[84]
$CsSnI_3$	SnF_2	FTO/TiO_2/$CsSnI_3$/HTL/Au	22.70	0.24	37.0	2.02	[92]
$CsSnI_3$		ITO/NiO_x/$CsSnI_3$/PCBM/Al	10.21	0.52	62.5	3.31	[94]
$CsSnI_3$	$SnCl_2$	ITO/$CsSnI_3$/PCBM/BCP/Al	9.89	0.50	68.0	3.56	[95]
$CsSnI_3$		FTO/TiO_2/$CsSnI_3$/PTAA/Au	25.71	0.381	49.05	4.81	[98]
$CsSnI_3$		FTO/TiO_2/$CsSnI_3$/Spiro-OMeTAD/Au	17.10	0.276	47.15	2.3	[116]
$CsSnBr_3$	SnF_2	FTO/TiO_2/$CsSnBr_3$/Spiro-OMeTAD/Au	9.1	0.42	57.0	2.17	[96]
$CsSnBr_3$	N_2H_4	FTO/TiO_2/$CsSnBr_3$/PTAA/Au	13.96	0.366	59.36	3.04	[97]
$CsSnI_2Br$	SnF_2	FTO/TiO_2/$CsSnI_2Br$/Spiro-OMeTAD/Au	15.06	0.289	38.0	1.67	[99]
$CsSnIBr_2$	HPA	FTO/TiO_2/Al_2O_3/$CsSnIBr_2$/Carbon	17.4	0.31	57	3.2	[100]

instability, and carrier recombination in perovskite materials. Facile solution-based and vacuum deposition methods were successfully demonstrated for the fabrication of both $CsPbX_3$ and $CsSnX_3$ inorganic perovskite film. Finally, surface and interface recombination has been suppressed using QDs, inorganic metal oxide nanoparticles, and polymer carrier transport layers. Apart from these developments, the high V_{oc} (due to the wide bandgap of inorganic perovskites) and the outstanding photo- and thermal stability of inorganic-based PSCs makes them beneficial for the fabrication of tandem solar cells or other energy conversion cells. The large open circuit voltages of the halide perovskite solar cells make them the potential candidates as the photovoltaic components of the photoelectrochemical devices [139–141]. Because, the single semiconductor photoelectrode, such as silicon, thin film chalcogenides, in photoelectrochemical devices like water splitting and solar redox flow batteries cannot generate enough photovoltage to drive the chemical reactions due to the thermodynamic and recombination losses associated with the insufficient redox potential of 1.23 V. Thus, additional voltage (0.4–0.6 eV) is required to overcome these thermodynamic and recombination losses for the photoelectrochemical devices as previously reported by Hu et al. and Bae et al. [142,143] Therefore, these perovskite light absorbers can be integrated onto other photoelectrodes of the photoelectrochemical systems to harvest significant portion of the solar spectrum and generate enough photovoltage to overcome the overpotential and thermodynamic potential for water splitting and solar redox flow batteries.

Declaration of competing interest

There are no conflicts of interest to declare.

Acknowledgements

This work was supported by the National Research Foundation of Korea (Korea Government) [grant numbers NRF- 2018R1C1B6008028 and NRF- 2018R1A4A1024691].

References

[1] M.A. Green, Y. Hishikawa, E.D. Dunlop, D.H. Levi, J. Hohl-Ebinger, M. Yoshita, A. W.Y. Ho-Baillie, Solar cell efficiency tables (Version 53), Prog. Photovolt. Res. Appl. 27 (2019) 3–12.
[2] S.D. Stranks, G.E. Eperon, G. Grancini, C. Menelaou, M.J.P. Alcocer, T. Leijtens, L. M. Herz, A. Petrozza, H.J. Snaith, Electron-hole diffusion lengths exceeding 1 micrometer in an organometal trihalide perovskite absorber, Science 342 (2013) 341.
[3] Q. Dong, Y. Fang, Y. Shao, P. Mulligan, J. Qiu, L. Cao, J. Huang, Electron-hole diffusion lengths > 175 μm in solution-grown $CH_3NH_3PbI_3$ single crystals, Science 347 (2015) 967.

[4] J.H. Noh, S.H. Im, J.H. Heo, T.N. Mandal, S.I. Seok, Chemical management for colorful, efficient, and stable inorganic–organic hybrid nanostructured solar cells, Nano Lett. 13 (2013) 1764–1769.

[5] S. De Wolf, J. Holovsky, S.-J. Moon, P. Löper, B. Niesen, M. Ledinsky, F.-J. Haug, J.-H. Yum, C. Ballif, Organometallic halide perovskites: sharp optical absorption edge and its relation to photovoltaic performance, J. Phys. Chem. Lett. 5 (2014) 1035–1039.

[6] A. Kojima, K. Teshima, Y. Shirai, T. Miyasaka, Organometal halide perovskites as visible-light sensitizers for photovoltaic cells, J. Am. Chem. Soc. 131 (2009) 6050–6051.

[7] NREL, in: B.R.-C.E. Chart (Ed.), Best Research-Cell Efficiency Chart, 2019.

[8] M. Wang, Z. Zang, B. Yang, X. Hu, K. Sun, L. Sun, Performance improvement of perovskite solar cells through enhanced hole extraction: the role of iodide concentration gradient, Sol. Energy Mater. Sol. Cells 185 (2018) 117–123.

[9] T. Zhou, M. Wang, Z. Zang, L. Fang, Stable dynamics performance and high efficiency of ABX3-type super-alkali perovskites first obtained by introducing H5O2 cation, Adv. Energy Mater. 9 (2019) 1900664.

[10] T. Zhou, Y. Zhang, M. Wang, Z. Zang, X. Tang, Tunable electronic structures and high efficiency obtained by introducing superalkali and superhalogen into AMX3-type perovskites, J. Power Sources 429 (2019) 120–126.

[11] T. Zhou, M. Wang, Z. Zang, X. Tang, L. Fang, Two-dimensional lead-free hybrid halide perovskite using superatom anions with tunable electronic properties, Sol. Energy Mater. Sol. Cells 191 (2019) 33–38.

[12] M. Becker, M. Wark, Recent progress in the solution-based sequential deposition of planar perovskite solar cells, Cryst. Growth Des. 18 (2018) 4790–4806.

[13] N.J. Jeon, J.H. Noh, Y.C. Kim, W.S. Yang, S. Ryu, S.I. Seok, Solvent engineering for high-performance inorganic–organic hybrid perovskite solar cells, Nat. Mater. 13 (2014) 897.

[14] H. Wei, X. Zhao, Y. Wei, H. Ma, D. Li, G. Chen, H. Lin, S. Fan, K. Jiang, Flash-evaporation printing methodology for perovskite thin films, NPG Asia Mater. 9 (2017) e395.

[15] J. Ávila, C. Momblona, P.P. Boix, M. Sessolo, H.J. Bolink, Vapor-deposited perovskites: the route to high-performance solar cell production? Joule 1 (2017) 431–442.

[16] Z. Wang, Z. Shi, T. Li, Y. Chen, W. Huang, Stability of perovskite solar cells: a prospective on the substitution of the ACation and XAnion, Angew. Chem. Int. Ed. 56 (2017) 1190–1212.

[17] E. Bi, H. Chen, F. Xie, Y. Wu, W. Chen, Y. Su, A. Islam, M. Grätzel, X. Yang, L. Han, Diffusion engineering of ions and charge carriers for stable efficient perovskite solar cells, Nat. Commun. 8 (2017) 15330.

[18] Q. Fu, X. Tang, B. Huang, T. Hu, L. Tan, L. Chen, Y. Chen, Recent progress on the long-term stability of perovskite solar cells, Adv. Sci. 5 (2018) 1700387.

[19] N.J. Jeon, J.H. Noh, W.S. Yang, Y.C. Kim, S. Ryu, J. Seo, S.I. Seok, Compositional engineering of perovskite materials for high-performance solar cells, Nature 517 (2015) 476.

[20] M. Saliba, T. Matsui, J.-Y. Seo, K. Domanski, J.-P. Correa-Baena, M. K. Nazeeruddin, S.M. Zakeeruddin, W. Tress, A. Abate, A. Hagfeldt, M. Grätzel, Cesium-containing triple cation perovskite solar cells: improved stability, reproducibility and high efficiency, Energy Environ. Sci. 9 (2016) 1989–1997.

[21] J.-W. Lee, D.-H. Kim, H.-S. Kim, S.-W. Seo, S.M. Cho, N.-G. Park, Formamidinium and cesium hybridization for photo- and moisture-stable perovskite solar cell, Adv. Energy Mater. 5 (2015) 1501310.

[22] M. Kulbak, D. Cahen, G. Hodes, How important is the organic part of lead halide perovskite photovoltaic cells? Efficient CsPbBr3 cells, J. Phys. Chem. Lett. 6 (2015) 2452–2456.

[23] G.E. Eperon, G.M. Paternò, R.J. Sutton, A. Zampetti, A.A. Haghighirad, F. Cacialli, H.J. Snaith, Inorganic caesium lead iodide perovskite solar cells, J. Mater. Chem. A 3 (2015) 19688–19695.

[24] C.C. Stoumpos, C.D. Malliakas, M.G. Kanatzidis, Semiconducting tin and lead iodide perovskites with organic cations: phase transitions, high mobilities, and near-infrared photoluminescent properties, Inorg. Chem. 52 (2013) 9019–9038.

[25] Y. Wang, T. Zhang, M. Kan, Y. Zhao, Bifunctional stabilization of all-inorganic α-CsPbI3 perovskite for 17% efficiency photovoltaics, J. Am. Chem. Soc. 140 (2018) 12345–12348.

[26] B.V. Lotsch, New light on an old story: perovskites go solar, Angew. Chem. Int. Ed. 53 (2014) 635–637.

[27] J. You, L. Meng, T.-B. Song, T.-F. Guo, Y. Yang, W.-H. Chang, Z. Hong, H. Chen, H. Zhou, Q. Chen, Y. Liu, N. De Marco, Y. Yang, Improved air stability of perovskite solar cells via solution-processed metal oxide transport layers, Nat. Nanotechnol. 11 (2015) 75.

[28] T. Fujihara, S. Terakawa, T. Matsushima, C. Qin, M. Yahiro, C. Adachi, Fabrication of high coverage MASnI3 perovskite films for stable, planar heterojunction solar cells, J. Mater. Chem. C 5 (2017) 1121–1127.

[29] M.E. Kayesh, T.H. Chowdhury, K. Matsuishi, R. Kaneko, S. Kazaoui, J.-J. Lee, T. Noda, A. Islam, Enhanced photovoltaic performance of FASnI3-based perovskite solar cells with hydrazinium chloride coadditive, ACS Energy Lett. 3 (2018) 1584–1589.

[30] B. Conings, J. Drijkoningen, N. Gauquelin, A. Babayigit, J. D'Haen, L. D'Olieslaeger, A. Ethirajan, J. Verbeeck, J. Manca, E. Mosconi, F.D. Angelis, H.-G. Boyen, Intrinsic thermal instability of methylammonium lead trihalide perovskite, Adv. Energy Mater. 5 (2015) 1500477.

[31] T. Shi, H.-S. Zhang, W. Meng, Q. Teng, M. Liu, X. Yang, Y. Yan, H.-L. Yip, Y.-J. Zhao, Effects of organic cations on the defect physics of tin halide perovskites, J. Mater. Chem. A 5 (2017) 15124–15129.

[32] M.A. Green, A. Ho-Baillie, H.J. Snaith, The emergence of perovskite solar cells, Nat. Photonics 8 (2014) 506.

[33] Q. Tai, F. Yan, Emerging semitransparent solar cells: materials and device design, Adv. Mater. 29 (2017) 1700192.

[34] H. Chen, S. Xiang, W. Li, H. Liu, L. Zhu, S. Yang, Inorganic perovskite solar cells: a rapidly growing field, Solar RRL 2 (2018) 1700188.

[35] C. Xie, P. You, Z. Liu, L. Li, F. Yan, Ultrasensitive broadband phototransistors based on perovskite/organic-semiconductor vertical heterojunctions, Light: Sci. Appl. 6 (2017), e17023.

[36] M. Konstantakou, T. Stergiopoulos, A critical review on tin halide perovskite solar cells, J. Mater. Chem. A 5 (2017) 11518–11549.

[37] B. Parida, A. Singh, M. Oh, M. Jeon, J.-W. Kang, H. Kim, Effect of compact TiO2 layer on structural, optical, and performance characteristics of mesoporous perovskite solar cells, Mater. Today Commun. 18 (2019) 176–183.

[38] H.J. Snaith, A. Abate, J.M. Ball, G.E. Eperon, T. Leijtens, N.K. Noel, S.D. Stranks, J.T.-W. Wang, K. Wojciechowski, W. Zhang, Anomalous hysteresis in perovskite solar cells, J. Phys. Chem. Lett. 5 (2014) 1511–1515.

[39] J. Wei, Y. Zhao, H. Li, G. Li, J. Pan, D. Xu, Q. Zhao, D. Yu, Hysteresis analysis based on the ferroelectric effect in hybrid perovskite solar cells, J. Phys. Chem. Lett. 5 (2014) 3937–3945.

[40] H.-S. Kim, S.K. Kim, B.J. Kim, K.-S. Shin, M.K. Gupta, H.S. Jung, S.-W. Kim, N.-G. Park, Ferroelectric polarization in CH3NH3PbI3 perovskite, J. Phys. Chem. Lett. 6 (2015) 1729–1735.

[41] J.-W. Lee, S.-G. Kim, J.-M. Yang, Y. Yang, N.-G. Park, Verification and mitigation of ion migration in perovskite solar cells, Apl. Mater. 7 (2019), 041111.

[42] Z. Li, C. Xiao, Y. Yang, S.P. Harvey, D.H. Kim, J.A. Christians, M. Yang, P. Schulz, S.U. Nanayakkara, C.-S. Jiang, J.M. Luther, J.J. Berry, M.C. Beard, M.M. Al-Jassim, K. Zhu, Extrinsic ion migration in perovskite solar cells, Energy Environ. Sci. 10 (2017) 1234–1242.

[43] H.-C. Hsieh, C.-Y. Hsiow, K.-F. Lin, Y.-C. Shih, L. Wang, C. Renaud, T.-P. Nguyen, Analysis of defects and traps in N–I–P layered-structure of perovskite solar cells by charge-based deep level transient spectroscopy (Q-DLTS), J. Phys. Chem. C 122 (2018) 17601–17611.

[44] G. Garcia-Belmonte, J. Bisquert, Distinction between capacitive and noncapacitive hysteretic currents in operation and degradation of perovskite solar cells, ACS Energy Lett. 1 (2016) 683–688.

[45] W. Li, M.U. Rothmann, A. Liu, Z. Wang, Y. Zhang, A.R. Pascoe, J. Lu, L. Jiang, Y. Chen, F. Huang, Y. Peng, Q. Bao, J. Etheridge, U. Bach, Y.-B. Cheng, Phase segregation enhanced ion movement in efficient inorganic CsPbIBr2 solar cells, Adv. Energy Mater. 7 (2017) 1700946.

[46] B. Parida, J. Ryu, S. Yoon, S. Lee, Y. Seo, J.S. Cho, D.-W. Kang, Two-step growth of CsPbI3−xBrx films employing dynamic CsBr treatment: toward all-inorganic perovskite photovoltaics with enhanced stability, J. Mater. Chem. A 7 (2019) 18488–18498.

[47] J. You, Z. Hong, Y. Yang, Q. Chen, M. Cai, T.-B. Song, C.-C. Chen, S. Lu, Y. Liu, H. Zhou, Y. Yang, Low-temperature solution-processed perovskite solar cells with high efficiency and flexibility, ACS Nano 8 (2014) 1674–1680.

[48] S.A. Kulkarni, T. Baikie, P.P. Boix, N. Yantara, N. Mathews, S. Mhaisalkar, Band-gap tuning of lead halide perovskites using a sequential deposition process, J. Mater. Chem. A 2 (2014) 9221–9225.

[49] W. Travis, E.N.K. Glover, H. Bronstein, D.O. Scanlon, R.G. Palgrave, On the application of the tolerance factor to inorganic and hybrid halide perovskites: a revised system, Chem. Sci. 7 (2016) 4548–4556.

[50] Z. Li, M. Yang, J.-S. Park, S.-H. Wei, J.J. Berry, K. Zhu, Stabilizing perovskite structures by tuning tolerance factor: formation of formamidinium and cesium lead iodide solid-state alloys, Chem. Mater. 28 (2016) 284–292.

[51] M. Kulbak, S. Gupta, N. Kedem, I. Levine, T. Bendikov, G. Hodes, D. Cahen, Cesium enhances long-term stability of lead bromide perovskite-based solar cells, J. Phys. Chem. Lett. 7 (2016) 167–172.

[52] J. Liang, C. Wang, Y. Wang, Z. Xu, Z. Lu, Y. Ma, H. Zhu, Y. Hu, C. Xiao, X. Yi, G. Zhu, H. Lv, L. Ma, T. Chen, Z. Tie, Z. Jin, J. Liu, All-inorganic perovskite solar cells, J. Am. Chem. Soc. 138 (2016) 15829–15832.

[53] X. Chang, W. Li, L. Zhu, H. Liu, H. Geng, S. Xiang, J. Liu, H. Chen, Carbon-based CsPbBr3 perovskite solar cells: all-ambient processes and high thermal stability, ACS Appl. Mater. Interfaces 8 (2016) 33649–33655.

[54] Q.A. Akkerman, M. Gandini, F. Di Stasio, P. Rastogi, F. Palazon, G. Bertoni, J. M. Ball, M. Prato, A. Petrozza, L. Manna, Strongly emissive perovskite nanocrystal inks for high-voltage solar cells, Nat. Energy 2 (2016) 16194.

[55] A. Zohar, M. Kulbak, I. Levine, G. Hodes, A. Kahn, D. Cahen, What limits the open-circuit voltage of bromide perovskite-based solar cells? ACS Energy Lett. 4 (2019) 1–7.

[56] A. Ho-Baillie, M. Zhang, C.F.J. Lau, F.-J. Ma, S. Huang, Untapped potentials of inorganic metal halide perovskite solar cells, Joule 3 (2019) 938–955.

[57] S. Colella, E. Mosconi, P. Fedeli, A. Listorti, F. Gazza, F. Orlandi, P. Ferro, T. Besagni, A. Rizzo, G. Calestani, G. Gigli, F. De Angelis, R. Mosca, MAPbI3-xClx mixed halide perovskite for hybrid solar cells: the role of chloride as dopant on the transport and structural properties, Chem. Mater. 25 (2013) 4613–4618.

[58] B. Li, Y. Zhang, L. Zhang, L. Yin, PbCl2-tuned inorganic cubic CsPbBr3(Cl) perovskite solar cells with enhanced electron lifetime, diffusion length and photovoltaic performance, J. Power Sources 360 (2017) 11–20.

[59] J. Duan, T. Hu, Y. Zhao, B. He, Q. Tang, Carbon-electrode-tailored all-inorganic perovskite solar cells to harvest solar and water-vapor energy, Angew. Chem. Int. Ed. 57 (2018) 5746–5749.

[60] H. Yuan, Y. Zhao, J. Duan, B. He, Z. Jiao, Q. Tang, Enhanced charge extraction by setting intermediate energy levels in all-inorganic CsPbBr3 perovskite solar cells, Electrochim. Acta 279 (2018) 84–90.

[61] J. Duan, Y. Zhao, B. He, Q. Tang, Simplified perovskite solar cell with 4.1% efficiency employing inorganic CsPbBr3 as light absorber, Small 14 (2018) 1704443.

[62] J. Duan, Y. Zhao, X. Yang, Y. Wang, B. He, Q. Tang, Lanthanide ions doped CsPbBr3 halides for HTM-free 10.14%-efficiency inorganic perovskite solar cell with an ultrahigh open-circuit voltage of 1.594 V, Adv. Energy Mater. 8 (2018) 1802346.

[63] A. Swarnkar, A.R. Marshall, E.M. Sanehira, B.D. Chernomordik, D.T. Moore, J. A. Christians, T. Chakrabarti, J.M. Luther, Quantum dot–induced phase stabilization of α-$CsPbI_3$ perovskite for high-efficiency photovoltaics, Science 354 (2016) 92.

[64] E.M. Sanehira, A.R. Marshall, J.A. Christians, S.P. Harvey, P.N. Ciesielski, L. M. Wheeler, P. Schulz, L.Y. Lin, M.C. Beard, J.M. Luther, Enhanced mobility $CsPbI_3$ quantum dot arrays for record-efficiency, high-voltage photovoltaic cells, Sci. Adv. 3 (2017) eaao4204.

[65] Q. Wang, X. Zheng, Y. Deng, J. Zhao, Z. Chen, J. Huang, Stabilizing the α-phase of CsPbI3 perovskite by sulfobetaine zwitterions in one-step spin-coating films, Joule 1 (2017) 371–382.

[66] Y. Fu, M.T. Rea, J. Chen, D.J. Morrow, M.P. Hautzinger, Y. Zhao, D. Pan, L. H. Manger, J.C. Wright, R.H. Goldsmith, S. Jin, Selective stabilization and photophysical properties of metastable perovskite polymorphs of CsPbI3 in thin films, Chem. Mater. 29 (2017) 8385–8394.

[67] T. Zhang, M.I. Dar, G. Li, F. Xu, N. Guo, M. Grätzel, Y. Zhao, Bication lead iodide 2D perovskite component to stabilize inorganic α-$CsPbI_3$ perovskite phase for high-efficiency solar cells, Sci. Adv. 3 (2017), e1700841.

[68] Y. Wang, T. Zhang, M. Kan, Y. Li, T. Wang, Y. Zhao, Efficient α-CsPbI3 photovoltaics with surface terminated organic cations, Joule 2 (2018) 2065–2075.

[69] S. Xiang, Z. Fu, W. Li, Y. Wei, J. Liu, H. Liu, L. Zhu, R. Zhang, H. Chen, Highly air-stable carbon-based α-CsPbI3 perovskite solar cells with a broadened optical spectrum, ACS Energy Lett. 3 (2018) 1824–1831.

[70] Y. Hu, F. Bai, X. Liu, Q. Ji, X. Miao, T. Qiu, S. Zhang, Bismuth incorporation stabilized α-CsPbI3 for fully inorganic perovskite solar cells, ACS Energy Lett. 2 (2017) 2219–2227.

[71] C.F.J. Lau, X. Deng, J. Zheng, J. Kim, Z. Zhang, M. Zhang, J. Bing, B. Wilkinson, L. Hu, R. Patterson, S. Huang, A. Ho-Baillie, Enhanced performance via partial lead replacement with calcium for a CsPbI3 perovskite solar cell exceeding 13% power conversion efficiency, J. Mater. Chem. A 6 (2018) 5580–5586.

[72] S. Xiang, W. Li, Y. Wei, J. Liu, H. Liu, L. Zhu, H. Chen, The synergistic effect of non-stoichiometry and Sb-doping on air-stable α-CsPbI3 for efficient carbon-based perovskite solar cells, Nanoscale 10 (2018) 9996–10004.

[73] B. Zhao, S.-F. Jin, S. Huang, N. Liu, J.-Y. Ma, D.-J. Xue, Q. Han, J. Ding, Q.-Q. Ge, Y. Feng, J.-S. Hu, Thermodynamically stable orthorhombic γ-CsPbI3 thin films for high-performance photovoltaics, J. Am. Chem. Soc. 140 (2018) 11716–11725.

[74] P. Ayyub, V.R. Palkar, S. Chattopadhyay, M. Multani, Effect of crystal size reduction on lattice symmetry and cooperative properties, Phys. Rev. B 51 (1995) 6135–6138.

[75] R.J. Sutton, G.E. Eperon, L. Miranda, E.S. Parrott, B.A. Kamino, J.B. Patel, M. T. Hörantner, M.B. Johnston, A.A. Haghighirad, D.T. Moore, H.J. Snaith, Bandgap-tunable cesium lead halide perovskites with high thermal stability for efficient solar cells, Adv. Energy Mater. 6 (2016) 1502458.

[76] R.E. Beal, D.J. Slotcavage, T. Leijtens, A.R. Bowring, R.A. Belisle, W.H. Nguyen, G.F. Burkhard, E.T. Hoke, M.D. McGehee, Cesium lead halide perovskites with improved stability for tandem solar cells, J. Phys. Chem. Lett. 7 (2016) 746–751.

[77] H. Rao, S. Ye, F. Gu, Z. Zhao, Z. Liu, Z. Bian, C. Huang, Morphology controlling of all-inorganic perovskite at low temperature for efficient rigid and flexible solar cells, Adv. Energy Mater. 8 (2018) 1800758.

[78] C.-Y. Chen, H.-Y. Lin, K.-M. Chiang, W.-L. Tsai, Y.-C. Huang, C.-S. Tsao, H.-W. Lin, All-vacuum-deposited stoichiometrically balanced inorganic cesium lead halide perovskite solar cells with stabilized efficiency exceeding 11%, Adv. Mater. 29 (2017) 1605290.

[79] J.K. Nam, M.S. Jung, S.U. Chai, Y.J. Choi, D. Kim, J.H. Park, Unveiling the crystal formation of cesium lead mixed-halide perovskites for efficient and stable solar cells, J. Phys. Chem. Lett. 8 (2017) 2936–2940.

[80] J.K. Nam, S.U. Chai, W. Cha, Y.J. Choi, W. Kim, M.S. Jung, J. Kwon, D. Kim, J. H. Park, Potassium incorporation for enhanced performance and stability of fully inorganic cesium lead halide perovskite solar cells, Nano Lett. 17 (2017) 2028–2033.

[81] C.F.J. Lau, M. Zhang, X. Deng, J. Zheng, J. Bing, Q. Ma, J. Kim, L. Hu, M.A. Green, S. Huang, A. Ho-Baillie, Strontium-doped low-temperature-processed CsPbI2Br perovskite solar cells, ACS Energy Lett. 2 (2017) 2319–2325.

[82] Q. Ma, S. Huang, X. Wen, M.A. Green, A.W.Y. Ho-Baillie, Hole transport layer free inorganic CsPbIBr2 perovskite solar cell by dual source thermal evaporation, Adv. Energy Mater. 6 (2016) 1502202.

[83] C.F.J. Lau, X. Deng, Q. Ma, J. Zheng, J.S. Yun, M.A. Green, S. Huang, A.W.Y. Ho-Baillie, CsPbIBr2 perovskite solar cell by spray-assisted deposition, ACS Energy Lett. 1 (2016) 573–577.

[84] J. Liang, P. Zhao, C. Wang, Y. Wang, Y. Hu, G. Zhu, L. Ma, J. Liu, Z. Jin, CsPb0.9Sn0.1IBr2 based all-inorganic perovskite solar cells with exceptional efficiency and stability, J. Am. Chem. Soc. 139 (2017) 14009–14012.

[85] K. Yamada, S. Funabiki, H. Horimoto, T. Matsui, T. Okuda, S. Ichiba, Structural phase transitions of the polymorphs of CsSnI3 by means of rietveld analysis of the X-ray diffraction, Chem. Lett. 20 (1991) 801–804.

[86] C. Yu, Y. Ren, Z. Chen, K. Shum, First-principles study of structural phase transitions in CsSnI3, J. Appl. Phys. 114 (2013) 163505.

[87] K. Shum, Z. Chen, J. Qureshi, C. Yu, J.J. Wang, W. Pfenninger, N. Vockic, J. Midgley, J.T. Kenney, Synthesis and characterization of CsSnI3 thin films, Appl. Phys. Lett. 96 (2010) 221903.

[88] G. Xing, M.H. Kumar, W.K. Chong, X. Liu, Y. Cai, H. Ding, M. Asta, M. Grätzel, S. Mhaisalkar, N. Mathews, T.C. Sum, Solution-processed tin-based perovskite for near-infrared lasing, Adv. Mater. 28 (2016) 8191–8196.

[89] I. Chung, J.-H. Song, J. Im, J. Androulakis, C.D. Malliakas, H. Li, A.J. Freeman, J. T. Kenney, M.G. Kanatzidis, CsSnI3: semiconductor or metal? High electrical conductivity and strong near-infrared photoluminescence from a single material. High hole mobility and phase-transitions, J. Am. Chem. Soc. 134 (2012) 8579–8587.

[90] I. Chung, B. Lee, J. He, R.P.H. Chang, M.G. Kanatzidis, All-solid-state dye-sensitized solar cells with high efficiency, Nature 485 (2012) 486.

[91] Z. Chen, J.J. Wang, Y. Ren, C. Yu, K. Shum, Schottky solar cells based on CsSnI3 thin-films, Appl. Phys. Lett. 101 (2012), 093901.

[92] M.H. Kumar, S. Dharani, W.L. Leong, P.P. Boix, R.R. Prabhakar, T. Baikie, C. Shi, H. Ding, R. Ramesh, M. Asta, M. Graetzel, S.G. Mhaisalkar, N. Mathews, Lead-free halide perovskite solar cells with high photocurrents realized through vacancy modulation, Adv. Mater. 26 (2014) 7122–7127.

[93] P. Xu, S. Chen, H.-J. Xiang, X.-G. Gong, S.-H. Wei, Influence of defects and synthesis conditions on the photovoltaic performance of perovskite semiconductor CsSnI3, Chem. Mater. 26 (2014) 6068–6072.

[94] N. Wang, Y. Zhou, M.-G. Ju, H.F. Garces, T. Ding, S. Pang, X.C. Zeng, N. P. Padture, X.W. Sun, Heterojunction-depleted lead-free perovskite solar cells with coarse-grained B-γ-CsSnI3 thin films, Adv. Energy Mater. 6 (2016) 1601130.

[95] K.P. Marshall, M. Walker, R.I. Walton, R.A. Hatton, Enhanced stability and efficiency in hole-transport-layer-free CsSnI3 perovskite photovoltaics, Nat. Energy 1 (2016) 16178.

[96] S. Gupta, T. Bendikov, G. Hodes, D. Cahen, CsSnBr3, A lead-free halide perovskite for long-term solar cell application: insights on SnF2 addition, ACS Energy Lett. 1 (2016) 1028–1033.

[97] T.-B. Song, T. Yokoyama, C.C. Stoumpos, J. Logsdon, D.H. Cao, M.R. Wasielewski, S. Aramaki, M.G. Kanatzidis, Importance of reducing vapor atmosphere in the fabrication of tin-based perovskite solar cells, J. Am. Chem. Soc. 139 (2017) 836–842.

[98] T.-B. Song, T. Yokoyama, S. Aramaki, M.G. Kanatzidis, Performance enhancement of lead-free tin-based perovskite solar cells with reducing atmosphere-assisted dispersible additive, ACS Energy Lett. 2 (2017) 897–903.

[99] D. Sabba, H.K. Mulmudi, R.R. Prabhakar, T. Krishnamoorthy, T. Baikie, P.P. Boix, S. Mhaisalkar, N. Mathews, Impact of anionic Br– substitution on open circuit voltage in lead free perovskite (CsSnI3-xBrx) solar cells, J. Phys. Chem. C 119 (2015) 1763–1767.

[100] W. Li, J. Li, J. Li, J. Fan, Y. Mai, L. Wang, Addictive-assisted construction of all-inorganic CsSnIBr2 mesoscopic perovskite solar cells with superior thermal stability up to 473 K, J. Mater. Chem. A 4 (2016) 17104–17110.

[101] J. Duan, Y. Zhao, B. He, Q. Tang, High-purity inorganic perovskite films for solar cells with 9.72 % efficiency, Angew. Chem. Int. Ed. 57 (2018) 3787–3791.

[102] P. Luo, Y. Zhou, S. Zhou, Y. Lu, C. Xu, W. Xia, L. Sun, Fast anion-exchange from CsPbI3 to CsPbBr3 via Br2-vapor-assisted deposition for air-stable all-inorganic perovskite solar cells, Chem. Eng. J. 343 (2018) 146–154.

[103] K.C. Tang, P. You, F. Yan, Highly stable All-inorganic perovskite solar cells processed at low temperature, Solar RRL 2 (2018) 1800075.

[104] A.J. Ramadan, L.A. Rochford, S. Fearn, H.J. Snaith, Processing solvent-dependent electronic and structural properties of cesium lead triiodide thin films, J. Phys. Chem. Lett. 8 (2017) 4172–4176.

[105] P. Luo, W. Xia, S. Zhou, L. Sun, J. Cheng, C. Xu, Y. Lu, Solvent engineering for ambient-air-processed, phase-stable CsPbI3 in perovskite solar cells, J. Phys. Chem. Lett. 7 (2016) 3603–3608.

[106] P. Wang, X. Zhang, Y. Zhou, Q. Jiang, Q. Ye, Z. Chu, X. Li, X. Yang, Z. Yin, J. You, Solvent-controlled growth of inorganic perovskite films in dry environment for efficient and stable solar cells, Nat. Commun. 9 (2018) 2225.

[107] G. Yin, H. Zhao, H. Jiang, S. Yuan, T. Niu, K. Zhao, Z. Liu, S. Liu, Precursor engineering for all-inorganic CsPbI2Br perovskite solar cells with 14.78% efficiency, Adv. Funct. Mater. 28 (2018) 1803269.

[108] S. Zhang, S. Wu, W. Chen, H. Zhu, Z. Xiong, Z. Yang, C. Chen, R. Chen, L. Han, W. Chen, Solvent engineering for efficient inverted perovskite solar cells based on inorganic CsPbI2Br light absorber, Mater. Today Energy 8 (2018) 125–133.

[109] L.A. Frolova, D.V. Anokhin, A.A. Piryazev, S.Y. Luchkin, N.N. Dremova, K. J. Stevenson, P.A. Troshin, Highly efficient all-inorganic planar heterojunction perovskite solar cells produced by thermal coevaporation of CsI and PbI2, J. Phys. Chem. Lett. 8 (2017) 67–72.

[110] R. Kottokkaran, H.A. Gaonkar, B. Bagheri, V.L. Dalal, Efficient p-i-n inorganic CsPbI3 perovskite solar cell deposited using layer-by-layer vacuum deposition, J. Vac. Sci. Technol. 36 (2018), 041201.

[111] M.J. Bækbo, O. Hansen, I. Chorkendorff, P.C.K. Vesborg, Deposition of methylammonium iodide via evaporation – combined kinetic and mass spectrometric study, RSC Adv. 8 (2018) 29899–29908.

[112] L. Zhang, B. Li, J. Yuan, M. Wang, T. Shen, F. Huang, W. Wen, G. Cao, J. Tian, High-voltage-efficiency inorganic perovskite solar cells in a wide solution-processing window, J. Phys. Chem. Lett. 9 (2018) 3646–3653.

[113] C. Dong, X. Han, Y. Zhao, J. Li, L. Chang, W. Zhao, A green anti-solvent process for high performance carbon-based CsPbI2Br all-inorganic perovskite solar cell, Solar RRL 2 (2018) 1800139.

[114] W. Zhu, Q. Zhang, D. Chen, Z. Zhang, Z. Lin, J. Chang, J. Zhang, C. Zhang, Y. Hao, Intermolecular exchange boosts efficiency of air-stable, carbon-based all-

inorganic planar CsPbIBr2 perovskite solar cells to over 9%, Adv. Energy Mater. 8 (2018) 1802080.
[115] D. Moghe, L. Wang, C.J. Traverse, A. Redoute, M. Sponseller, P.R. Brown, V. Bulović, R.R. Lunt, All vapor-deposited lead-free doped CsSnBr3 planar solar cells, Nano Energy 28 (2016) 469–474.
[116] P. Zhu, C. Chen, S. Gu, R. Lin, J. Zhu, CsSnI3 solar cells via an evaporation-assisted solution method, Solar RRL 2 (2018) 1700224.
[117] P. Zhao, B.J. Kim, H.S. Jung, Passivation in perovskite solar cells: a review, Mater. Today Energy 7 (2018) 267–286.
[118] B. Li, Y. Zhang, L. Fu, T. Yu, S. Zhou, L. Zhang, L. Yin, Surface passivation engineering strategy to fully-inorganic cubic CsPbI3 perovskites for high-performance solar cells, Nat. Commun. 9 (2018) 1076.
[119] Q. Zeng, X. Zhang, X. Feng, S. Lu, Z. Chen, X. Yong, S.A.T. Redfern, H. Wei, H. Wang, H. Shen, W. Zhang, W. Zheng, H. Zhang, J.S. Tse, B. Yang, Polymer-passivated inorganic cesium lead mixed-halide perovskites for stable and efficient solar cells with high open-circuit voltage over 1.3 V, Adv. Mater. 30 (2018) 1705393.
[120] J. Yuan, L. Zhang, C. Bi, M. Wang, J. Tian, Surface trap states passivation for high-performance inorganic perovskite solar cells, Solar RRL 2 (2018) 1800188.
[121] Y. Zhao, T. Liu, F. Ren, J. Duan, Y. Wang, X. Yang, Q. Li, Q. Tang, Organic hole-transporting materials for 9.32%-efficiency and stable CsPbBr3 perovskite solar cells, Mater. Chem. Front. 2 (2018) 2239–2244.
[122] H. Uratani, K. Yamashita, Charge carrier trapping at surface defects of perovskite solar cell absorbers: a first-principles study, J. Phys. Chem. Lett. 8 (2017) 742–746.
[123] D. Meggiolaro, S.G. Motti, E. Mosconi, A.J. Barker, J. Ball, C. Andrea Riccardo Perini, F. Deschler, A. Petrozza, F. De Angelis, Iodine chemistry determines the defect tolerance of lead-halide perovskites, Energy Environ. Sci. 11 (2018) 702–713.
[124] J. Ding, J. Duan, C. Guo, Q. Tang, Toward charge extraction in all-inorganic perovskite solar cells by interfacial engineering, J. Mater. Chem. A 6 (2018) 21999–22004.
[125] C. Liu, W. Li, J. Chen, J. Fan, Y. Mai, R.E.I. Schropp, Ultra-thin MoOx as cathode buffer layer for the improvement of all-inorganic CsPbIBr2 perovskite solar cells, Nano Energy 41 (2017) 75–83.
[126] C. Liu, W. Li, C. Zhang, Y. Ma, J. Fan, Y. Mai, All-inorganic CsPbI2Br perovskite solar cells with high efficiency exceeding 13%, J. Am. Chem. Soc. 140 (2018) 3825–3828.
[127] W. Zhu, Z. Zhang, W. Chai, D. Chen, H. Xi, J. Chang, J. Zhang, C. Zhang, Y. Hao, Benign pinholes in CsPbIBr2 absorber film enable efficient carbon-based, all-inorganic perovskite solar cells, ACS Appl. Energy Mater. 2 (2019) 5254–5262.
[128] W.S. Subhani, K. Wang, M. Du, X. Wang, S. Liu, Interface-modification-induced gradient energy band for highly efficient CsPbIBr2 perovskite solar cells, Adv. Energy Mater. 9 (2019) 1803785.
[129] J. Lu, S.-C. Chen, Q. Zheng, Defect passivation of CsPbIBr2 perovskites for high-performance solar cells with large open-circuit voltage of 1.28 V, ACS Appl. Energy Mater. 1 (2018) 5872–5878.
[130] X. Wen, W. Chen, J. Yang, Q. Ou, T. Yang, C. Zhou, H. Lin, Z. Wang, Y. Zhang, G. Conibeer, Q. Bao, B. Jia, D.J. Moss, Role of surface recombination in halide perovskite nanoplatelets, ACS Appl. Mater. Interfaces 10 (2018) 31586–31593.
[131] T. Leijtens, I.K. Ding, T. Giovenzana, J.T. Bloking, M.D. McGehee, A. Sellinger, Hole transport materials with low glass transition temperatures and high solubility for application in solid-state dye-sensitized solar cells, ACS Nano 6 (2012) 1455–1462.
[132] Z. Liu, A. Zhu, F. Cai, L. Tao, Y. Zhou, Z. Zhao, Q. Chen, Y.-B. Cheng, H. Zhou, Nickel oxide nanoparticles for efficient hole transport in p-i-n and n-i-p perovskite solar cells, J. Mater. Chem. A 5 (2017) 6597–6605.
[133] W. Chen, Y. Wu, Y. Yue, J. Liu, W. Zhang, X. Yang, H. Chen, E. Bi, I. Ashraful, M. Grätzel, L. Han, Efficient and stable large-area perovskite solar cells with inorganic charge extraction layers, Science 350 (2015) 944.
[134] Q. He, K. Yao, X. Wang, X. Xia, S. Leng, F. Li, Room-temperature and solution-processable Cu-doped nickel oxide nanoparticles for efficient hole-transport layers of flexible large-area perovskite solar cells, ACS Appl. Mater. Interfaces 9 (2017) 41887–41897.
[135] N. Arora, M.I. Dar, A. Hinderhofer, N. Pellet, F. Schreiber, S.M. Zakeeruddin, M. Grätzel, Perovskite solar cells with CuSCN hole extraction layers yield stabilized efficiencies greater than 20%, Science 358 (2017) 768.
[136] Z. Zhu, Y. Bai, X. Liu, C.-C. Chueh, S. Yang, A.K.Y. Jen, Enhanced efficiency and stability of inverted perovskite solar cells using highly crystalline SnO2 nanocrystals as the robust electron-transporting layer, Adv. Mater. 28 (2016) 6478–6484.
[137] M.B. Islam, M. Yanagida, Y. Shirai, Y. Nabetani, K. Miyano, NiOx hole transport layer for perovskite solar cells with improved stability and reproducibility, ACS Omega 2 (2017) 2291–2299.
[138] B. Yang, M. Wang, X. Hu, T. Zhou, Z. Zang, Highly efficient semitransparent $CsPbIBr_2$ perovskite solar cells via low-temperature processed In2S3 as electron-transport-layer, Nano Energy 57 (2019) 718–727.
[139] I. Poli, U. Hintermair, M. Regue, S. Kumar, E.V. Sackville, J. Baker, T.M. Watson, S. Eslava, P.J. Cameron, Graphite-protected CsPbBr3 perovskite photoanodes functionalised with water oxidation catalyst for oxygen evolution in water, Nat. Commun. 10 (2019) 2097.
[140] L. Ma, W. Zhang, P. Zhao, J. Liang, Y. Hu, G. Zhu, R. Chen, Z. Tie, J. Liu, Z. Jin, Highly efficient overall water splitting driven by all-inorganic perovskite solar cells and promoted by bifunctional bimetallic phosphide nanowire arrays, J. Mater. Chem. A 6 (2018) 20076–20082.
[141] J. Xu, Y. Chen, L. Dai, Efficiently photo-charging lithium-ion battery by perovskite solar cell, Nat. Commun. 6 (2015) 8103.
[142] S. Hu, C. Xiang, S. Haussener, A.D. Berger, N.S. Lewis, An analysis of the optimal band gaps of light absorbers in integrated tandem photoelectrochemical water-splitting systems, Energy Environ. Sci. 6 (2013) 2984–2993.
[143] D. Bae, G.M. Faasse, G. Kanellos, W.A. Smith, Unravelling the practical solar charging performance limits of redox flow batteries based on a single photon device system, Sustain. Energy Fuels 3 (2019) 2399–2408.